

Incremental Nonlinear Dynamic Inversion and Multihole Pressure Probes for Disturbance Rejection Control of Fixed-Wing Micro Air Vehicles

Elisabeth Sophia van der Sman

Technische Universiteit Delft

INCREMENTAL NONLINEAR DYNAMIC INVERSION AND MULTIHOLE PRESSURE PROBES FOR DISTURBANCE REJECTION CONTROL OF FIXED-WING MICRO AIR VEHICLES

by

Elisabeth Sophia van der Sman

in partial fulfillment of the requirements for the degree of

Master of Science
in Aerospace Engineering

at the Delft University of Technology,
to be defended publicly on Thursday 22nd of December, 2016 at 10:00 AM.

Supervisors:	Dr. ir. Q. P. Chu,	
	Ir. B. Remes,	
	Ir. E. J. J. Smeur	
Thesis committee:	Dr. ir. Q. P. Chu,	TU Delft
	Dr. ir. G. C. H. E. de Croon,	TU Delft
	Ir. B. Remes,	TU Delft
	Ir. C. de Wagter,	TU Delft
	Ir. E. J. J. Smeur,	TU Delft
	Prof. dr. ir. S. Watkins	RMIT

This thesis is confidential and cannot be made public until December 22, 2018.

An electronic version of this thesis is available at <http://repository.tudelft.nl/>.

PREFACE

Micro Air Vehicles (MAVs) are becoming an integral part of our society. Due to the development of cheap electronic components, MAVs can be bought in shops around the entire world. The small size and the low weight make them ideal for new applications such as search and rescue missions, mapping the environment, photography and filming. In densely populated areas the safety and the reliability of MAVs have to be guaranteed in order to benefit from the services they provide. One of the main challenges when flying in urban environments is the high levels of turbulence intensity experienced by the MAV. The aim of this thesis is to improve the stability of MAVs flying through turbulence by using state-of-the-art control techniques and sensors inspired by the flight of birds. This thesis combines my interest for aviation and robotics. It explores the behavior of fixed-wing MAVs during flight allowing me to relate the work to my own passion for flying gliders. On the other hand it deals with a multidisciplinary challenge of combining electrical components, software and mechanical designs.

This thesis marks the end of my studies at the Faculty of Aerospace Engineering at Delft University of Technology. This achievement would not have been possible without the support of my supervisors, colleagues, friends and family.

I would like to thank my supervisor Bart Remes for his extensive support from the moment I joined the MAVLab team. He gave me the opportunity to travel to Australia for my internship at RMIT, which turned out to be a very enriching experience. As the team manager, Bart inspired me to look beyond the engineering perspective and to consider how technology can change the world we live in.

I would like to thank my daily supervisor Ewoud Smeur for teaching me how to critically review my work and for helping me deal with drawbacks and unexpected technical difficulties throughout the project.

I am equally grateful to Christophe de Wagter for his commitment to my project. I much benefited from his excellent piloting skills and the stimulating discussions on my research project.

I am particularly thankful to my supervisor, and chairman of the committee, Dr. Chu for his excellent feedback on my research questions, for his enthusiasm, and for inspiring me to believe in the importance of my work.

I also owe much gratitude to Prof. Watkins for sharing his insights and expertise regarding turbulence and phase-advanced sensors, and for the warm welcome and incredible hospitality I received at RMIT during my internship.

At Delft University of Technology, working at MAVLab has been most inspiring. The MAVLab team represents an extremely passionate group of researchers who love their work and have made my studies a delightful and memorable experience.

I finally owe special gratitude to my dearest Freek, my beloved sister Lydia and my dear parents for their constant and unconditional support. With their love and kindness they guided me through stressful moments keeping me focused on achieving my goals.

*Elisabeth Sophia van der Sman
Delft, 11 December 2016*

NOMENCLATURE

α	Angle of attack, rad
β	Side slip angle, rad
χ	Course angle, rad
δ_a	Aileron deflection, rad/s
δ_e	Elevator deflection, rad/s
δ_r	Rudder deflection, rad/s
δ_t	Throttle input
Ω	Angular rates matrix, rad/s
\mathbf{I}	Moment of inertia matrix, Nm ²
\mathbf{M}	Sum of moments around the body axes matrix, Nm
D	Derivative gain
I	Integral gain
P	Proportional gain
ϕ	Roll angle, rad
ψ	Yaw angle, rad
θ	Pitch angle, rad
ζ	Damping term of second order filter
A	Actuator Dynamics
f	Sensitivity factor
G	Control effectiveness, rad/(s ² rad)
H	Filter
M_x	Moment around the X_B -axis, Nm
M_y	Moment around the Y_B -axis, Nm
M_z	Moment around the Z_B -axis, Nm
p	Roll rate, rad/s
P_α	Probe pressure differential between top and bottom hole, Pa
P_β	Probe pressure differential between right and left hole, Pa
P_R	Probe pressure differential between center and top hole, Pa
P_∞	Free stream pressure, Pa
q	Dynamic pressure, Pa

q	Pitch rate, rad/s
r	Yaw rate, rad/s
u	Component of V along the X_B -axis, m/s
V	Airspeed vector, m/s
v	Component of V along the Y_B -axis, m/s
w	Component of V along the Z_B -axis, m/s
w_n	Natural frequency of second order filter, rad/s
x	position of MAV, x-coordinate, m
y	position of MAV, y-coordinate, m
z	position of MAV, z-coordinate, m

CONTENTS

I	Research Paper	1
II	Thesis	20
1	Introduction	21
2	Literature Study	22
2.1	Control techniques	22
2.1.1	PID.	22
2.1.2	NDI	23
2.1.3	INDI	24
2.1.4	AINDI	26
2.2	Turbulence	27
2.2.1	Wind tunnel turbulence	28
2.2.2	Measurement systems	29
2.3	Phase-advanced sensors	30
2.3.1	5 hole pressure probe	33
2.4	Discussion and Conclusion	34
2.5	Research question, aims and objectives	35
3	MAV Model	37
3.1	Roll axis	38
3.1.1	Roll Rig.	39
3.1.2	Wind tunnel flight	41
3.1.3	Outdoor flight	42
3.1.4	Conclusion and Recommendations	43
3.2	Pitch axis	44
3.2.1	Pitch Rig	44
3.2.2	Wind tunnel flight	47
3.2.3	Outdoor flight	48
3.2.4	Conclusion and Recommendations	48
3.3	Yaw axis coupling	49
3.4	Actuators	49
3.5	Phase-Advanced Sensors	50
4	Controller Design	58
4.1	Inner loop control.	58
4.1.1	INDI	58
4.1.2	PID.	60
4.1.3	Phase-advanced sensors	62
4.2	Outer loop control	64
4.2.1	Throttle control	64
4.2.2	Vertical pitch control.	65
4.2.3	Lateral control	65
4.2.4	Outdoor airspeed control	66

5	Experimental Set-Up	67
5.1	Slick 360 Micro	67
5.2	OJF	68
5.2.1	OptiTrack system	68
5.2.2	Pitch and roll rig set-up	69
5.2.3	Free flight set-up	70
5.2.4	Turbulence grids set-up	70
5.3	Sensor calibration	71
6	Results	72
6.1	Preliminary outdoor flights	72
6.1.1	Roll axis	72
6.1.2	Pitch axis.	74
6.2	Autonomous wind tunnel flights	75
6.3	Outdoor test flights	84
7	Conclusion	88
	Bibliography	91

I

RESEARCH PAPER

Incremental Nonlinear Dynamic Inversion and Multihole Pressure Probes for Disturbance Rejection Control of Fixed-wing Micro Air Vehicles

Elisabeth S. van der Sman,^{*} Ewoud J. J. Smeur,[†] Bart Remes,[‡] and Qiping Chu[§]

Delft University of Technology, 2629 HS Delft, The Netherlands

Maintaining stable flight during high turbulence intensities is challenging for fixed-wing micro air vehicles. Two methods have been identified to improve the disturbance rejection performance of the MAV: incremental nonlinear dynamic inversion and phase-advanced pitch probes. Incremental nonlinear dynamic inversion uses the angular acceleration measurements to counteract disturbances. Multihole pressure probes measure the incoming flow angle and velocity ahead of the wing in order to react to gusts before an inertial response has occurred. The performance of incremental nonlinear dynamic inversion is compared to a traditional proportional integral derivative controller with and without the multihole pressure probes. The attitude controllers are tested by performing autonomous wind tunnel flights and stability augmented outdoor flights. This paper shows that nonlinear dynamic inversion improves the disturbance rejection performance of fixed-wing MAVs compared to traditional proportional integral derivative controllers.

Nomenclature

α	Angle of attack, rad
δ_a	Aileron deflection, rad/s
δ_e	Elevator deflection, rad/s
δ_r	Rudder deflection, rad/s
δ_t	Throttle input
Ω	Angular rates matrix, rad/s
\mathbf{I}	Moment of inertia matrix, Nm ²
\mathbf{M}	Sum of moments around the body axes matrix, Nm
ϕ	Roll angle, rad
ψ	Yaw angle, rad
σ	Standard deviation
θ	Pitch angle, rad
f	Frequency, Hz
G	Control effectiveness, rad/(s ² rad)
L_x	Turbulence length scale in longitudinal direction, m
M_x	Moment around the X_B -axis, Nm
M_y	Moment around the Y_B -axis, Nm
M_z	Moment around the Z_B -axis, Nm
p	Roll rate, rad/s
q	Pitch rate, rad/s
r	Yaw rate, rad/s
u	Component of V along the X_B -axis, m/s

^{*}Msc. Student, Control and Simulation Department, Faculty of Aerospace Engineering

[†]Ph.D. Candidate, Control and Simulation Department, Faculty of Aerospace Engineering

[‡]Researcher at MAVLAB, Control and Simulation Department, Faculty of Aerospace Engineering

[§]Associate Professor, Control and Simulation Department, Faculty of Aerospace Engineering. Member AIAA.

V	Airspeed vector, m/s
v	Component of V along the Y_B -axis, m/s
w	Component of V along the Z_B -axis, m/s

I. Introduction

THE number of Micro Air Vehicles (MAVs) flying in urban areas is increasing due to the low cost, the low weight, the availability of ready-to-use platforms and the variety of applications. Fixed-wing MAVs are ideal for tasks which require a long range and endurance such as mapping the environment, surveillance, photography and delivering goods. These tasks may require the MAV to fly between buildings and obstacles which generate high energy turbulence.¹ The turbulence intensity profile increases as the MAV flies closer to the ground reaching levels up to 50%.² The perceived turbulence level depends on the MAV flight speed. The lower the flight speed the higher the turbulence intensity, indicating that hover is the most critical condition for MAVs.³ Fixed-wing MAVs are particularly susceptible to wind gusts due to the large wing area which is subject to uneven lift distributions causing unpredictable roll and pitch inputs.³ High levels of turbulence intensity provide a serious threat to the stability of the MAV. The safety and reliability of MAVs becomes increasingly important when operating close to densely populated areas. Mohamed et al. identified two main approaches to counteract turbulence: reactive and phase-advanced.² This paper focuses on developing a reactive nonlinear controller in combination with phase-advanced sensors to increase the stability of fixed-wing MAVs flying through turbulence.

Reactive techniques use sensors to measure the inertial response to disturbances. The angular acceleration is the first to occur. It leads to changes in the angular rate which in turn causes errors in the attitude angles. Controllers that use Inertial Measurement Units (IMUs) to control the MAV attitude are reactive techniques. The most common controller is Proportional Integral Derivative (PID). It is an error based linear controller. When applied to fixed-wing MAVs the error is calculated based on the attitude angles and rates. The main advantage of this technique is that no knowledge of the MAV model is required. The main disadvantage is the linear property of PID controllers. Fixed-wing aircraft are nonlinear systems which require a different set of gains for each linearization point in the flight envelope. Gusts cause large variations in airspeed and attitude angles leading to nonlinear behavior. To maintain an optimal performance gain scheduling is often used over a range of linearization points.⁴ The complexity of gain scheduling leads to the analysis of nonlinear control techniques to improve the performance of fixed-wing MAVs in turbulence. Nonlinear Dynamic Inversion (NDI) is a model based nonlinear controller which calculates the control inputs based on changes in the model states. A uniform performance over the flight envelope is guaranteed if the aerodynamic model is accurately known.⁵ The major disadvantage of NDI is that unstable situations or loss of control can occur in case of model mismatch.⁶ Determining an accurate aerodynamic model of the MAV is very expensive and time consuming. NDI has been applied to the Lockheed Marting X-35^{7,8} and to the NASA X-36 tailless aircraft.⁹ The MAV used in this research has a very low development cost and is therefore not suited for the NDI control strategy. Research has been performed to make this control technique less dependent on the model leading to the development of Incremental Nonlinear Dynamic Inversion (INDI)^{10,11}.⁶ INDI is a sensor-based nonlinear controller which uses the angular acceleration error to determine the control input.¹² This controller is much more robust compared to NDI. When applied to MAVs the angular acceleration is determined by differentiating the angular rate provided by the gyroscopes. To decrease the noise level, filtering of the gyroscopes is required introducing a delay in the signal. Smeur et al.¹² found that the same filter should be used on the actuators to provide time synchronization with the measured acceleration. This method analytically proves that the disturbance rejection performance of the INDI controller depends on the actuator dynamics, the filter and the sampling time.¹² This control technique was tested by Smeur et al.¹² on quadcopters. The reaction time became 5 times faster compared to a Proportional Integral Derivative (PID) controller when subject to the same disturbance. Considering the time scale of turbulence, the angular acceleration measurement occurs before the change in attitude angle or angular rate giving the system a time advantage compared to PID controllers. Another advantage of INDI is the low development cost. The only model parameters required by the INDI attitude controller are the actuator dynamics and the control effectiveness.¹² INDI has been implemented on fixed-wing MAVs for the first time by Vlaar.¹³ Test flights performed by Vlaar show that this technique can be used on fixed-wing MAVs. This paper will give a detailed analysis of the reference tracking and the disturbance rejection performance of INDI applied to fixed-wing MAVs.

Phase-advanced sensors are used to measure turbulence before an inertial response has occurred. The first phenomenon to occur is the change in flow pitch angle and velocity ahead of the wing. These variations cause an uneven lift distribution over the wings leading to structural stresses which can be measured by strain sensors.¹⁴ Mohamed et al.² developed a pitch probe sensor inspired by the leading edge feathers of birds. This sensor measures the variations in the angle of attack and speed of the incoming flow. By measuring the incoming gust ahead of the wing a time advantage is created. The gust is related to the pressure distribution over the wing which in turn causes an angular acceleration measurement. The sensor was therefore placed at the point of highest correlation between the surface pressure variation and the measured angular acceleration.¹⁴ The gust measurement is used as a feed-forward component to each aileron separately to locally counteract the gust on each wing.² This sensor enhances the PID controller performance by decreasing the range of the roll and pitch angle displacements and thereby creating a higher probability density function.² These tests were performed in wind tunnels and outdoors. The wind tunnel flights were performed by inserting static turbulence generating grids at the inlet of the test section. The distance from the grids in the direction of the flow determines the turbulence intensity level experienced by the MAV.¹⁵ The main difference with the turbulence experienced outdoors is the length scale, during wind tunnel flights the length scale is in the order of 1 meter compared to 15 meters for outdoor flights.²

The aim of this paper is to investigate the disturbance rejection performance of INDI applied to fixed-wing MAVs in high turbulence intensities and to compare the performance of the proposed system with a traditional PID controller. It is furthermore interesting to evaluate the performance of INDI compared to an enhanced PID controller which uses pitch probe sensors as a feed-forward component. Finally research is performed on the incorporation of the pitch probe sensors in the INDI control structure. All systems are implemented on the Slick 360 Micro fixed-wing MAV with the Open-Source Paparazzi Autopilot system. The disturbance rejection performance is tested in the same turbulence intensity conditions which are typical for urban environments. Two different test set-ups are presented: autonomous wind tunnel tests and outdoor flights.

The structure of this paper is the following: Section II describes the MAV model, Section III is dedicated to the design of the INDI and PID controllers and Section IV describes the pitch probe sensors. Section V presents the experimental set-up. The results are presented in Section VI.

II. MAV Model

The sum of moments experienced during flight by the Slick 360 Micro fixed-wing MAV expressed in the body frame are described by Eq. (1)^{6,16}.

$$\mathbf{M} = \mathbf{I}\dot{\boldsymbol{\Omega}} + \boldsymbol{\Omega} \times \mathbf{I}\boldsymbol{\Omega} \quad (1)$$

In terms of the angular accelerations Eq. (1) is given by Eq. (2).

$$\dot{\boldsymbol{\Omega}} = \mathbf{I}^{-1}(\mathbf{M} - \boldsymbol{\Omega} \times \mathbf{I}\boldsymbol{\Omega}) \quad (2)$$

The sum of moments around the body axes $\{X_B, Y_B, Z_B\}$ is given by $\mathbf{M}^T = [M_x \ M_y \ M_z]$. The angular rates are denoted by $\boldsymbol{\Omega}^T = [p \ q \ r]$. The moment of inertia matrix is defined by Eq. (3) assuming a plane of symmetry around the longitudinal and vertical axis ($X_B Z_B - plane$).

$$\mathbf{I} = \begin{bmatrix} I_{xx} & 0 & -I_{xz} \\ 0 & I_{yy} & 0 \\ -I_{xz} & 0 & I_{zz} \end{bmatrix} \quad (3)$$

The resulting system of equations is given by Eq. (4)^{16,17}

$$\begin{aligned} M_x &= I_{xx}\dot{p} + (I_{zz} - I_{yy})qr - I_{xz}(\dot{r} + pq) \\ M_y &= I_{yy}\dot{q} + (I_{xx} - I_{zz})rp + I_{xz}(p^2 - r^2) \\ M_z &= I_{zz}\dot{r} + (I_{yy} - I_{xx})pq - I_{xz}(\dot{p} + rq) \end{aligned} \quad (4)$$

Expressed in terms of the angular accelerations Eq. (4) becomes Eq. (5).¹⁷

$$\begin{aligned}\dot{p} &= (c_1 r + c_2 p)q + c_3 M_x + c_4 M_z \\ \dot{q} &= c_5 p r - c_6 (p^2 - r^2) + c_7 M_y \\ \dot{r} &= (c_8 p - c_2 r)q + c_4 M_x + c_9 M_z\end{aligned}\quad (5)$$

The definitions of the multiplication parameters c_1 up to c_9 with $\Gamma = I_{xx}I_{zz} - I_{xz}^2$:¹⁷

$$\begin{aligned}\Gamma c_1 &= (I_{yy} - I_{zz})I_{zz} - I_{xz}^2 & \Gamma c_2 &= (I_{xx} - I_{yy} + I_{zz})I_{xz} & \Gamma c_3 &= I_{zz} \\ \Gamma c_4 &= I_{xz} & c_5 &= (I_{zz} - I_{xx})I_{yy}^{-1} & c_6 &= I_{xz}I_{yy}^{-1} \\ c_7 &= I_{yy}^{-1} & c_8 &= (I_{xx} - I_{yy})I_{xx} - I_{xz}^2 & \Gamma c_9 &= I_{xx}\end{aligned}$$

The moments can be split into two components Eq. (6): a part depending on the aerodynamic state variables and a part influenced by the control surfaces of the vehicle.

$$\mathbf{M} = \mathbf{M}_a + \mathbf{M}_c \quad (6)$$

Substituting Eq. (6) into Eq. (4) leads to Eq. (7) around the roll axis.

$$\dot{p} = (c_1 r + c_2 p)q + c_3 M_{xa}(u, v, w, p, q, r) + c_3 M_{xc}(V, \delta_a, \delta_e, \delta_r) + c_4 M_{za}(u, v, \dot{w}, w, p, q, r) + c_4 M_{zc}(V, \delta_a, \delta_e, \delta_r) \quad (7)$$

In the body frame the components of the free stream velocity V are defined as u, v, w . The control surface deflections are denoted by $\delta_a, \delta_e, \delta_r$ for the ailerons, elevator and rudder respectively. Around the pitch axis substituting Eq. (6) into Eq. (4) leads to Eq. (8).

$$\dot{q} = c_5 p r - c_6 (p^2 - r^2) + c_7 M_{ya}(u, v, w, \dot{w}, p, q, r) + c_7 M_{yc}(V, \delta_a, \delta_e, \delta_r, \delta_t) \quad (8)$$

A second derivative term is incorporated for the vertical velocity component \dot{w} . The thrust of the propeller is defined as δ_t .

The goal of this paper is to control the attitude of the MAV. Euler angles are used to define the orientation of the body frame with respect to the earth frame.¹⁶ Starting in the earth frame the MAV is rotated by an angle ψ around the yaw axis, θ around the pitch axis and ϕ around the roll axis.¹⁶ The kinematic attitude equations Eq. (9) for a flat non-rotating earth are used to relate the angular rates to the Euler angles.¹⁶

$$\begin{aligned}\dot{\phi} &= p + q \sin \phi \tan \theta + r \cos \phi \tan \theta \\ \dot{\theta} &= q \cos \phi - r \sin \phi \\ \dot{\psi} &= q \frac{\sin \phi}{\cos \theta} + r \frac{\cos \phi}{\cos \theta}\end{aligned}\quad (9)$$

III. Incremental Nonlinear Dynamic Inversion

The angular accelerations around the body axes defined by Eq. (5) can be written in an incremental form by applying a Taylor series expansion. The resulting equation is used by the controller to predict the angular acceleration one step ahead in time based on the current time point.¹²

A. Roll axis

Three eigenmotions characterize the behavior of the MAV around the roll axis: the aperiodic roll, the dutch roll and the spiral. Slow motions can be damped out by the controller whereas fast motions determine the behavior of the MAV to aileron inputs. The aperiodic rolling motion is therefore used to model the angular acceleration. During this maneuver the MAV is flown at a constant speed V of 10m/s with $\Delta u = 0$. The yawing motion and rudder input are neglected: $\Delta v = 0$ $\Delta \dot{v} = 0$ $\Delta r = 0$ $\Delta \delta_r = 0$. Due to this assumption the yaw moment M_z can be omitted from the equation.¹⁶ The asymmetric and symmetric motions are considered decoupled. The effects of the symmetric motions are neglected: $\Delta \delta_e = 0$ $\Delta w = 0$ $\Delta q = 0$. Applying a Taylor series expansion to Eq. (7) with the above mentioned assumptions leads to Eq. (10).

$$\dot{p} = \dot{p}_0 + \left. \frac{\partial(c_3 M_{xa})}{\partial p} \right|_{p=p_0} (p - p_0) + \left. \frac{\partial(c_3 M_{xc})}{\partial \delta_a} \right|_{\delta_a=\delta_{a0}} (\delta_a - \delta_{a0}) \quad (10)$$

The partial derivative of the aerodynamic moment $\frac{\partial(c_3 M_{x_a})}{\partial p}$ is defined as F_p . The partial derivative of the control moment $\frac{\partial(c_3 M_{x_c})}{\partial \delta_a}$ is defined as G_{δ_a} , simplifying Eq. (10) to Eq. (11).

$$\Delta \dot{p} = F_p \Delta p + G_{\delta_a} \Delta \delta_a \quad (11)$$

A least-square fitting method is used to determine F_p and G_{δ_a} . Data was collected by performing outdoor test flights. In total 90 seconds of flight test data are used, 80% for the training set and 20% for the test set. An airspeed controller was used to maintain the cruise speed at 10m/s. During the flight p and δ_a were logged. \dot{p} can be calculated by differentiating the angular rate. The change in \dot{p} is too noisy to be used directly for the fit, all signals are therefore filtered with the same second order low pass filter given by Eq. (12) with $w_n = 15.9$ Hz and $\zeta = 0.65$.

$$H(s) = \frac{\omega_n^2}{s^2 + 2\zeta\omega_n s + \omega_n^2} \quad (12)$$

The root mean square error of the test set and training set differ by 2% indicating the model is not over-fitted. The model parameters are $F_p = -16 \pm 1$ [1/s] and $G_{\delta_a} = 212 \pm 6$ [rad/(s²rad)]. The INDI controller is based on the principle of time scale separation¹²⁶ simplifying Eq. (11) simplifies to Eq. (13).

$$\Delta \dot{p} = G_{\delta_a} \Delta \delta_a \quad (13)$$

It is important to compare the angular acceleration prediction of the INDI controller with damping Eq. (11) and without damping Eq. (13). The root mean square error of the model without damping is 0.4% higher compared to the model with damping. The comparison of the two models and the measured change in angular acceleration is given in Figure 1.

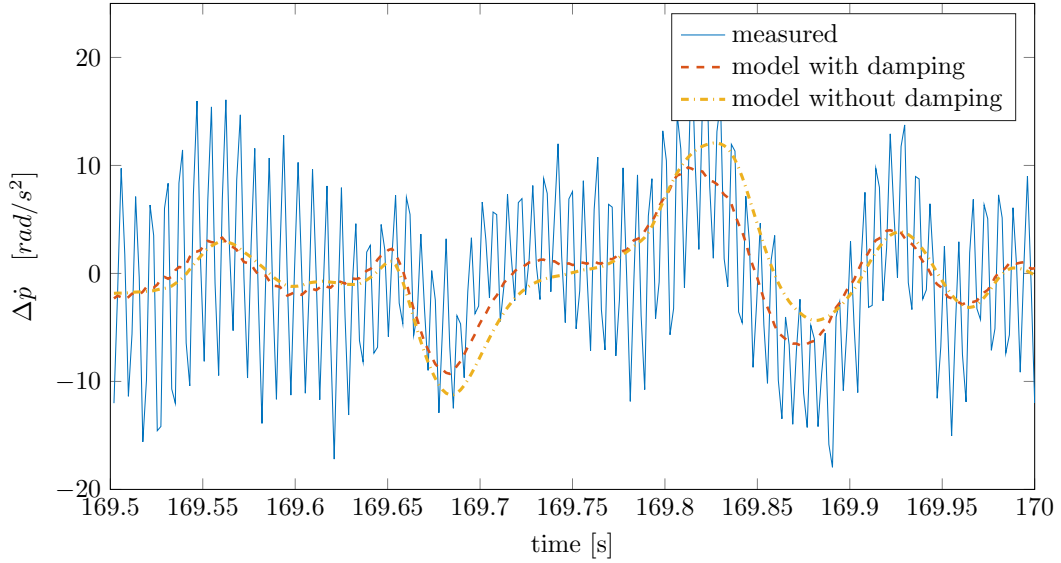


Figure 1: Measured and modeled angular acceleration around the roll axis at 10m/s

B. Pitch axis

Around the pitch axis the motion is characterized by the short period and the phugoid. The phugoid is a slow and slightly damped motion which can be easily compensated by the controller. The focus lays on the short period motion which is highly damped and very fast. During this maneuver the MAV is considered in level flight at a constant speed V of 10m/s, leading to $\Delta u = 0$.¹⁶ The thrust input is kept constant: $\Delta \delta_t = 0$. The asymmetric motions are considered negligible leading to $\Delta v = 0$ $\Delta p = 0$ $\Delta r = 0$ $\Delta \delta_a = 0$ $\Delta \delta_r = 0$. The second order derivative is neglected $\Delta \dot{w} = 0$. With these assumptions Eq. (8) is simplified to Eq. (14).

$$\dot{q} = \dot{q}_0 + \left. \frac{\partial(c_7 M_{y_a})}{\partial w} \right|_{w=w_0} (w - w_0) + \left. \frac{\partial(c_7 M_{y_a})}{\partial q} \right|_{q=q_0} (q - q_0) + \left. \frac{\partial(c_7 M_{y_c})}{\partial \delta_e} \right|_{\delta_e=\delta_{e0}} (\delta_e - \delta_{e0}) \quad (14)$$

The partial derivatives of the aerodynamic moment are defined as $F_q = \frac{\partial(c_7 M_{y_a})}{\partial q}$ and $F_w = \frac{\partial(c_7 M_{y_a})}{\partial w}$. The control effectiveness is defined as $G_{\delta_e} = \frac{\partial(c_7 M_{y_e})}{\partial \delta_e}$ leading to Eq. (15).

$$\Delta \dot{q} = F_w V \Delta \alpha + F_q \Delta q + G_{\delta_e} \Delta \delta_e \quad \alpha = w/V \quad (15)$$

To measure the angle of attack the MAV is placed in a pitch rig set-up. In the rig the MAV can only rotate around the pitch axis which passes through the center of gravity. In this set-up the angle of attack α is considered equal to the pitch angle θ . A least-square fitting method is used to determine F_w , F_q and G_{δ_e} . Data was collected by giving open loop doublet inputs while the MAV was placed in the pitch rig in the wind tunnel at a speed of 10m/s. In total 45 seconds of flight test data are considered, 80% for the training set and 20% for the test set. During the flight q , θ and δ_e are logged. \dot{q} can be calculated by differentiating the angular rate. To decrease the noise level, all signals are filtered with the same second order low pass filter given by Eq. (12) with $w_n = 15.9$ Hz and $\zeta = 0.65$. The root mean square error of the test set and training set differ by only 0.2% indicating the amount of data points is sufficient to make a good fit. The model parameters are $F_w = -31.7 \pm 0.3$ [$\frac{rad}{m.s}$], $F_q = -8.3 \pm 0.2$ [1/s] and $G_{\delta_e} = 73 \pm 1$ [$rad/(s^2 rad)$]. The damping term F_w and the control effectiveness G_{δ_e} are in the same order of magnitude. This indicates the principle of time scale separation is theoretically no longer valid.⁶ It is however, difficult to predict the value of the term $\Delta \alpha$ for the next time point. The INDI controller is therefore designed based on Eq. (16) considering errors can be present due to the effect of the damping term F_w .

$$\Delta \dot{q} = G_{\delta_e} \Delta \delta_e \quad (16)$$

The root mean square error of the model without damping is 22% higher compared to the model with damping. The increase in root mean square error is mainly due to the open loop response which includes a slow damping motion which is not captured by the initial elevator input. The damping is slower compared to the initial change in acceleration due to the elevator input and can therefore be compensated by a closed loop control structure. The comparison of the two models and the measured change in angular acceleration is given in Figure 2.

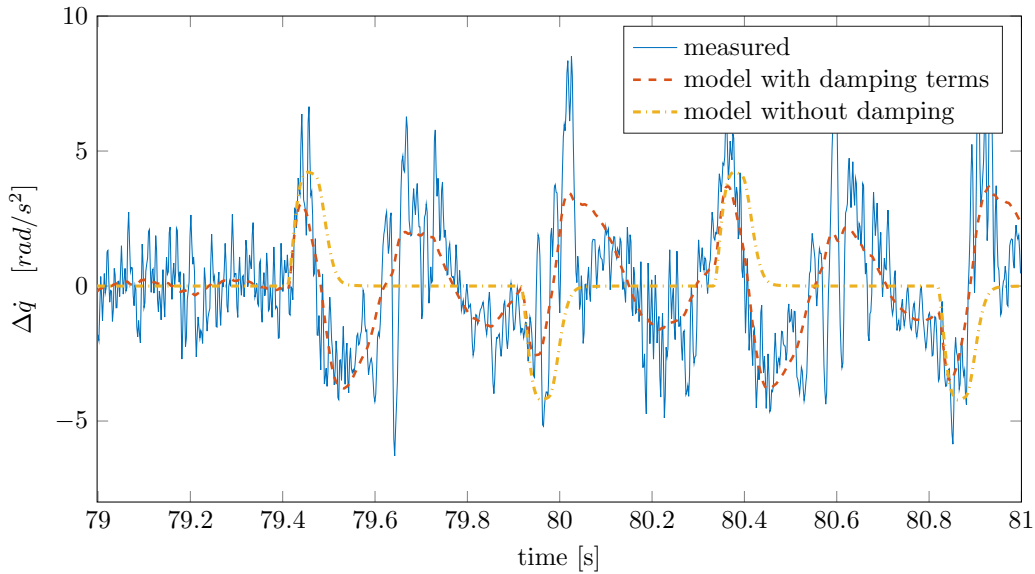


Figure 2: Measured and modeled angular acceleration around the pitch axis at 10m/s

C. Implementation

The INDI control scheme has the form given in Figure 3 and Figure 4 based on Eq. (13) and Eq. (16). The virtual control input v denotes the reference acceleration of the system which is compared to the measured acceleration \dot{p}_f for roll and \dot{q}_f for pitch. The subscript f is used to denote all signals which have been filtered with second order low pass filter $H(s)$. The inverse of the control effectiveness G is used to calculate the

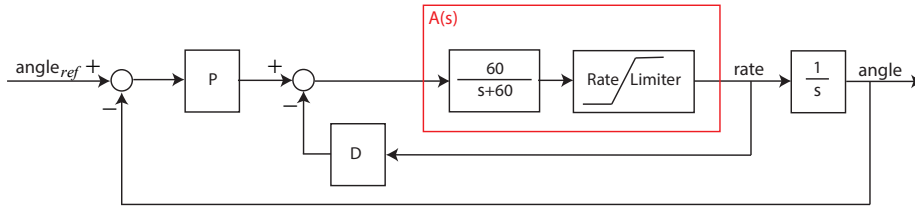
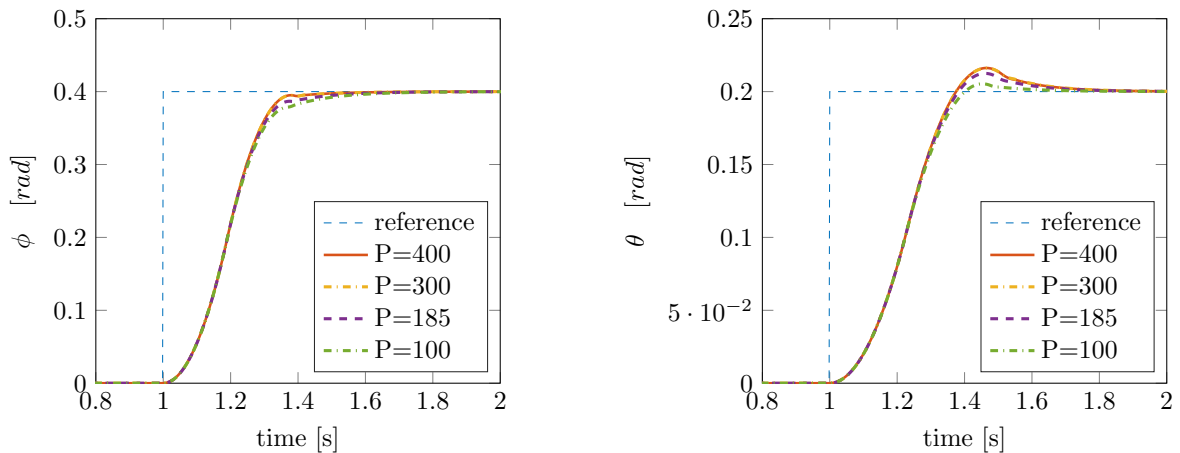


Figure 5: Linear gains analysis

The actuator dynamics block contains a first order system and a rate limiter which is influenced by the control effectiveness G . Due to the rate limiter, increasing the PD gains does not necessarily lead to a faster reference tracking performance. Above a certain threshold the linear gains of the INDI controller can be increased without increasing the performance of the system. During high turbulence intensities the system is considered to be operating in the range influenced by the rate limiter. The closed-loop response is analyzed for a step input of 0.2 rad for pitch and 0.4 rad for roll. Figure 6 shows the performance of the model with the parameters from Eq. (17) for $P = 100, 185, 300$ and 400. The ratio between the proportional and derivative gain should remain constant leading to a corresponding set of derivative gains $D = 12, 22, 36$ and 48. This shows that a drawback of using a higher P gain is the amplification of the noise in the roll and pitch rate signals due to a higher D gain. Figure 6 shows that the response of the system for a range of proportional gains is identical except for the last part of the step response where the first order system determines the behavior.



(a) Roll angle tracking of a step input of 0.4 radians

(b) Pitch angle tracking of a step input of 0.2 radians

Figure 6: Reference tracking performance for varying PD gains

Around the roll axis, the linear gains are designed to obtain a rise time of 0.22 sec given a step input of 0.4 rad without overshoot. This leads to $P = 185$ and $D = 22$. For pitch, the reference tracking for a step input of 0.2 rad is designed to give a rise time of 0.23 sec and a small overshoot of 6%. This leads to the same set of gains $P = 185$ and $D = 22$.

Assuming the actuators are a first order system, a comparable reference tracking performance is obtained when the PID controller uses the same PD gains as the INDI controller.¹² Figure 6 shows that this assumption is not always valid for a rate limited system, as a range of gains can lead to the same reference tracking performance. The PID gains used in this paper were manually tuned to obtain comparable rise time and overshoot properties. For roll, the manually tuned P gain is 1.6 times higher compared to the INDI gain. The D gain used in the PID structure is 0.7 times lower compared to the INDI gain. The ratio between the proportional and derivative gain should theoretically be identical as it is not affected by the rate limiter. For pitch, the P gain was found to be 0.7 times lower compared to INDI. The D gain cannot be compared

for the pitch axis as the PID controller uses the derivative of the error instead of the gyro signal to damp the system. Additional flight tests should be performed to evaluate the effect of adapting the PID gains to match the exact values used by the INDI controller. Differences in the ratio between the proportional and derivative gain show that the damping terms play a role in the response of the system. To determine the theoretical influence of the damping terms on the D gain more research should be performed.

IV. Phased-advanced pitch probes

The pressure probes system designed by Mohamed et al.² is used in the same configuration for the tests presented in this paper. The probe head is connected to a differential pressure sensor through acrylic tubes embedded in the wings. The probe is placed 15 centimeters ahead of the wing to create a 15 milliseconds time advantage. The pitch probe sensors are implemented as feed-forward components to both ailerons separately as shown in Figure 7.²

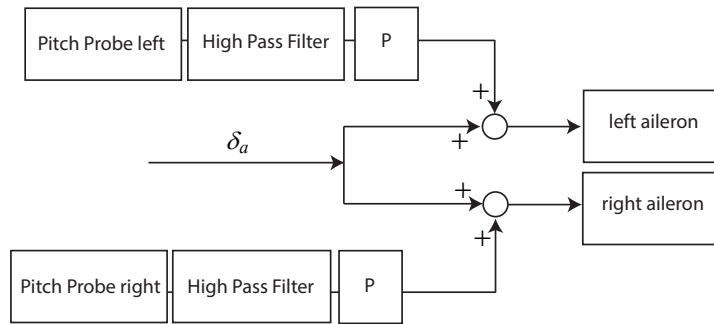


Figure 7: Feed-forward control probes²

The probes sense changes in angle of attack of the incoming flow caused by turbulence or by the pilot inputs. Mohamed et al.² showed that a linear relationship exists between the angle of attack measurement and the differential pressure measurement. To ensure that the probes are only reacting to turbulence a high pass filter is used. The pilot inputs have a low frequency range, by analyzing the flight test data the filter cut-off frequency was selected to be 4Hz. A fourth order Butterworth filter is used with the form given by Eq. (18).

$$H(z) = \frac{b(1)+b(2)z^{-1}+b(3)z^{-2}+b(4)z^{-3}+b(5)z^{-4}}{a(1)+a(2)z^{-1}+a(3)z^{-2}+a(4)z^{-3}+a(5)z^{-4}} \quad (18)$$

With $b = [0.7194 \ -2.8774 \ 4.3162 \ -2.8774 \ 0.7194]$ and $a = [1 \ -3.3441 \ 4.2389 \ -2.4093 \ 0.5175]$.

V. Experimental set-up



Figure 8: Slick 360 Micro

Figure 8 shows the results the MAV is flown completely autonomously with a vertical, longitudinal and lateral position control system. Turbulence was generated in the wind tunnel by using static grids. Outdoor flights were performed to test the system in turbulence intensities which are common in urban environments.

A. OJF

The OJF tunnel cross section is 285×285 cm. In the wind tunnel the coordinate system is defined as: X_w to the right perpendicular to the flow direction, Y_w in the direction of the tunnel flow and Z_w to the top of the wind tunnel. The origin of the axis system is given in Figure 9 in the middle of the cross section underneath the tunnel inlet. The heading is defined as 0 deg in the flow direction. The position is measured by 12 camera's of the Optitrack system. The infrared camera's measure the distance to 4 reflective markers placed on the MAV. The position data is sent to the MAV at 20Hz.

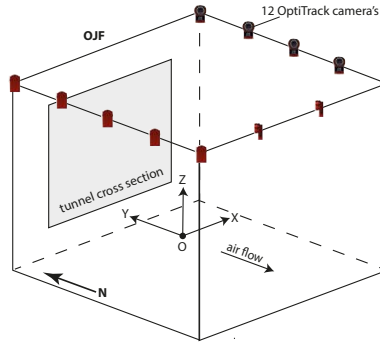


Figure 9: OJF wind tunnel coordinate system definition

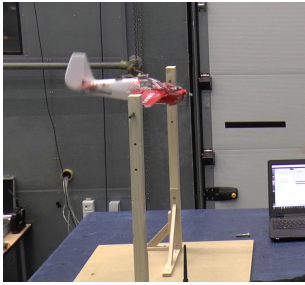


Figure 10: Pitch rig set-up

The pitch rig wind tunnel tests were performed to analyze the short period motion. The rig consists of a wooden construction attached to the tunnel floor and a movable rod connected to the wooden frame through low friction bearings. The rotational axis of the rig passed through the quarter chord line which corresponds to the center of gravity of the MAV. The pitch rig set-up is shown in Figure 10.

To replicate high levels of turbulence intensity static grids were placed at the test section inlet. The grids are built up of metal rods evenly spaced in the vertical direction and connected at the edges as shown in Figure 11. The turbulence intensity profile and the turbulence length scale have not been defined for this set-up due to leaks in the pressure probe measurement system during testing. Close to the grids wake turbulence is generated which slowly decays into homogeneous turbulence.¹⁵ This

decay is captured by the variation of the turbulence intensity in the flow direction. Due to the uneven grid structure the lateral and vertical turbulence spectrum should also be determined for this set-up as they can influence the results. The results shown in Section VI are therefore considered for parts of the flight executed at the same $\{X_w, Y_w, Z_w\}$ position.

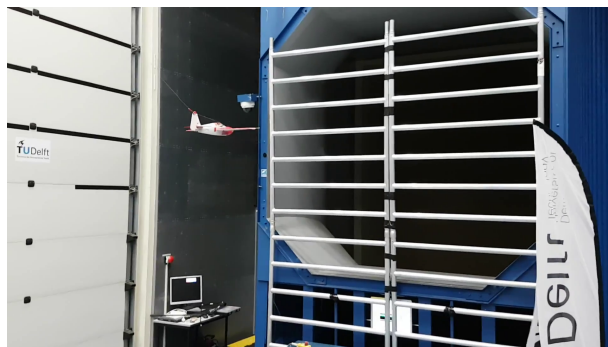


Figure 11: Turbulence grids set-up

B. Position Control

Autonomous flight in the wind tunnel poses a series of challenges. The MAV has to fly in a box with a maximum cross section of 285×285 cm. The position in the flow direction has to be constant to ensure the same level of turbulence intensity is experienced throughout multiple flights. Fixed-wing MAVs normally control the position based on the course as they fly from one waypoint to the next. In the wind tunnel set-up the course angle cannot be used as the position of the MAV is constant and the MAV is effectively hovering. In this set-up the heading angle has to be measured to control the lateral position. Finally the position data have to be communicated to the MAV at a high rate to ensure small deviations in speed and position can be counteracted. All these challenges have been taken into account during the design of the position control loops.

1. Vertical and longitudinal control

The throttle is used to control the vertical and longitudinal displacements. During outdoor flights the throttle is only used for the climb and descent phases and therefore always combined with a corresponding pitch angle. In this set-up an additional block is added to control the longitudinal position creating a coupling between the vertical and longitudinal displacements. The vertical controller uses the altitude error to calculate the reference climb rate. The altitude error is the difference between the reference altitude defined in the flight plan and the altitude z measured by the OptiTrack system. Each climb rate is associated with an increase in throttle level added to the cruise throttle. The cruise throttle is not constant in this set-up as it depends on the longitudinal position error. The longitudinal position y is compared to the reference position defined in the flight plan. A standard PID control structure is used to calculate the cruise throttle. The throttle control loop structure is shown in Figure 12. The green blocks highlight the required adjustments to fly in a wind tunnel environment.

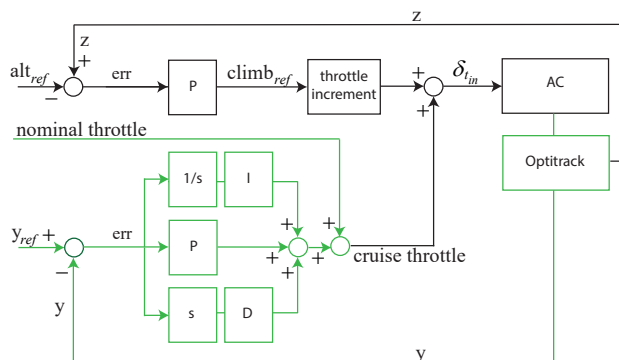


Figure 12: Vertical and longitudinal throttle control

The reference pitch angle is calculated based on the reference climb rate. The climb rate calculation, shown in Figure 13, depends on the altitude error. The standard altitude controller used during outdoor flights is extended with a integral gain I. The integrator ensures small offsets are eliminated to prevent position displacements outside the tunnel cross section. Changes in the vertical speed error are used to calculate the required pitch setpoint in combination with a feed-forward term based on the climb reference.

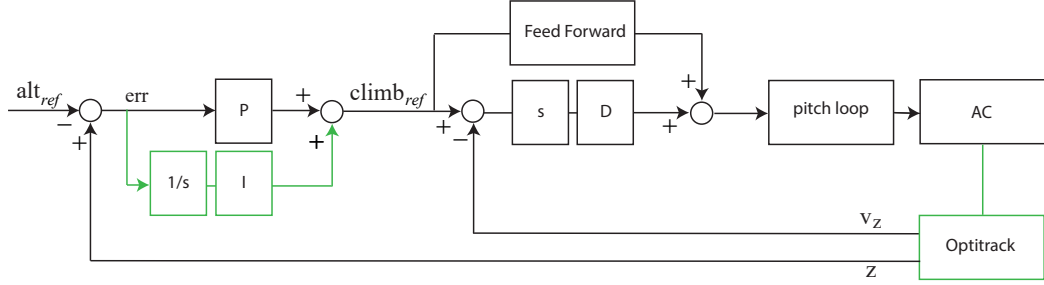


Figure 13: Vertical pitch control

2. Lateral control

The lateral controller compares the desired course angle with the current heading angle ψ measured by the OptiTrack system. The reference course angle χ_{ref} is defined as the arctangent of the x and y distances between the MAV and the desired waypoint. A PD controller is used to calculate the roll angle setpoint based on the course error. An overview of the lateral position control block is given in Figure 14.

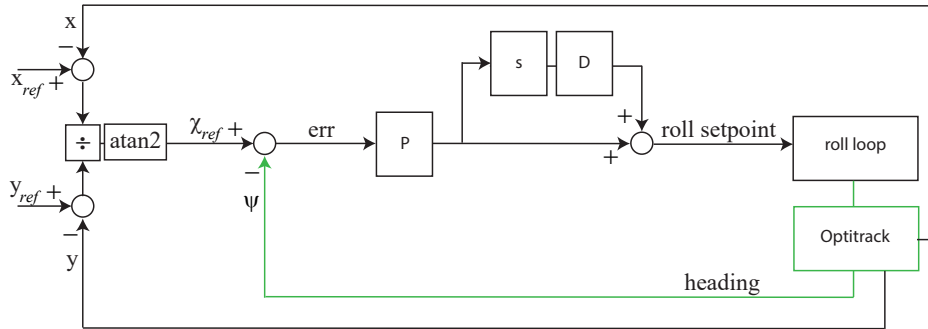


Figure 14: Lateral roll control

C. Outdoor test flights

The flight tests were performed in a field surrounded by trees to ensure the MAV is constantly subject to turbulence generated by the surrounding objects. The speed of the MAV was kept constant at 10m/s by using a proportional integral (PI) airspeed controller to regulate the throttle level. The attitude was controlled by the test pilot. The turbulence length scale can be estimated by using the von Karman model given by Eq. (19).¹⁵

$$S_{\bar{u}\bar{u}}(f) = \frac{4\sigma^2 L_x}{V} \frac{1}{\left(1 + 70.8 \left(\frac{L_x f}{V}\right)^2\right)^{\frac{5}{6}}} \quad (19)$$

$S_{\bar{u}\bar{u}}$ is the power spectral density as a function of the frequency f expressed in Hz. The power spectral density follows a -5/6 decay law as can be seen by the denominator of the function. σ is the standard

deviation of the flow and L_x the turbulence length scale.

VI. Results

A. Wind Tunnel Flights

Preliminary results were obtained by autonomously flying the MAV in the OJF. The results were obtained with approximate values of the control effectiveness, linear gains and filter cut-off frequency. The parameters calculated in Section III are summarized in Table 1 and Table 2 and compared to the preliminary parameters used during the autonomous wind tunnel tests. The preliminary parameters have been empirically selected.

Table 1: Preliminary and final parameters of the INDI controllers

	Roll		Pitch	
	Preliminary	Final	Preliminary	Final
P	400	185	400	185
D	22	22	22	22
G	0.019	0.022	0.014	0.008
ω_n	3.2	15.9	1.6	15.9

Table 2: Preliminary and final parameters of the PID controllers

	Roll		Pitch	
	Preliminary	Final	Preliminary	Final
P	12500	15000	4500	16000
I	1	30	1	30
D	700	700	1.5	1.5

The PID controller, with preliminary tuning parameters, proved to be very difficult to fly autonomously in the wind tunnel. The longest time period the PID controller was flown in the wind tunnel is 18 seconds. The INDI controller proved to be very precise and able to maintain the position within a 1x1x1 meter box during all flights. The performance of INDI and PID is evaluated for the same time frame and for the the same position in the wind tunnel. The $\{X_w, Y_w, Z_w\}$ position in the tunnel measured during the test for the two controllers is shown in Figure 17. The results given in Figure 15 and Figure 16 show that the range of the probability density function for the roll angle error decreases by 40% with the INDI controller compared to the PID controller. For the pitch angle the range decreases by 43% for INDI compared to PID. The probability density functions of the PID controller for roll and pitch are not centered around zero. This indicates that the integral gains should be increased to obtain a better performance. The integral gains were therefore increased by a factor 30 for the final test flights, as shown in Table 2.

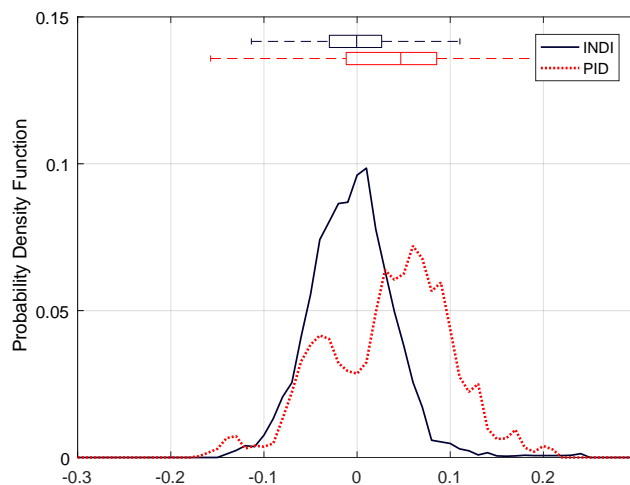


Figure 15: Comparison of roll angle perturbation for the PID and INDI controller

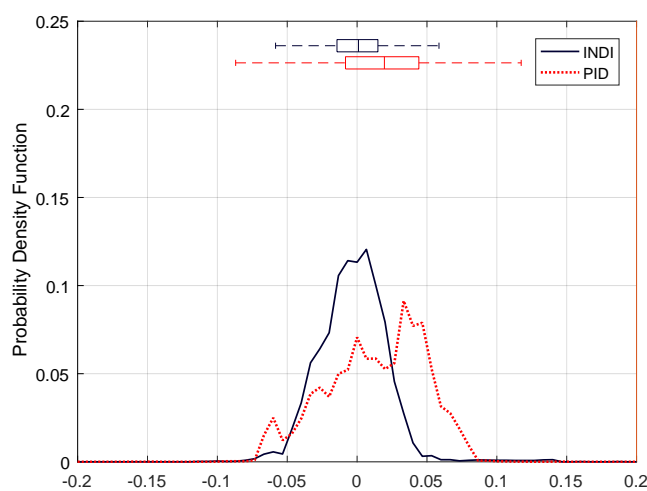


Figure 16: Comparison of pitch angle perturbation for the PID and INDI controller

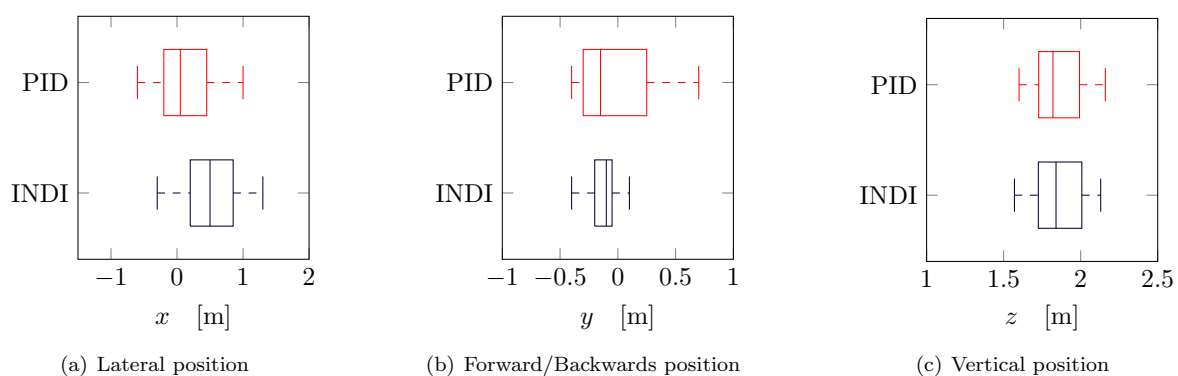


Figure 17: Position variation comparison between INDI and PID

B. Outdoor flights

The reference tracking performance of the INDI controller around the roll axis is shown in Figure 18(a). The rise time of the step input given from 0 to 0.4 radians is on average 0.15 sec which is faster than the expected rise time obtained with the closed loop analysis in subsection D of Section III. Overshoot is also present in all three responses with an average value of 10%. The reference tracking performance of the PID controller around the roll axis is shown in Figure 18(b) with an average rise time of 0.19 sec. The overshoot is on average 5%. These tests were performed outdoors on the same day as the disturbance rejection tests during high levels of turbulence intensity. Turbulence can lead to unexpected roll inputs which affect the reference tracking performance of the two controllers.

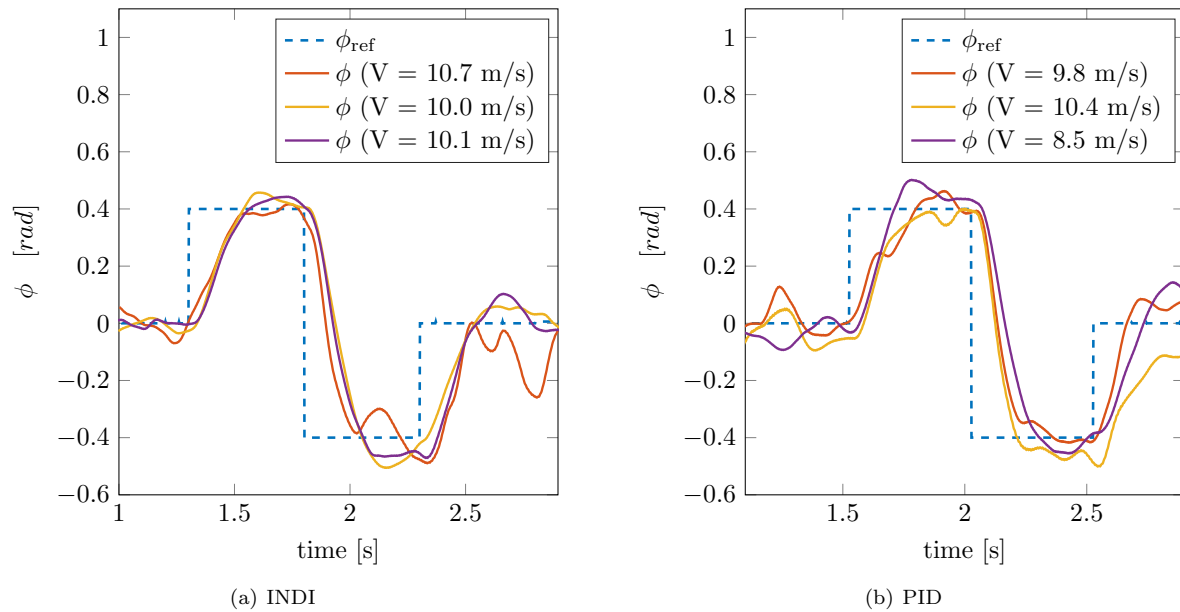


Figure 18: Reference tracking performance around the roll axis

The reference tracking performance of the INDI controller around the pitch axis is shown in Figure 19(a). The rise time for the test performed at 10.6 m/s is 0.37 sec and the overshoot 13%. The variation between the three curves is due to the high levels of turbulence experienced during the flight and the different airspeeds at which the step inputs were given. The PID step response test was executed twice during this flight. The performance is difficult to assess due to the influence of high energy turbulence as shown in Figure 19(b). On a calm day the results obtained with the same PID gains show a very high performance as given in Figure 20. A small steady state-error is visible in the results indicating the tuning of the integral gain can be improved to eliminate the steady-state offset.

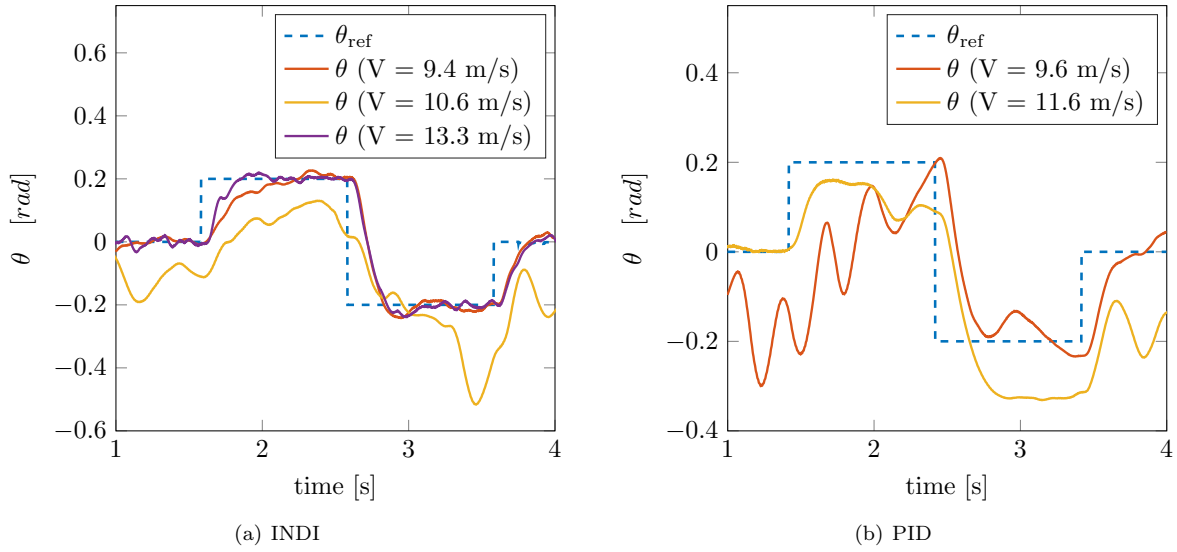


Figure 19: Reference tracking performance around the pitch axis during outdoor test in turbulence

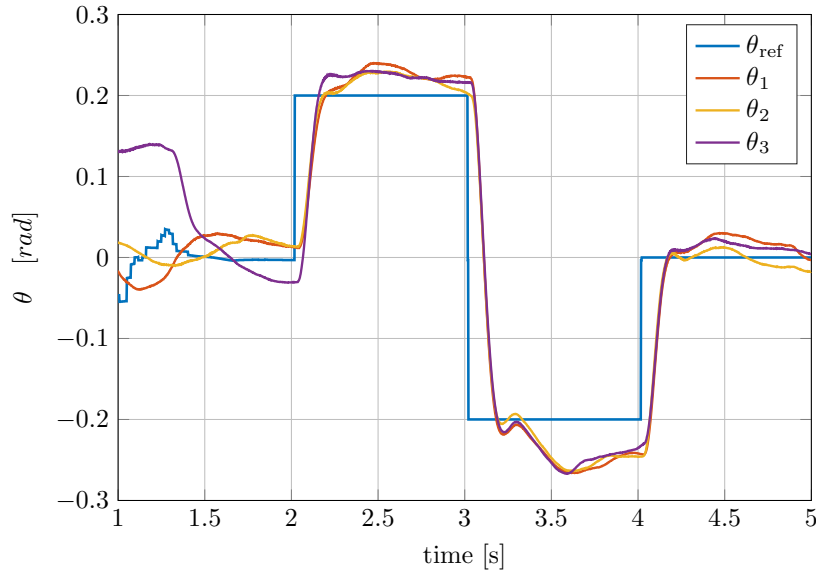


Figure 20: Pitch angle during the doublet for the PID controller in calm air at 10m/s

The disturbance rejection of the INDI controller and the PID controller with and without pitch probes was tested on the same day while flying the same trajectory multiple times. The analysis of all test flights showed that one of the pitch probes got obstructed during landing causing a bias in the measurements of the subsequent flights. Therefore no reliable data was obtained on the performance of the INDI controller in combination with the pitch probe sensors. The disturbance rejection performance is therefore analyzed for the other three control approaches. In total 120sec of reliable flight data are analyzed in this section, 40 seconds for each controller. The turbulence intensity level of the flight data is $T_i = 12.9\%$. The turbulence length scale is estimated by using the von Karman spectrum Eq. (19) to be 2.5 meters. The performance is evaluated for the part of the flight which used the airspeed controller to maintain the average velocity around 10m/s. The average velocity of the flight test data is 9.7 m/s. Figure 21(a) clearly shows an improvement in the probability density function of the roll angle error for the INDI controller compared to the PID controller. The box plot of the data given in Figure 21(b) shows that the range decreases by 21% for INDI compared to PID. The enhanced PID controller with the pitch probes does not show an improvement in performance

compared to the traditional PID controller. This result is not as expected from literature. Two main reasons have been identified which can influence the results: the high pass filter and degraded servos. The flight data show that the filtered probe values contain offsets. These offsets should have been eliminated by the high pass filter. The parameters used for the high pass filter during testing had a precision of 10^{-4} . By increasing the accuracy of the filter parameters to 10^{-6} all offsets are removed from the data. Another factor which was not taken into account is the degrading performance of the servos due to overheating. To eliminate this aspect the servos should be replaced after each test flight. Additional flight tests should be performed with accurate filter parameters and new servos to improve the performance of the pitch probe sensors.

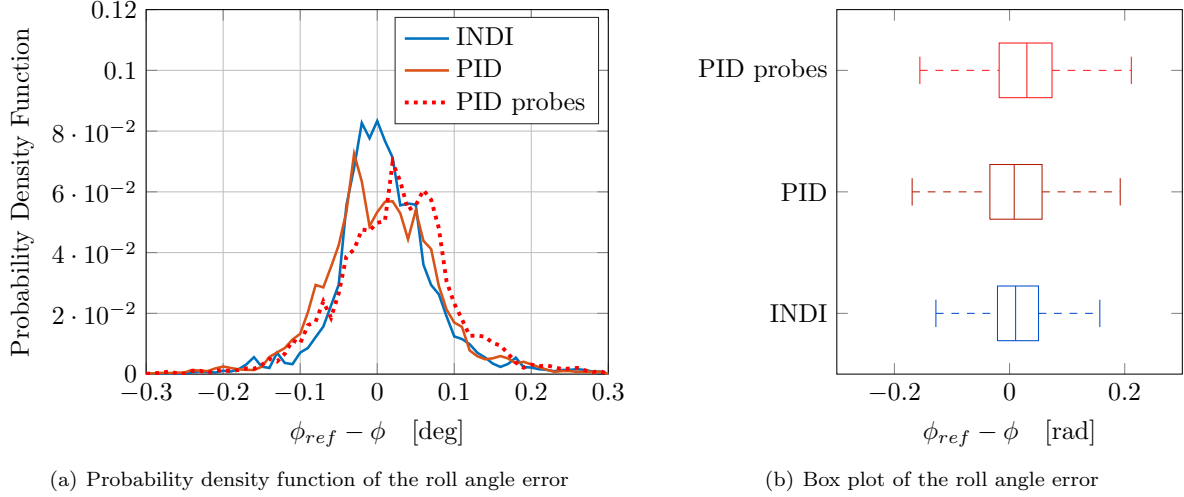


Figure 21: Disturbance rejection performance around the roll axis

The pitch angle error shown in Figure 22(a) also shows a clear improvement with INDI compared to PID. The box plot highlights the difference in Figure 22(b) which indicates that the range decreases by 24% for INDI compared to PID.

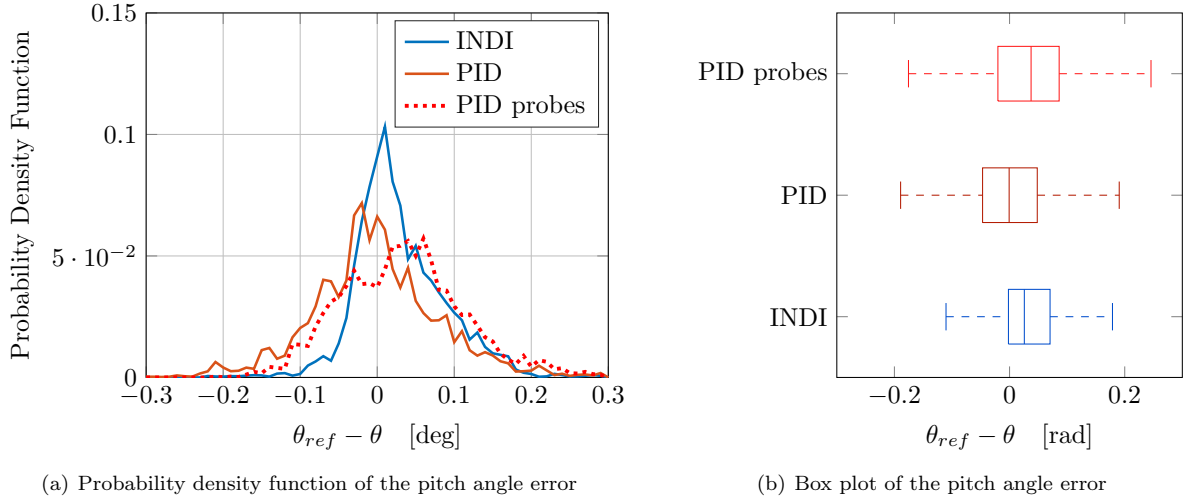


Figure 22: Disturbance rejection performance around the pitch axis

VII. Conclusion

This research shows the potential of incremental nonlinear dynamic inversion applied to fixed-wing micro air vehicles flown in high turbulence intensities. The angular acceleration measurements are predicted based

upon the control surface deflections eliminating the need for a complex aerodynamic model. To test the performance of the system a novel control solution is presented which allows autonomous free flight in a wind tunnel. The throttle is used for both the longitudinal and vertical control and the heading angle is used for lateral control. This experimental set-up eliminates all human factors and provides the opportunity to test in turbulence intensities which are beyond human capabilities. Autonomous free flight wind tunnel tests in turbulence were performed with estimates of the control effectiveness and the filter cut-off frequency. The performance of the estimated model is presented as it illustrates the robustness of the system. The results show that the controller eliminates all steady-state errors and counteracts accelerations caused by external disturbances making it a suitable solution for precise movements in the wind tunnel. Accurate model parameters for the control effectiveness, the actuators and the filter cut-off frequency are determined in this paper and used to assess the performance of the system during outdoor test flights. During outdoor flights the performance is compared to a proportional integral derivative controller tuned to obtain the same reference tracking performance. The nonlinear incremental controller significantly improves the disturbance rejection performance around both the roll and pitch axis. More research should be performed to assess the performance of the nonlinear controller compared to an enhanced linear controller with phase-advanced pitch probes.

VIII. Acknowledgments

The authors would like to thank the MAVLab team for the technical support throughout the project. In particular the authors would like to thank Christophe de Wagter for the excellent piloting skills, the critical review of the test procedure and the inspiring discussions. The authors would also like to thank the RMIT UAS Research Team for the valuable collaboration and their excellent knowledge on phase-advanced sensors.

References

- ¹Watkins, S., Mohamed, A., Fisher, A., Clothier, R., Carrese, R., and Fletcher, D. F., "Towards Autonomous MAV Soaring in Cities: CFD Simulation, EFD Measurement and Flight Trials," *International Micro Air Vehicles Conference and Flight Competition 2015*, 2015.
- ²Mohamed, A., Abdulrahim, M., Watkins, S., and Clothier, R., "Development and flight testing of a turbulence mitigation system for micro air vehicles," *Journal of Field Robotics*, Vol. 33, No. 5, 2016, pp. 639–660.
- ³Watkins, S., Millbank, J., Loxton, B. J., and Melbourne, W. H., "Atmospheric winds and their implications for microair vehicles," *AIAA Journal*, Vol. 44, No. 11, 2006, pp. 2591–2600.
- ⁴Slotine, J. J. E. and Li, W., *Applied Nonlinear Control*, Prentice-Hall, 1991.
- ⁵Lee, H. P., Reiman, S. E., Dillon, C. H., and Youssef, H., "Robust nonlinear dynamic inversion control for a hypersonic cruise vehicle," *AIAA Guidance, Navigation, and Control Conference and Exhibit*, 2007.
- ⁶Sieberling, S., Chu, Q., and Mulder, A. J., "Robust Flight Control Using Incremental Nonlinear Dynamic Inversion and Angular Acceleration Prediction," *AIAA Journal of Guidance, Control, and Dynamics*, Vol. 33, No. 6, 2010, pp. 1732–1742.
- ⁷Bordignon, K. and Bessolo, J., "Control allocation for the X-35B," *2002 Biennial International Powered Lift Conference and Exhibit*, 2002.
- ⁸Walker, G. P. and Allen, D. A., "X-35B STOVL Flight Control Law Design and Flying Qualities," *2002 Biennial International Powered Lift Conference and Exhibit*, 2002.
- ⁹Brinker, J. S. and Wise, K. A., "Flight testing of reconfigurable control law on the X-36 tailless aircraft," *AIAA Journal of Guidance, Control, and Dynamics*, Vol. 24, No. 5, 2001, pp. 903–909.
- ¹⁰Smith, P. R., "A Simplified Approach to Nonlinear Dynamic Inversion Based Flight Control," *AIAA Atmospheric Flight Mechanics Conference and Exhibit*, 1998.
- ¹¹Bacon, B. J. and Ostroff, A. J., "Reconfigurable Flight Control Using Nonlinear Dynamic Inversion with a Special Accelerometer Implementation," *AIAA Guidance, Navigation, and Control Conference and Exhibit*, 2000.
- ¹²Smeur, E. J. J., Chu, Q., and de Croon, G. C. H. E., "Adaptive Incremental Nonlinear Dynamic Inversion for Attitude Control of Micro Aerial Vehicles," *AIAA Journal of Guidance, Control, and Dynamics*, Vol. 39, No. 3, 2016, pp. 450–461.
- ¹³Vlaar, M. C., "Incremental Nonlinear Dynamic Inversion flight control implementation and flight test on a fixed wing UAV," Master thesis, Delft University of Technology, Delft The Netherlands, Feb. 2014.
- ¹⁴Mohamed, A., Watkins, S., Clothier, R., and Abdulrahim, M., "Influence of Turbulence on MAV Roll Perturbations," *International Journal of Micro Air Vehicles*, Vol. 6, No. 3, 2014, pp. 175–190.
- ¹⁵Ravi, S., *The influence of turbulence on a flat plate aerofoil at Reynolds numbers relevant to MAVs*, Ph.D. thesis, RMIT, Melbourne, Victoria, Australia, 2011.
- ¹⁶Cook, M. V., *Flight Dynamics Principles*, Elsevier, 2007.
- ¹⁷Sonneveldt, L., *Adaptive Backstepping Flight Control for Modern Fighter Aircraft*, Ph.D. thesis, Delft University of Technology, Delft, The Netherlands, 2010.

II

THESIS

1

INTRODUCTION

Micro Air Vehicles (MAVs) are becoming increasingly popular and are being used for a large variety of applications such as exploration of urban environments by autonomously planning the flight path [1] or search and rescue missions in remote areas [2]. In particular, fixed-wing MAVs have the ability to fly long distances but at the same time perform steep maneuvers in the vicinity of buildings and urban areas. In light of the growing number of MAVs used for commercial applications Delft University of Technology (TU Delft) and the Royal Melbourne Institute of Technology (RMIT) have taken interest in improving the safety and reliability of MAVs.

At RMIT, the research is focused on understanding which types of turbulence are most critical for MAVs. Due to the large surface wing area MAVs have the most difficulty in counteracting gusts which occur around the roll axis [3]. Inspired by nature they developed a phase-advanced sensor which has the same function as the leading edge feathers of birds. Birds use the feathers to measure the changes in flow pitch angle and velocity [4]. The sensor is a multi-hole pressure probe that can reconstruct the flow velocity vector in three dimensions [4]. The information from the sensor is then used by the control system to react to the gust before it has a deleterious effect on the wing. The incoming flow angle and velocity are used as a feed-forward term in the PID control architecture for attitude control [4]. Flight tests have been performed by RMIT both in the wind tunnel and outdoors in various turbulence intensities and showed major improvements in attitude control around both the roll, pitch and yaw axis [4].

At TU Delft, state of the art research is done on nonlinear control techniques to improve disturbance rejection. Most controllers which are commercially available use PID loops to regulate the system response. These controllers however do not always work as required when applied to nonlinear systems like an airplane subject to strong wind gusts [5]. A promising control technique is INDI, a nonlinear controller that uses the actuator dynamics and the angular acceleration to determine the change in control input. The main advantage of this technique is that any measured dynamics, which are not part of the model, will be compensated [5]. Flight tests have been done with INDI to assess disturbance rejection for attitude control and position control. A disturbance in the attitude of the quadrotor was created by using a mass placed at an off-center position [5]. This test showed promising results as the INDI controller was able to recover from the disturbance 5 times faster than the PID controller [5]. Position control using INDI was tested on a quadrotor while flying between two waypoints in and out of a turbulence generating fan [6]. The results showed that the INDI controller performed 3 times better than the PID controller in terms of average position error [6]. Although these tests were conducted on a quadrotor, this research shows potential for fixed-wing aircraft.

The goal of this thesis is to improve attitude control of fixed-wing MAVs subject to turbulence by combining the phased-advanced sensors with an INDI controller. This thesis will give new insights into the use of phase advanced sensors for attitude control and the use of inner loop INDI for fixed wing aircraft in combination with these sensors.

Chapter 2 presents the state of the art research which brings to light knowledge gaps that still need to be investigated. The identified knowledge gaps are used to formulate the research question. The MAV model is described in Chapter 3 and the control techniques are given in Chapter 4. The experimental set up used to answer the research question is given in Chapter 5. The results and the added value of the research to the body of knowledge is described in Chapter 6.

2

LITERATURE STUDY

This section describes the state of the art research on turbulence mitigation systems from a control perspective and from a sensor perspective. The first part of this chapter outlines the research on nonlinear control techniques and the second part describes turbulence and phase-advanced sensors. The identified knowledge gaps are used to formulate the research question which will be addressed in this master thesis project. The chapter will conclude with the relevance of this thesis project to the body of knowledge in relation to the state of the art research.

2.1. CONTROL TECHNIQUES

In total four control strategies will be analyzed that can be applied to counteract gusts during the flight of an MAV: Proportional Integral Derivative (PID), Nonlinear Dynamic Inversion (NDI), Incremental Nonlinear Dynamic Inversion (INDI) and Adaptive Incremental Nonlinear Dynamic Inversion (AINDI). The controllers will be analyzed in terms of performance and applicability to select the best control strategy for this Master thesis work. Slotine [7] identified a number of reasons to focus on nonlinear controllers opposed to linear controllers. The first reason is that linear controllers assume that the system will be operating in a small range where the linear model is valid [7]. When dealing with high turbulence intensities, the MAV can experience large changes in roll and pitch angle. These changes cause the aircraft to experience high angles of attack and large bank angles in which the behavior of the system is nonlinear. When using a linear PID controller, gain scheduling is used to maintain the same performance. This may be counterintuitive, but gain scheduling can be much more difficult to implement compared to nonlinear control systems due to the large amount of linearization points required to obtain a good performance. As stated by Slotine [7] simplicity is another advantage of nonlinear control. Every control systems has to deal with friction, dead zones and saturation, these properties cannot be linearized and require a nonlinear controller to predict the system response [7]. Finally, Slotine [7] states that model uncertainties can be larger for nonlinear control systems. The goal of this literature review is to explore the advantages and disadvantages of each control technique to identify the appropriate controller for turbulence mitigation for MAVs.

2.1.1. PID

PID was introduced before World War II and used extensively during the war due to the high demand of automation [8]. According to Ang et al. [9] the PID controller was invented in 1910 by Elmer Sperry who applied it to automatic ship steering. At that time the controller was implemented in pneumatic or electrical form whereas nowadays it is programmed in a computer in digital form [10]. It is still used extensively today in all sort of applications mainly due to the robustness of the system and the ease of implementation. The main difficulty of a PID controller is tuning the system gains such that the output signal has the desired response. A lot of rules of thumb have been developed over the years which have greatly helped with the success of this technique, such as the Ziegler–Nichols method developed 1942 [11]. PID controllers are error driven meaning they work based on a feedback mechanism that compares the actual value with the desired value.

$$u(t) = K_p e(t) + K_i \int_0^t e(\tau) d\tau + K_d \frac{de}{dt} \quad (2.1)$$

As outlined in Equation 2.1, the control input u is calculated as the sum of the Proportional, Integral and Derivative terms. The control error e is defined as the difference between the reference signal and the measured signal. The derivative term is the most difficult to tune and to implement [10]. This is mainly caused by the noise amplification when differentiating the error signal. For MAVs PID control is widely used for both attitude and position control, for example it is available on the Paparazzi autopilot [12] and on the Pixhawk flight controller [13]. The tuning of such a system is relatively easy and is mainly done in the field by increasing the P gain until the system starts oscillating, next increasing the D and I gain to achieve a stable output. It is therefore relatively easy to obtain a stable system especially for fixed wing aircraft as they are inherently stable. Achieving optimal tracking performance is more complicated, as analysis of flight data is required to check the rise time and the steady state error. In the Paparazzi autopilot system PID control can be used for both the attitude and position control loops [12]. The PID control loop structure is in this case augmented by the reference signal second order filter. This filter has been implemented to avoid abrupt changes in the reference signal thereby decreasing the response to load disturbances and decreasing the output oscillations induced by the input [14]. This filter allows the PID gains to be higher achieving a better performance. The main disadvantage of a PID controller is that the gains which are optimal for reference tracking are not optimal for disturbance rejection [6]. Smeur et al. [6] explain that increasing the integral term can be used to counteract a disturbance. This action however degrades the performance of the reference tracking as it causes more overshoot. In the MatLAB and Simulink software packages, PID controllers can be tuned automatically by the software. The gains that the program selects are by default set to balance the performance between reference tracking and disturbance rejection [15]. The focus can also be changed to favor one over the other, indicating the optimal gains are different depending on the design focus. For this Master Thesis Project disturbance rejection and reference tracking are both equally important in the design of the control system. On the one hand the MAV has to follow the flight path as defined by the flight plan, but on the other hand it has to counteract strong wind gusts along its trajectory.

2.1.2. NDI

Nonlinear dynamic inversion transforms the nonlinear system into a companion form by applying input and state transformation which results in a linear input-output relation. A nonlinear system is given by:

$$\dot{\underline{x}} = F(\underline{x}, u) \quad (2.2)$$

Can be transformed to companion form [16]:

$$\frac{dx}{dt} \begin{bmatrix} x_1 \\ \vdots \\ x_{n-1} \\ x_n \end{bmatrix} = \begin{bmatrix} x_2 \\ \vdots \\ x_n \\ b(x) + a(x)u \end{bmatrix} \quad (2.3)$$

The virtual control input v is defined such that the input-output linearization can be applied [16]:

$$v = \frac{dx_n}{dt} \quad (2.4)$$

$$u = a^{-1}(x)[v - b(x)] \quad (2.5)$$

The system now has two control loops as shown by Figure 2.1 [16]. The inner loop contains the nonlinear part of the system and the linear input-state relation. The outer loop is a linear control problem, therefore the gains can be chosen to achieve the desired response. If the gains of the outer loop are stable the stability of the entire system can be guaranteed [16]. For tracking problems the output equation has to be differentiated until the input appears. The number of differentiations define the relative degree of the system. NDI cannot be applied to all types of systems as not all systems lead to an input-output relationship, meaning the relative degree is not always defined [7]. Figure 2.1 [16] shows that the performance of the system is dependent on the accuracy of parameters a and b . If these parameters match with reality, the desired response can be achieved [17]. The advantages of NDI are the accuracy and precision of the system response. The disadvantages are the sensitivity to model inaccuracies, the measurement of all state variables and the limited applicability [7]. Solutions to the first problem were presented by Lee [17] by analyzing the robust singular value (μ) or by using neural networks as presented by Brinker [18]. For the second problem research is done on state observers [7]. Using certified aircraft models NDI was applied to the Lockheed Martin X-35 Joint Strike Fighter [19] and the NASA X-36 Tailless Aircraft [18] with excellent performance characteristics. NDI has not yet been applied to MAVs as these platforms have a much lower development cost compared to military platforms.

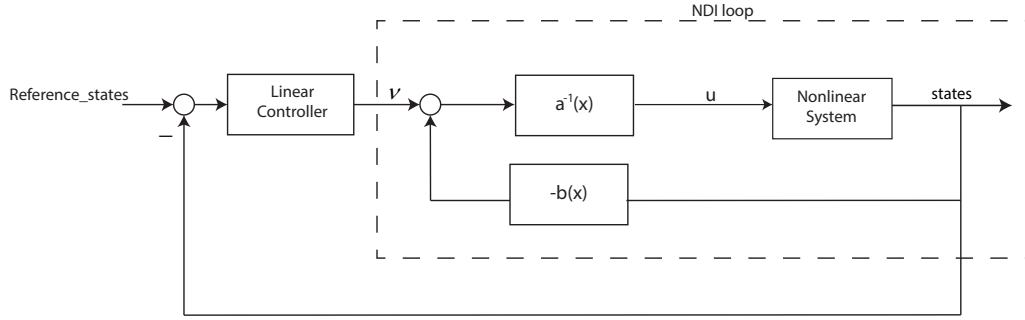


Figure 2.1: NDI control block structure[16]

2.1.3. INDI

As seen in the previous section NDI requires an accurate model and is therefore not easy to implement. Smith [20] presented a simplified version in 1998 later called INDI. Smith [20] derived a relationship between the angular accelerations and the control surface deflections from the aircraft equations of motion. The control law calculated the incremental input instead of the complete input. The derivation is based on the Taylor expansion of the system around the current time point and by applying the principle of time scale separation [16]. The Taylor expansion of the system has the following form [16]:

$$\dot{\underline{x}} = \dot{\underline{x}}_0 + F(\underline{x}_0, \underline{u}_0)(\underline{x} - \underline{x}_0) + G(\underline{x}_0, \underline{u}_0)(\underline{u} - \underline{u}_0) \quad (2.6)$$

If the sampling rate is high, the principle of time scale separation applies indicating the term $\underline{x} - \underline{x}_0$ can be neglected leading to [16]:

$$\Delta \dot{\underline{x}} = G(\underline{x}_0, \underline{u}_0)(\underline{u} - \underline{u}_0) \quad (2.7)$$

From Equation 2.7 it can be seen that the only model parameter is G . G represents the control effectiveness or in other words the relationship between the change in angular acceleration and the corresponding change in control surface deflection. The main advantage of INDI is now clearly visible, the control law is insensitive to changes in the aerodynamic coefficients and the centre of gravity as these are not included in the control law but captured as changes in the angular acceleration [21]. This theory was applied to a model of the McDonnell Douglas F/A-18 from NASA obtaining good results in terms of robustness to noise, model inaccuracies and limits on the actuator rate and authority [20]. Bacon and Ostroff [22] tested INDI on aircraft with actuator failure or actuator damage or loss. The results showed that the INDI controller could always operate inside the 6 dB and 5° phase margin except for uncertainties in the normal acceleration measurements [22]. Sieberling et al. [21] further developed INDI for platforms with inertial measurements units (IMUs) where gyroscopes are used to measure the angular rate. The angular rate needs to be differentiated in order to obtain the angular acceleration needed for the INDI control loop. Differentiating amplifies the noise of the state measurement increasing the error in the control loop structure. The solution proposed by Sieberling [21] consists of a predictive filter on the gyroscopes. Bacon et al. [23] proposed a second order washout filter on the angular rate and a lag filter on the incremental input. Smeur et al. [5] found that the best results are obtained when using the same filter on both the gyroscopes and the incremental input. The INDI attitude controller of a fixed-wing or quadcopter has the control block structure given by Figure 2.2. The linear controller is in this case a PD controller, the same filter has been applied to the angular rates and the input. The filtered signals are all delayed by the same time stamp and are denoted by the subscript f . Elaborating Figure 2.2 by defining H as the second order filter, A for the actuator dynamics and G for the actuator effectiveness Figure 2.3 is created. Smeur et al. [5] proved that the closed-loop transfer function TF between the virtual input v and the angular acceleration measurement $\dot{\omega}$ is given by Equation 2.8. The discrete time operator in the frequency domain is defined as z .

$$TF_{v \rightarrow \dot{\omega}}(z) = A(z) \quad (2.8)$$

The performance of the INDI controller in reference tracking depends solely on the actuator dynamics as given by Equation 2.8. The faster the actuators the better the performance of the system will be. Smeur et al. [5] proved this concept on a quadcopter with the Paparazzi open source autopilot. The obtained results showed that INDI and PID can be tuned to obtain the same reference tracking behavior when a step input is

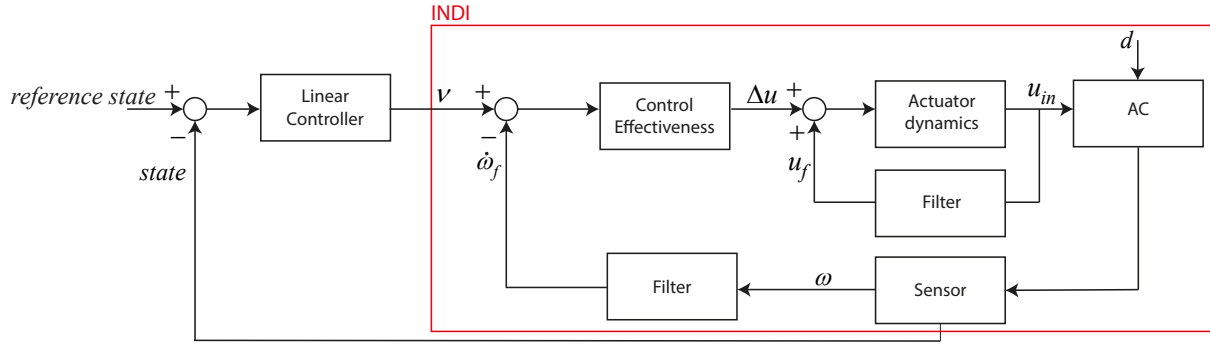


Figure 2.2: Schematic INDI control block structure

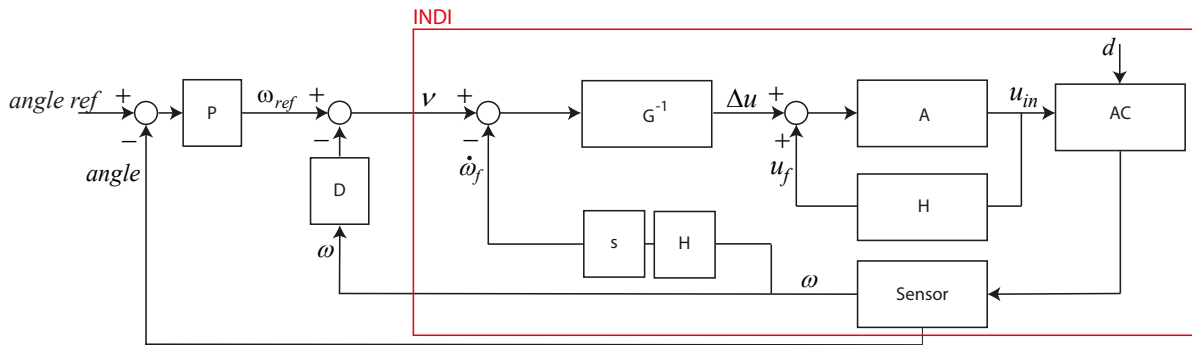


Figure 2.3: INDI control block structure

applied. Smeur et al. [5] derived the closed-loop transfer function between a disturbance d and the measured angular acceleration $\dot{\omega}$ given by Equation 2.9.

$$TF_{d \rightarrow \dot{\omega}}(z) = A(z)H(z)z^{-1} \quad (2.9)$$

The performance in disturbance rejection depends on the actuators, the filter and the sampling time. The more the signal needs to be filtered the more delay will be present in the system degrading the performance of the disturbance rejection. The highest sampling time does not only guarantee the principle of time scale separation but also improves the disturbance rejection characteristics.

The disturbance rejection characteristics of INDI were tested by Smeur et al. [5] by changing the center of gravity of the quadrotor. The INDI controller performed 5 times better than the PID controller in terms of reaction time [5]. It took the INDI controller 0.3s to bring the pitch angle back to the desired value whereas the PID controller took 1.5s for the same disturbance [5]. The results are shown in Figure 2.4 [6] for the INDI controller and in Figure 2.5 [6] for the PID controller. The INDI and PID were tuned such that they gave the same results for reference tracking. This once again shows that the PID controller cannot be tuned optimally for both scenarios.

Vlaar applied INDI to a fixed-wing MAV from the University of Minnesota during his master thesis at TU Delft [24]. INDI was used for the attitude control of the vehicle using estimators for the actuator position and a second order filter for the angular acceleration. The same filter was also applied to the input, as suggested by Smeur et al. [5]. A full aerodynamic model of this aircraft was also available which gave Vlaar [24] the opportunity to compare the performance of the INDI controller in a simulation environment with the actual test flights. The flight test results were as expected from the simulations apart from some small deviations due to the aircraft oscillations around the trim speed induced by a vibrating speed sensors [24]. INDI can not only be used for attitude control but also position control. Smeur et al. [6] derived and developed a relation between the MAV thrust and the linear accelerations. Outer loop INDI proved to be very successful in gust rejection as shown by the results given by Smeur et al. [6] by flying in and out of the flow of a fan. In terms of

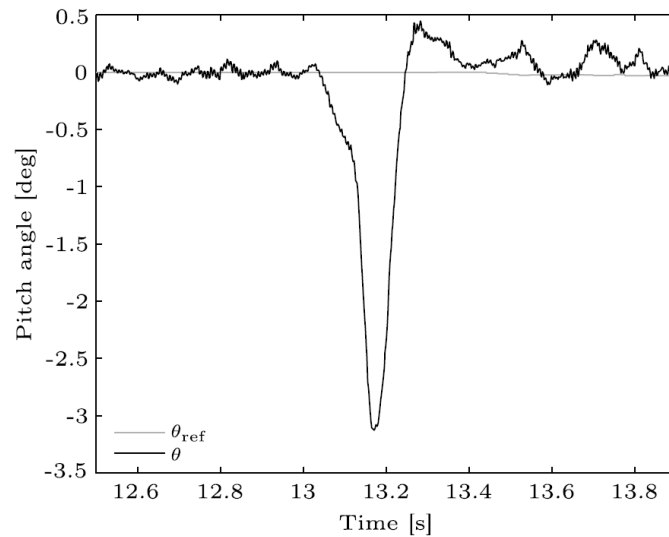


Figure 2.4: Pitch angle during the disturbance rejection for the INDI controller [6]

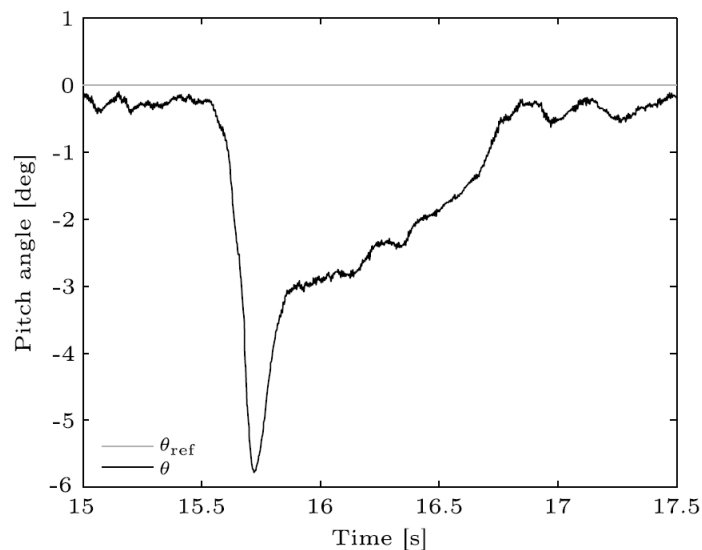


Figure 2.5: Pitch angle during the disturbance rejection for the PID controller [6]

average position error the INDI controller performed 3 times better compared to a PID controller tuned for the same tracking response [6]. The difference between the two flight paths is shown in Figure 2.6 [6].

2.1.4. AINDI

AINDI was developed to further increase the robustness of INDI to model inaccuracies and actuator damage or loss. As shown by Equation 2.7 INDI depends on the actuator effectiveness model G . The accuracy of the model is critical for both the stability and performance of the system response. Smeur et al. [5] performed flight tests on the Bebop quadcopter in which the actuator effectiveness was set either too low or too high. If the actuators are more effective than the model predicts, the required angular acceleration will not be reached as soon as expected requiring an additional input from the controller and thus requiring more time [5]. In this case oscillations occur, but they can be reduced by lowering the gains of the linear controller [5]. A more destructive scenario occurs when the effectiveness is estimated to be higher than the actual value. In this case fast oscillations occur which cannot be eliminated by the linear controller [5]. Increments in the control effectiveness are calculated based on the difference between the actual and expected angular acceleration [5]. The rate at which the control effectiveness changes can be selected, the faster it changes the more quickly the

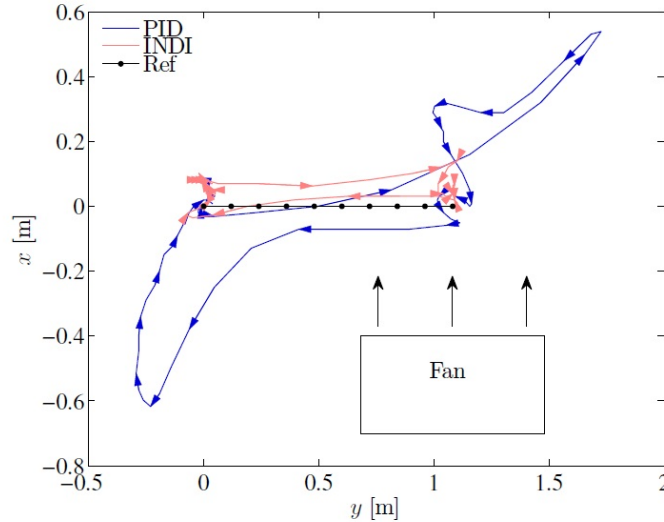


Figure 2.6: Comparison between PID and INDI position control when flying in and out of the fan [6]

performance of the system will improve, a limit however exists and if exceeded will lead to loss of convergence and therefore instability [5]. This control strategy is very interesting for fixed-wing MAVs as the effectiveness of the control surfaces is dependent on the flight speed. Furthermore the performance of servos used on MAVs degrades over time due to heat and friction. For the Slick 360 Micro fixed-wing MAV, Mohamed et al. [4] had to discard the servos after every flight tests to ensure the degradation was not influencing the controller performance.

2.2. TURBULENCE

MAVs fly close to the ground in a region called the Atmospheric Boundary Layer (ABL). This part of the atmosphere is the most affected by weather phenomena and therefore also by varying wind conditions. Wind engineers have documented the wind speeds at various locations on earth for a period of over 100 years [3]. These measurements give an indication of the average wind speeds that can be expected in a certain area at a certain height with the aim of understanding the effects on buildings and large structures. This information can be used to estimate if the MAV is able to fly against the wind but does not provide any information on the stability during the flight. The stability is influenced by the horizontal and vertical variation of wind speed within the wing span of the MAV, also known as turbulence. Research on atmospheric turbulence and the effects of turbulence on MAV flights was researched at RMIT by Watkins et al. [3]. The two main parameters used to characterize turbulence are the turbulence intensity (Ti) and the turbulence length scale (L). Turbulence intensity is defined as the fluctuating velocity component compared to the mean velocity \bar{V}_w . It can be calculated for each velocity component individually or for the entire velocity vector. The longitudinal turbulence intensity I_u is given by Equation 2.10 [3].

$$I_u = \sqrt{(u')^2 / \bar{V}_w}, \quad \text{with} \quad \bar{V}_w = \sqrt{u^2 + v^2 + w^2} \quad (2.10)$$

The ambient wind velocity is given by V_w . The components of V_w long the body axes are defined as u, v, w . The fluctuating velocity component in the longitudinal direction is defined as u' . When flying with a fixed wing MAV the mean velocity component becomes the wind velocity plus the aircraft airspeed V_{veh} . This implies that the faster the MAV is flying, the lower the turbulence intensity it will experience. The more general form of by Equation 2.10 which includes the vehicle speed is given by Equation 2.11 [3].

$$J_u = \sqrt{(u')^2 / \bar{V}_r}, \quad \text{with} \quad \bar{V}_r = \sqrt{(u + V_{veh})^2 + v^2 + w^2} \quad (2.11)$$

The turbulence intensity in urban environments can be up to 50% [4]. In cities the turbulence intensity increases drastically as the MAV flies closer to the ground due to the high buildings.

The turbulence length scale is characterized by the average length of the eddies within the flow [4]. The length scale is usually comparable to the size of the object generating the turbulence, therefore outdoors it

will be in the order of 15 meters [4]. When flying in a wind tunnel the length scale is much smaller in the order of 1 meter. The larger the wind tunnel test section the larger the length scales can be made. This implies that turbulence generated in wind tunnels has more energy in the high frequency components compared to outdoor turbulence [4]. The von Karman spectra models the power spectral density of the velocity components and is often used to compute the turbulence length scale L [25]. The longitudinal velocity spectrum $S_{\bar{u}\bar{u}}$ in terms of the frequency f in Hz and is given by Equation 2.12, the units are $(m/s)^2/Hz$ [25]. The standard deviation of the velocity component u is defined as σ .

$$S_{\bar{u}\bar{u}}(f) = \frac{4\sigma^2 L_x}{V} \frac{1}{\left(1 + 70.8 \left(\frac{L_x f}{V}\right)^2\right)^{5/6}} \quad (2.12)$$

For fixed-wing MAVs the most critical axes when subject to turbulence are roll and pitch [3]. Fixed-wing aircrafts have good stability around the yaw axis as the tail provides a large stabilizing moment in the direction of flight due to the long arm between the tail and the center of gravity [3]. The roll axis can be considered the most susceptible to disturbances as the gusts are three dimensional structures which create different lift distributions on the right and left wing inducing rolling motion [3]. For this reason Watkins et al. [3] performed tests to determine the variation in flow pitch angle along the wing span when flying through turbulence. The results show that the pitch angle can vary up to 15° within a spacing of $50mm$ making it very difficult to counteract as the wing span reduces [3].

2.2.1. WIND TUNNEL TURBULENCE

Turbulence in the wind tunnel can be generated by using passive methods such as static grids or rods, or active methods which add extra energy to the flow by means of moving or rotating components. The most challenging aspect of creating turbulence in a wind tunnel is the small length scale that is produced by the grids. When the smooth flow encounters the grids, vortices arise from the edges of the grids decaying as the flow moves downstream [25]. The turbulence intensity, the length scale and the rate of change of the turbulence intensity in the stream direction are all parameters that are influenced by the type of grids, the vertical and horizontal spacing and the grid size. Ravi [25] measured the turbulence intensity and integral length scale for various grid set-ups in the RMIT Industrial Wind Tunnel (IWT). By changing the location of the grids Ravi could change the turbulence intensity from 12.9% at 7.75m down the streamline when the grids were placed at the test section inlet, to 7.3% at 7.75m for grids at the contraction section inlet. The turbulence length scale was influence by using a tighter grid mesh with smaller rods. The aim of this work was to reproduce turbulence intensities and length scales which can be used to replicate the flight of MAVs. The setup with a 12.9% Ti was later used by Mohamed et al. [4] to develop phase-advanced sensors for turbulence rejection. This set-up used chip-board plates of 6mm thickness and a 300mm width [25]. The plates covered the entire wind tunnel length and height with 600mm spacing as shown in Figure 2.7 [25]. The turbulence intensity profile for this set-up is given in Figure 2.8 [25].



Figure 2.7: Turbulence grid set-up at test section inlet [25]

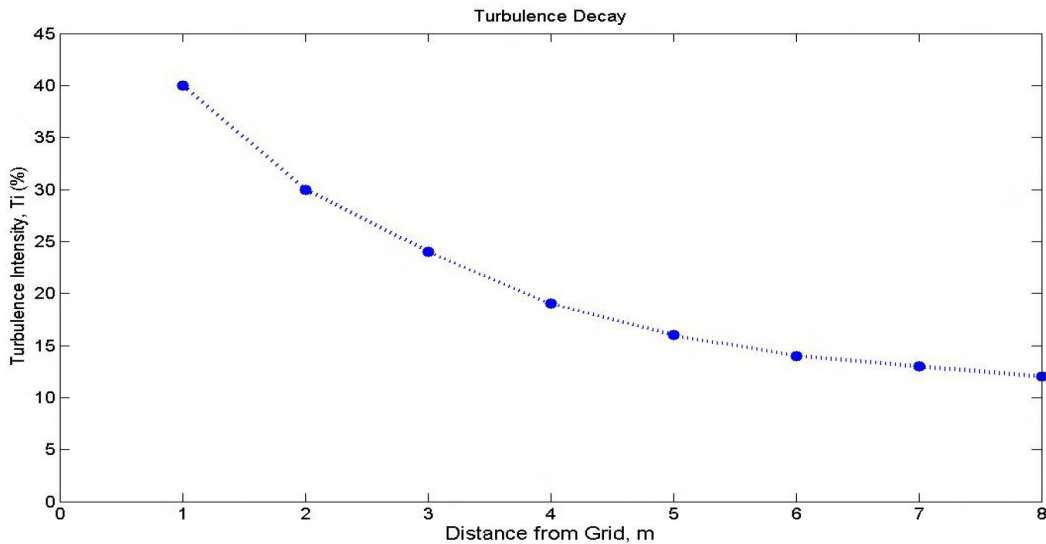


Figure 2.8: Turbulence Intensity variation downwards from grid set-up [25]

Then flying an MAV in free stream the turbulence intensity can however vary depending on the MAV flight speed as given by Equation 2.11 [3]. The turbulence intensity measured on-board of the vehicle by Mohamed et al. [4] in this set-up was equal to 13.2% with a length scale of 0.31m. The difference between the static turbulence and the turbulence measured on-board of the MAV can be visualized by plotting the power spectrum as shown in Figure 2.9 [4]. The spectrum is very similar to the von Karman model given by Equation 2.12 [25]. The non-stationary pitch probe shows a deviation in the power spectrum at the high frequency components due to the vibration of the wings and probe with the gusts thereby not being able to measure the gusts itself [4].

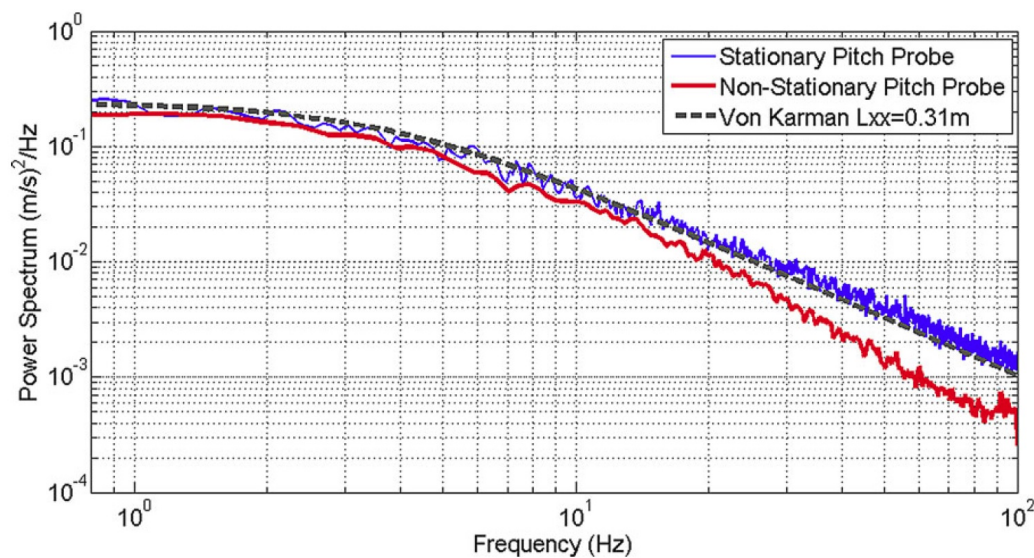


Figure 2.9: Power spectrum of the longitudinal turbulence in the RMIT wind tunnel at $Ti = 12.6\%$ [4]

2.2.2. MEASUREMENT SYSTEMS

To measure the turbulence intensity various sensors can be used. The Cobra Probe developed by Turbulent Flow Instruments (TFI) measures the incoming flow vector in three dimensions in real time. It has a frequency response of up to 2000Hz, the head consists a central hole and 3 holes placed at equal distances from each other on a chamfered edge as shown in Figure 2.10 [26]. The incoming flow angle can be measured up to $\pm 45^\circ$ in all three directions. The main advantage of this sensor is that it is easy to use as it comes completely

calibrated and can be used out of the box. The velocity measurements can directly be used to calculate the turbulence intensity in three directions. This instrument has been used by many research studies at RMIT to characterize the flow in the industrial wind tunnel prior to the experiments. The Cobra probe is one specific

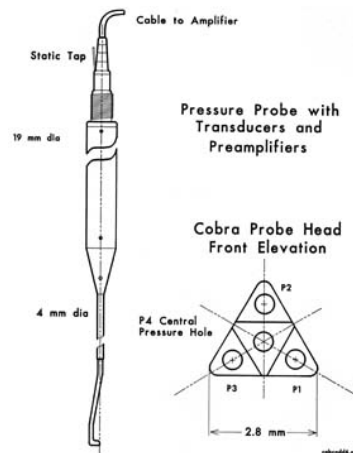


Figure 2.10: Cobra Probe Design [26]

type of multi-hole pressure probe. Other types of multi-hole pressure probes can also be calibrated to measure the flow velocity components. As explained by Rodi et al. [27] a 5-hole pressure probe can be used to measure the angle of attack, the side slip angle and the aircraft velocity. The calibration of a 5-hole pressure probe is explained in the following section. Hot wires are also often used to estimate the turbulence intensity in the wind tunnel. The wire is heated by a current passing through it, the heat dissipated to the environment changes depending on the velocity of the flow. The wire is most sensitive in the direction perpendicular to the flow. If the three dimensional velocity components have to be measured, three hot wire set-ups have to be used. The wires are more difficult to use compared to the Cobra Probes as they have to be calibrated. At TU Delft single axis hot wires are often used to characterize the flow in the wind tunnels.

2.3. PHASE-ADVANCED SENSORS

The high levels of turbulence are challenging for MAVs but are better tolerated by birds. This led to the investigation of how birds manage to fly in these conditions. Carruthers et al. [28] suggests that birds use their leading edge feathers to sense the flow and adjust the wings accordingly. This led Mohamed et al. [4] to develop a multi-hole pressure sensors capable of sensing the incoming flow angle and speed. Birds have leading edge feathers that sense the variation in flow pitch angle and speed [28]. This information is then used by the bird to morph the wings locally to counteract the effect of the gust. Based on the same principle, pressure based multi-hole probes were used to sense the velocity vector [4].

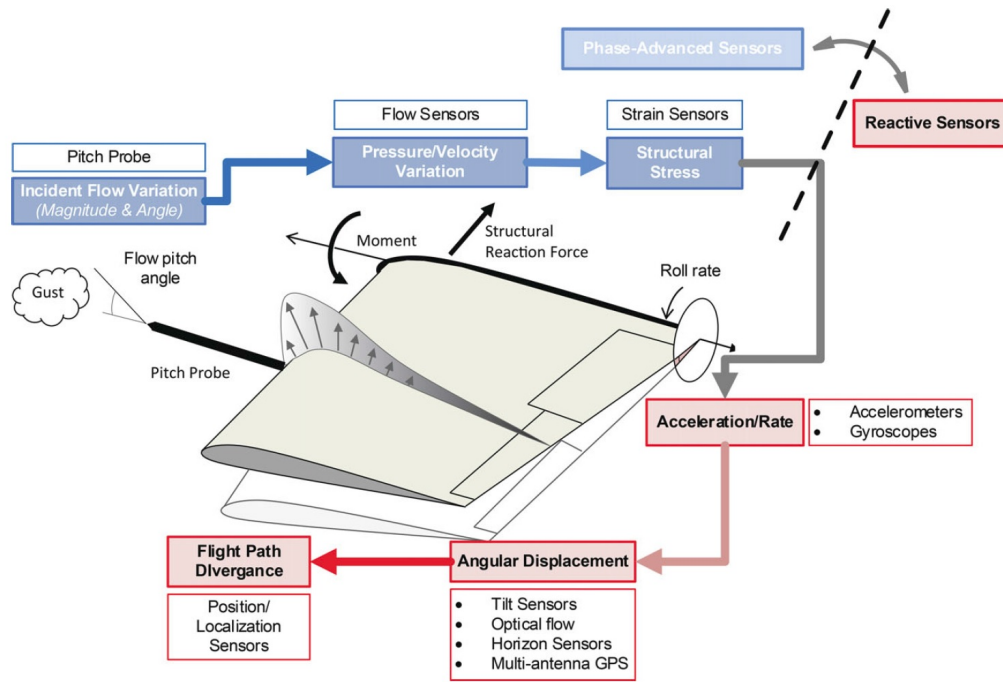


Figure 2.11: Timeline of turbulence effect on the MAV [4]

Variation in flow angle and velocity cause uneven pressure distribution over the two wings leading to differences in structural stress. These effects can be measured before any inertial response of the vehicle has occurred and can therefore be categorized as phase-advanced sensors. The changes in forces and moments cause the MAV to experience angular accelerations around the body axes. The accelerations lead in turn to angular rates and finally to angular displacements. Sensors which measure the inertial response of the vehicle to turbulence are classified as reactive sensors. An overview of the timeline is given in Figure 2.11 [4].

Mohamed et al. [29] investigated the correlation between the surface pressure variation and the resulting angular acceleration around the roll axis experienced by the MAV during turbulence. Pressure taps were placed at four locations along the wing span and two chord wise locations ($A=5.44\% x/c$ and $B=21.77\% x/c$). In Figure 2.12 [29] it can be seen that the correlation increases until 64.9% and decreases towards the tip. The decrease in correlation at the tips can be due to the tip vortices which affect the flow [29]. The correlation is above 0.6 at the 64.9% for tap location B and generally above 0.6 for location A. The decrease in correlation for high angle of attacks is due to flow separation and was visualized by Mohamed et al. [29] by performing wind tunnel tests. The results of these experiments showed Mohamed et al. [29] that it is possible to improve the attitude stability around the roll axis by measuring the surface pressure variations and by using the measurements for an attitude control system.

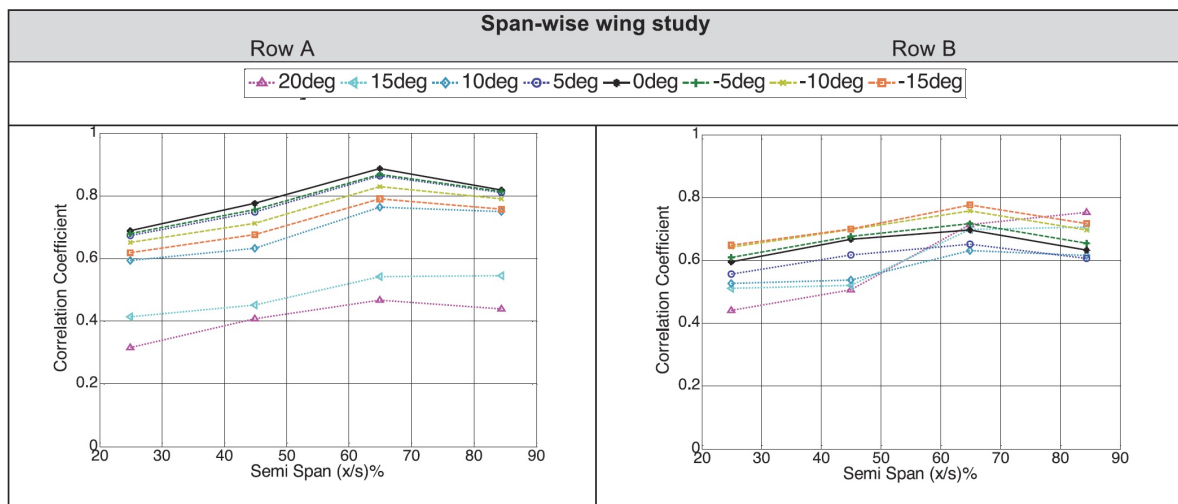


Figure 2.12: Correlation between surface pressure and angular acceleration around the roll axis for various location along the wind span [29]

The pitch probes developed by Mohamed et al. [4] measure differences in pressure when the incoming flow pitch angle and velocity change. The initial design of the probe consisted of a 3-hole probe with one central hole to measure the total pressure, 2 holes at the top and bottom chamfered at 45 degrees to measure the flow pitch angle and a static port. The probe design is shown in Figure 2.13 [4].

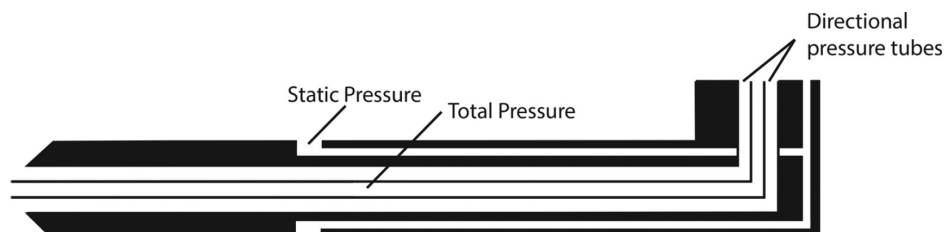


Figure 2.13: Probe design [4]

According to Mohamed et al. [30] the time lag of a controlled MAV at 10 m/s is 0.52 s . This would imply that the probes have to be placed 5.2 m ahead of the wing. The correlation between the disturbances measured by the probe and the disturbances experienced by the MAV decreases as the distance increases. A balance has therefore to be found between time advantage and correlation taking into consideration also the practical constraints associated with making probes which are of considerable length. A good compromise was found by Mohamed et al. [30] by placing the probes 15 cm ahead giving the controller 15 milliseconds time advantage. This time is still enough to improve the attitude stability as the turbulent length scales described earlier show that the same turbulence is usually experienced for a couple of meters at a time. The pitch probe were installed at the point of highest correlation given in Figure 2.13 [4]. These sensors were tested in combination with a PID controller as feed-forward commands for the ailerons separately [4]. The decoupling of the control surfaces enabled the MAV to compensate for the turbulence locally and to generate direct lift to counteract gusts around the pitch axis. The tests were performed in the RMIT Industrial wind tunnel, in the Monash wind tunnel and outdoors. To obtain a fair comparison of the system performance with and without the pressure probes time intervals of 300 seconds were compared, in total three test flights for each set up were performed [4]. To analyze the results the probability density function for the roll, pitch and yaw angles and rates is used. Tests were performed with a PID control architecture (CL1) and with the same architecture including the phase-advanced sensors (CL2). The probability density function for the roll angle during the outdoor flight is given in Figure 2.14 [4]. The effect of the probes is clearly visible as the curve for CL2 is more

centered around the desired roll angle making the peak value higher. The results for the wind tunnel tests are summarized in Table 2.1 [4]. The values are shown as percentages and represent the reduction in the range of the box plots for example the roll angle displacement was 28% less for CL2 compared to CL1 in the Monash wind tunnel.

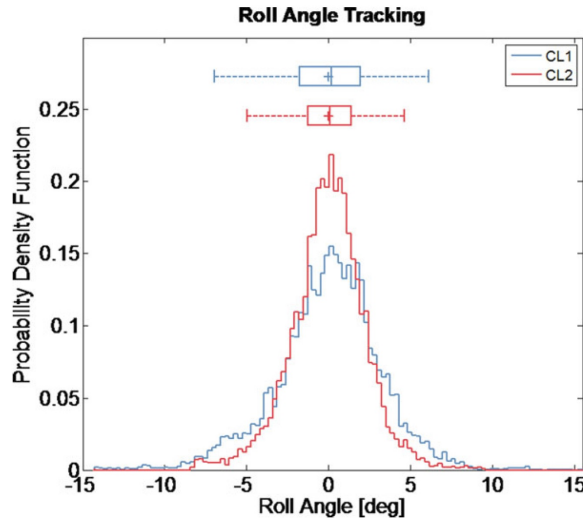


Figure 2.14: Probability Density Function of the roll angle for CL1 and CL2 [4]

Table 2.1: Reduction in box plot range obtained during wind tunnel testing at RMIT and Monash [4]

Variable	Displacement (CL1-CL2) [%]	
	Monash	RMIT
Roll angle	28	15
Roll rate	32	16
Pitch angle	41	31
Pitch rate	25	9
Yaw rate	12	16

2.3.1. 5 HOLE PRESSURE PROBE

A secondary design made by Mohamed et al. [4] consists of a 5-hole pressure probe, identical to the 3-hole pressure probe, but has two extra holes to the side which can be used to measure the variation in side slip angle. The differential pressure of a 5-hole probe can be related to the angle of attack, the side slip angle and the free stream velocity. By assuming the surface where the pressures are measured is spherical, mathematical relations can be derived based on the known pressure distribution on a sphere. The pressure coefficient is calculated based on Equation 2.13 [27].

$$C_p = \frac{P - P_\infty}{q} = 1 - f \sin^2 \phi \quad (2.13)$$

The pressure P is measured at an angle ϕ from the stagnation point and compared to the free stream pressure P_∞ . The result divided by the free stream dynamic pressure can be related to angle ϕ and a sensitivity factor f . The angle at which the pressure is measured ϕ can be rewritten in terms of direction cosines and can be applied to each pressure port individually. The centre hole is defined at an angle 0 deg and the remaining ports at 45 deg. The differential pressures are defined by Equation 2.14 [27].

$$\begin{aligned} \Delta P_1 &= P_1 - P_\infty = q \left(1 - \frac{(f-1)(\tan^2 \alpha + \tan^2 \beta)}{1 + \tan^2 \alpha + \tan^2 \beta} \right) \\ \Delta P_\alpha &= P_4 - P_5 = 2f q \frac{\tan \alpha}{1 + \tan^2 \alpha + \tan^2 \beta} \\ \Delta P_\beta &= P_2 - P_3 = 2f q \frac{\tan \beta}{1 + \tan^2 \alpha + \tan^2 \beta} \\ \Delta P_R &= P_1 - P_2 = f q \frac{(1 - 2 \tan \beta - \tan 2\beta)}{2(1 + \tan^2 \alpha + \tan^2 \beta)} \end{aligned} \quad (2.14)$$

The last three equations can be solved analytically for the angles α and β without knowledge of q and f [27].

$$\tan \beta = (\sqrt{2 * (\Delta P_{\beta}^2 + 2\Delta P_{\beta}\Delta P_R + 2\Delta P_R^2)} - \Delta P_{\beta} - 2\Delta P_R) / \Delta P_{\beta} \quad (2.15)$$

$$\tan \alpha = \tan \beta \frac{\Delta P_{\alpha}}{\Delta P_{\beta}}$$

The 5-hole probe can be calibrated in the wind tunnel by using these 4 relations: the differential pressures can be measured by differential pressure sensors, the autopilot board can be used to measure the angle of attack and the side slip angle. The wind tunnel speed q can be logged by the wind tunnel controller.

2.4. DISCUSSION AND CONCLUSION

Turbulence is one of the most challenging aspects for the flight of MAVs due to their small wing span and the low flight speeds at which they operate. During turbulence the incoming flow pitch angle can vary up to 15 degrees within a 50mm spacing. These variations lead to an uneven lift distribution over the wings resulting in roll and pitch angle accelerations. To ensure the MAV remains stable during the flight various turbulence mitigations systems have been developed. Two categories of turbulence mitigation systems can be used: phase-advanced and reactive. Phase-advanced techniques look at the incoming flow, the pressure distribution over the wings and the resulting changes in structural stress. These phenomena occur before any inertial response. Reactive techniques measure accelerations, rates and angles in the body frame which are the result of variations in flow and pressure over the wings.

The four control techniques reviewed in the previous section use reactive sensors to counteract the effects of turbulence on fixed-wing MAVs. The main advantages and disadvantages of each control technique can be summarized as follows. PID has already been implemented in the Paparazzi autopilot which will be used during the flight tests, and it requires no aerodynamic model or actuator model of the aircraft. On the other hand, a simple set of PID gains may not lead to the best performance in high turbulence intensities and therefore gain scheduling may be required for different flight speeds and angles of attack. The main disadvantage of PID is the trade-off between disturbance rejection and reference tracking mentioned by Smeur et al. [5]. The aim of this Master thesis is to improve the attitude control of the MAV in turbulence requiring both reference tracking of the desired attitude angle and disturbance rejection of wind gusts. This would imply that the PID controller would have to be tuned differently for each scenario depending on the priority of the task. This problem does not occur with nonlinear controllers. NDI gives excellent results in terms of tracking and disturbance rejection but requires a very accurate aerodynamic model of the MAV. Obtaining this model would require a series of wind tunnel tests which would deviate the focus of this Master thesis work. Less wind tunnel time is required for INDI, as this control technique is based on the control effectiveness and the actuators. This technique has given excellent results on quadcopters as shown by Smeur et al. [5] and fixed-wing MAVs as tested by Vlaar [24]. The INDI controller has been implemented in the Paparazzi autopilot for quadcopters but not yet for fixed-wing aircraft. One disadvantage of INDI is that its performance depends on the actuator model. If the actuator model changes during the flight, the results are affected. AINDI would solve this problem as it would calculate the model on-board during the flight.

For this Master Thesis project a number of practical considerations have to be taken into account before choosing the most appropriate control technique. At TU Delft the Open Jet Facility (OJF) is the only wind tunnel large enough to fly with fixed-wing MAVs. Due to the limited availability of the OJF, a couple of days are available at the start of the project and 1 week of wind tunnel time has been reserved half way through the planned thesis work. Due to the short time frame available for testing, an appropriate control strategy should be chosen at the start of the project. The most suitable attitude controller for this Master Thesis work is the INDI controller. This controller was chosen for the following reasons: it has been used for both quadcopter and fixed-wing attitude control with excellent results, it requires one set of wind tunnel tests to determine the control effectiveness, it is robust to changes in the aerodynamic model and center of gravity. The performance of INDI in turbulence applied to fixed-wing MAVs has not been analyzed before, providing an opportunity for this Master thesis to add to the body of knowledge. To be able to evaluate the performance of the INDI controller a traditional PID controller will be used as a comparative tool. The PID controller is a widely used and easy to implement making it a suitable baseline controller.

An other method to improve the disturbance rejection performance is to use phase-advanced sensors. The pitch probes developed by RMIT [4] proved to deliver excellent results in terms of roll and pitch angle stability. By placing the sensors 15cm ahead of each wing while flying at 10m/s a time advantage of 15 milliseconds is created. The knowledge about the gust direction and speed can be used by the control system to

move the aileron of each wing individually to neutralize the effect of the gust. This method is constrained by the actuator speed. The faster the actuators can move to the required aileron position the less impact the gust will have on the accelerations around the roll and pitch axis. These sensors act as a feed-forward components and can therefore be implemented on each control system. Following my internship at RMIT, a 5-hole probe was made available by RMIT to performed the test flights. The span-wise location and the length of the probe were researched at RMIT for the Slick 360 Micro fixed-wing MAV making this an platform for the experiments.

The experimental set-up is an important part of this Master Thesis work. The wind tunnel was booked to create various turbulence intensities in a controlled environment. The turbulence will be generated using grids placed at start of the test section. In the wind tunnel the turbulence intensity and the length scale can be determined by using sensors such as the cobra probes, hot wires or a calibrated five-hole probe. The Cobra Probe is the easiest and most straightforward method, due to a limited budget however the Cobra probe cannot be purchased for this master thesis project. The hot wire set up is not available during the wind tunnel time booked for this project and therefore the 5-hole probe will be calibrated such that it can be used to provide information on the flow properties. The turbulence generated has to be comparable to the turbulence intensity levels experienced in urban environments in the vicinity of high building. To create a fair comparison between the nonlinear INDI controller and the baseline PID controller the pilot will be taken out of the loop. The MAV is required to fly completely autonomously in the wind tunnel by using position control loops. No research was found on fixed-wing position control in the wind tunnel therefore any modifications with respect to standard position control techniques will be developed during this master thesis project. The main difference with respect to outdoor flights is that in the wind tunnel the MAV is hovering instead of flying forward with a constant speed. Position control with INDI has not yet been developed for fixed-wing MAVs. This would required additional wind tunnel time and intensive outdoor testing as well as the development of new control laws. In the time frame given for this master thesis project this would not be feasible. The PID control strategy will therefore be used for the position control loops as it does not depend on the MAV model.

2.5. RESEARCH QUESTION, AIMS AND OBJECTIVES

The state of the art research unveils that turbulence mitigation systems either rely on nonlinear control techniques or on phase-advanced sensors. These two methods have never before been combined. Furthermore turbulence rejection with an INDI controller for fixed-wing MAVs has never been tested in a controlled environment like a wind tunnel. Therefore the following research question was formulated:

What is the disturbance rejection performance of the INDI attitude controller with and without the phase-advance sensors in turbulence intensities comparable to those experienced in urban environments and how does the performance of the system compare to a traditional PID controller with and without phase-advanced sensors?

The research question can be divided into sub-questions:

SQ1 What are the differences in disturbance rejection performance between the INDI attitude controller with and without phase-advanced sensors in turbulent conditions?

SQ2 What are the differences in disturbance rejection performance between the INDI attitude controller and the PID attitude controller in turbulent conditions?

SQ3 What are the differences in reference tracking performance between the INDI attitude controller and the PID attitude controller?

SQ4 What is the performance of the position control loop in combination with the INDI attitude controller?

SQ5 What is the performance of the position control loop in combination with the PID attitude controller?

The goal of this master thesis is the following:

To gain a better understanding of turbulence mitigation systems for fixed-wing MAVs in turbulence intensities comparable to those experienced in urban environments by means of nonlinear control techniques in combination with phase-advanced sensors.

The main goal can be divided into multiple sub-goals:

SG1 Obtain actuator model and control effectiveness at cruise speed

SG2 Design experimental set-up

SG3 Obtain performance of the INDI attitude controller with and without phase-advanced sensors

SG4 Obtain performance of the PID attitude controller with and without phase-advanced sensors

SG5 Obtain performance of the PID position controller

3

MAV MODEL

The forces and moments experienced by the MAV during flight are described by the equations of motion. The Slick 360 Micro has a standard configuration with ailerons, an elevator and a rudder. The MAV can be considered a rigid body with constant mass and a plane of symmetry along the longitudinal axis. The thrust vector of the propeller lies in this plane of symmetry. The flight tests were performed in the OJF and outdoors within visual flight range therefore the equations of motion can be simplified by assuming the Earth is non-rotating, flat and with a constant gravity field. The equation of motion expressed in the body frame consist of three parts: the force equations, the moment equations and the kinematic relations [31]. The INDI controller uses the equations of rotational motion given by Equation 3.1 to predicted changes in the angular acceleration [31]. The Euler angles, defined by Equation 3.2, are used to relate the angular motions in the body frame to the inertial frame [31].

Rotational motion:

$$\begin{aligned} M_x &= I_{xx}\dot{p} + (I_{zz} - I_{yy})qr - I_{xz}(\dot{r} + pq) \\ M_y &= I_{yy}\dot{q} + (I_{xx} - I_{zz})rp - I_{xz}(p^2 - r^2) \\ M_z &= I_{zz}\dot{r} + (I_{yy} - I_{xx})pq - I_{xz}(\dot{p} + rq) \end{aligned} \quad (3.1)$$

Kinematic relations:

$$\begin{aligned} \dot{\phi} &= p + q \sin \phi \tan \theta + r \cos \phi \tan \theta \\ \dot{\theta} &= q \cos \phi - r \sin \phi \\ \dot{\psi} &= q \frac{\sin \phi}{\cos \theta} + r \frac{\cos \phi}{\cos \theta} \end{aligned} \quad (3.2)$$

Equation 3.1 can be rewritten in terms of the angular accelerations as Equation 3.3 [32].

$$\begin{aligned} \dot{p} &= (c_1 r + c_2 p)q + c_3 M_x + c_4 M_z \\ \dot{q} &= c_5 pr - c_6(p^2 - r^2) + c_7 M_y \\ \dot{r} &= (c_8 p - c_2 r)q + c_4 M_x + c_9 M_z \end{aligned} \quad (3.3)$$

The definitions of the multiplication parameters c_1 up to c_9 with $\Gamma = I_{xx}I_{zz} - I_{xz}^2$ [32]:

$$\begin{aligned} \Gamma c_1 &= (I_{yy} - I_{zz})I_{zz} - I_{xz}^2 & \Gamma c_2 &= (I_{xx} - I_{yy} + I_{zz})I_{xz} & \Gamma c_3 &= I_{zz} \\ \Gamma c_4 &= I_{xz} & c_5 &= (I_{zz} - I_{xx})I_{yy}^{-1} & c_6 &= I_{xz}I_{yy}^{-1} \\ c_7 &= I_{yy}^{-1} & c_8 &= (I_{xx} - I_{yy})I_{xx} - I_{xz}^2 & \Gamma c_9 &= I_{xx} \end{aligned}$$

The sum of moments around the body axes consists of an aerodynamic component M_a and a control component M_c . Around the roll axis this leads to Equation 3.4.

$$\dot{p} = (c_1 r + c_2 p)q + c_3 M_{x_a}(u, v, w, p, q, r) + c_3 M_{x_c}(V, \delta_a, \delta_e, \delta_r) + c_4 M_{z_a}(u, v, \dot{v}, w, p, q, r) + c_4 M_{z_c}(V, \delta_a, \delta_e, \delta_r) \quad (3.4)$$

In the body frame the components of the free stream velocity V are defined as u, v, w . The control surface deflections are denoted by $\delta_a, \delta_e, \delta_r$ for the ailerons, elevator and rudder respectively. Around the pitch axis dividing the moments into aerodynamic and control components leads to Equation 3.5.

$$\dot{q} = c_5 pr - c_6(p^2 - r^2) + c_7 M_{y_a}(u, v, w, \dot{w}, p, q, r) + c_7 M_{y_c}(V, \delta_a, \delta_e, \delta_r, \delta_t) \quad (3.5)$$

A second derivative term is incorporated for the vertical velocity component \dot{w} . The thrust of the propeller is defined as δ_r . It is important to notice that these equations are nonlinear, therefore making it an ideal test case for nonlinear control techniques. In the literature section it was shown that a PID controller relies on a linearized model which is different for each flight condition. This implies that to achieve the best PID performance a different set of gains has to be used for each linearization point. The INDI controller gains depend on the actuator dynamics which remain unchanged across the entire flight envelope, therefore a single set of gains provides the optimum performance for all flight conditions. The aim of this thesis is to compare PID and INDI in terms of disturbance rejection. As the PID gains vary for each flight condition, the comparison has to be made for each condition separately. The analysis of the aircraft disturbance rejection for the entire flight envelope of the Slick 360 Micro is outside the scope of this thesis, therefore a specific flight condition is considered. The condition of interest is cruise at 10m/s. The accuracy and the range in which the linear system approximates the nonlinear equations is called the validity region [31]. Gusts can be considered as disturbances from the initial condition, the higher the turbulence intensity the larger the deviations from the initial condition will become introducing nonlinear behaviour.

Small changes in the angular rates can be approximated by applying a Taylor series expansion around the cruise condition of 10m/s. To obtain a good linearization is it sufficient to take the value of the function at the point of interest and the first partial derivative terms. The general expression for a multi-variable function is given by Equation 3.6.

$$\mathbf{Y} = f(\mathbf{X}_0) + \frac{\partial f(\mathbf{X}_0)}{\partial x_1} \Delta x_1 + \dots + \frac{\partial f(\mathbf{X}_0)}{\partial x_n} \Delta x_n \quad (3.6)$$

In this chapter the Taylor series expansion for the roll and pitch axes will be analyzed to make a model of the angular accelerations. This model will be used to determine the control effectiveness G used in the INDI control loop structure.

3.1. ROLL AXIS

The asymmetric aircraft motions are the aperiodic roll, the dutch roll and spiral. For the INDI controller it is important to predict fast motions which have the largest influence on the angular accelerations and are measured before the other motions occur. The aperiodic roll is a highly damped fast motion. An increase in aileron deflection causes the angular acceleration and the angular rate to increase, the acceleration however damps out due to the damping effect of the wings which generate a moment in the opposite direction. After a short period of time a constant roll rate is achieved, each constant roll rate corresponds to a specific aileron deflection. During this maneuver the longitudinal flight speed is considered constant $\Delta u = 0$. The lateral speed and rudder input are neglected: $\Delta v = 0$ $\Delta r = 0$. The effects of the symmetric motions are neglected: $\Delta \delta_e = 0$ $\Delta w = 0$ $\Delta q = 0$. Applying a Taylor series expansion to Equation 3.4 with the above mentioned assumptions leads to Equation 3.7.

$$\dot{p} = \dot{p}_0 + \left. \frac{\partial c_3 M_{xa}}{\partial p} \right|_{p=p_0} (p - p_0) + \left. \frac{\partial c_3 M_{xc}}{\partial \delta_a} \right|_{\delta_a=\delta_{a0}} (\delta_a - \delta_{a0}) \quad (3.7)$$

The partial derivatives with respect to p and δ_a are defined as F_p and G_{δ_a} respectively, simplifying 3.7 to 3.8.

$$\Delta \dot{p} = F_p (p - p_0) + G_{\delta_a} (\delta_a - \delta_{a0}) \quad (3.8)$$

The INDI control theory is based on the principle of time scale separation [5], thereby simplifying Equation 3.8 even further by assuming the damping term $F_p(p - p_0)$ is close to zero due to the high sample rate (in these experiments 512Hz). The equation used in the INDI loop structure is given by Equation 3.9.

$$\Delta \dot{p} = G_{\delta_a} \Delta \delta_a \quad (3.9)$$

To find the values of F_p and G_{δ_a} three different tests were performed: roll rig experiments in OJF, a free flight experiment outdoors and a free flight experiment in OJF. In the following subsections the experiments will be explained and the results analyzed and compared. For each of these test the values of F_p and G_{δ_a} were found by using the linear least-squares fitting method. To evaluate the correctness of the fit the data was divided into a training set and a test set. 80% of the data was used for the training set and the remaining 20% for the test set used to evaluate the model. The distribution of the residual terms, the coefficient of determination R^2 and the Root Mean Square error (RMSE) will be used to assess the validity of the model. If the results for the test set are very different from the training set, it can be an indication of over fitting, errors in the model or a poor dataset.

3.1.1. ROLL RIG

This rig was constructed on purpose for the Slick 360 Micro for both the roll and pitch axis. In the roll rig configuration, the plane can only move around the roll axis as the motion around the other axis is constrained. This test set-up ensures the assumptions for the aperiodic roll are met as the yaw axis is constrained. The roll rate and the roll acceleration were measured by the autopilot on board of the Slick 360 Micro. The aileron deflections were measured by the servo potentiometer. The aim of the experiment is to find the parameters at the cruise condition of 10m/s to compare the INDI and the PID controller performance. The experiments were also done at 7m/s to check how the parameters change with airspeed. The speed of 7m/s was chosen as a comparison as this is the minimum speed at which the Slick 360 Micro is able to fly with the current weight and sensor configuration. As given by Equation 2.11, this is the speed at which the MAV will experience the highest turbulence intensity levels and is therefore interesting for future research on turbulence mitigation systems.

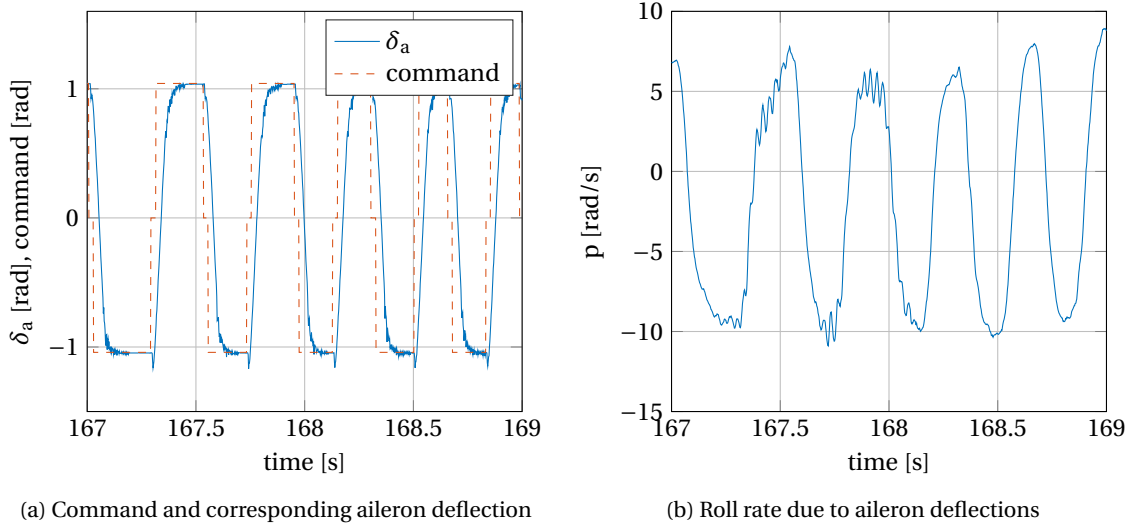


Figure 3.1: Aperiodic roll motion in the rig at 10m/s

In order to excite the system dynamics doublet inputs were given on the ailerons from $-\pi/3$ to $\pi/3$. No controller was used for this test as the natural response of the MAV had to be observed. The servo follows the command as a first order system with a constant slope as shown in Figure 3.1a. The corresponding angular rate is given in Figure 3.1b. The roll rate increases with a steep slope, at a certain moment however the effect of the damping term is clearly visible as the slope decreases and the roll rate levels out to a constant value. The roll rate shows high frequency oscillations for the first two doublets and the slope of the roll rate is slightly different for all inputs, this can be explained by the shift in the center of gravity with respect to the axis of rotation.

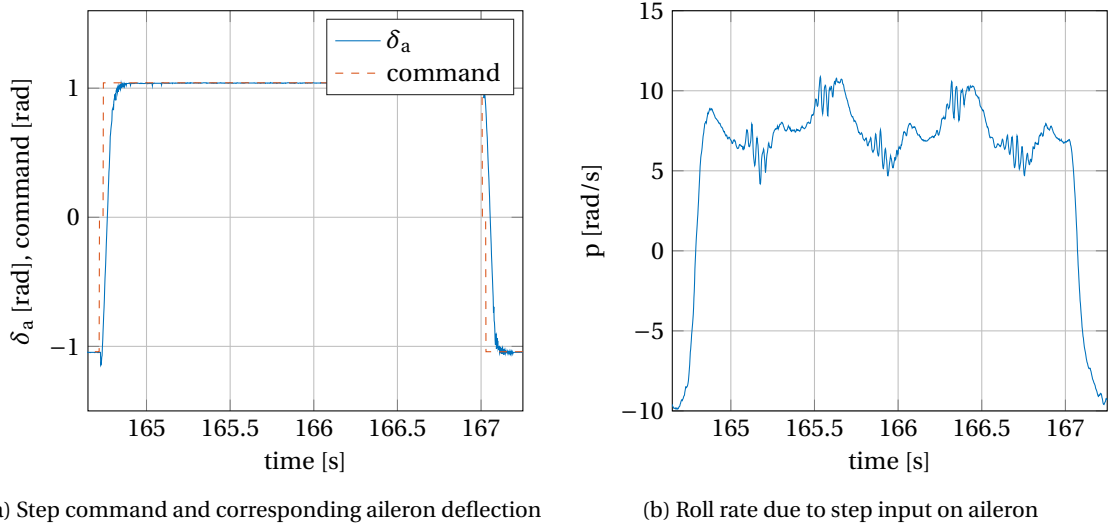


Figure 3.2: Influence of center of gravity shift with respect to axis of rotation on aperiodic roll motion in the rig at 10m/s

The centre of gravity was assumed to be in line with the thrust force of the propeller, the electronic component were however, all placed above the thrust line shifting the center of gravity towards the top of the fuselage. This caused uneven forces during the rotation in the rig as the gravity force gives an extra acceleration to the system when the wings are not level with the ground. To illustrate this error more clearly a set of full 360° rotations are displayed in Figure 3.2. The roll rate during there rotations should have a constant value as the aileron deflection is constant, the rate however increases when the MAV rotates towards the ground and decreases when it moves away from the ground illustrating the error in the center of gravity estimation.

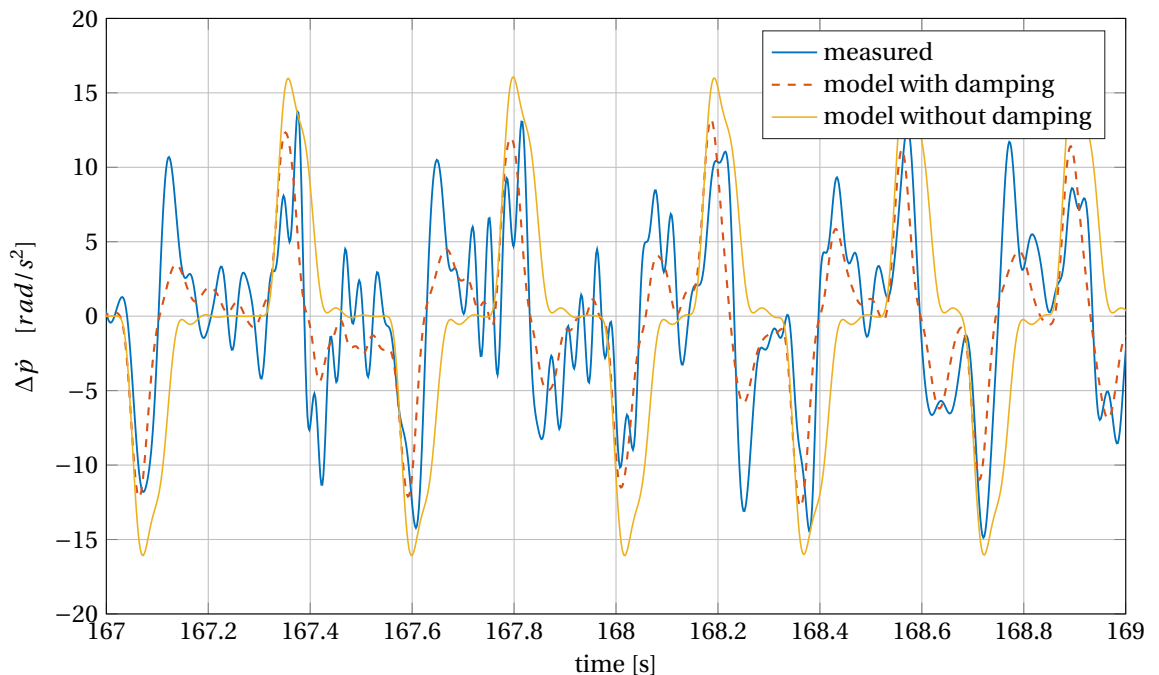


Figure 3.3: Measured and modeled angular acceleration around the roll axis at 10m/s during the roll rig set-up

In Figure 3.3 three curves are shown, the measured angular acceleration, the predicted angular acceleration based upon the model given by Equation 3.8 and the predicted angular acceleration used by the INDI control loop structure given by Equation 3.9.

Table 3.1: Linear fit parameters for the aperiodic roll rig model at 10m/s

Variable	Value	SE
F_p $\left[\frac{1}{s}\right]$	-26.2	0.4
G_{δ_a} $\left[\frac{\text{rad}}{s^2} \frac{1}{\text{rad}}\right]$	254	3

The parameters calculated by the linear model function *fitlm* in MatLAB are given in Table 3.1. For a period of 10 seconds the system was constantly excited using doublet inputs of varying time span but with the same amplitude of $\pm\pi/3$. In hindsight, the amplitude of the step input should have been chosen for a varying range of aileron deflections. The large aileron deflection used during this test are not often used by the controller and may excite nonlinearities in the system which lead to inaccuracies in the model parameters. The time span used for modeling is relatively short, but due to the repeatability of the input it was sufficient to determine a model of the system. The p-value for all parameters turned out to be very small ($\ll 5\%$), basically zero indicating the null-hypothesis can be rejected and therefore these variables are strongly correlated with the variable that they predict. The Standard Error (SE) of the coefficient shows the accuracy of the calculated parameter. The R^2 for the model given by Equation 3.8 is 0.6, indicating the model can be improved but the fit can be used for control purposes.

Table 3.2: RMSE of the model applied to the training set and test set during the roll rig set-up at 10m/s

Variable	Training set	Test set
RMSE	3.16	2.96

Table 3.3: RMSE of the model with and without damping for the roll rig set-up at 10m/s

Variable	With damping	Without damping
RMSE	3.16	5.62

To validate the model the parameters given in Table 3.1 are used to predict the angular acceleration for a different part of the dataset. The difference between the RMSE of the training set and the test set is given in Table 3.2, the difference is 6% indicating the model is valid in general and not only for the data set on which is fitted. The INDI control loop structure uses the model without the damping term given by Equation 3.9. If the damping term is neglected, the RMSE of the training set becomes 1.8 times higher as shown in Table 3.3. The model without damping can make an accurate prediction when variations in the input signal are observed. For constant input signals or zero inputs the behavior of the system is determined by the damping terms.

The same tests was executed at 7m/s. The results are shown in Table 3.4. The value of G_{δ_a} has drastically decreased for this speed. This implies that for lower airspeeds the ailerons have to deflect by larger amounts to achieve the same moment around the roll axis.

Table 3.4: Linear fit parameters for the aperiodic roll rig model at 7m/s

Variable	Value	SE
F_p	-26.1	0.8
G_{δ_a}	143	4

3.1.2. WIND TUNNEL FLIGHT

It is very interesting to compare the behavior of the aircraft in the roll rig with the response in free flight at 10m/s. During this test the wind tunnel speed was fixed to 10m/s while the MAV was flying in a fixed spot in the wind tunnel, thereby ensuring the airspeed experienced during the flight is identical to the airspeed encountered during the roll rig test. In free flight the MAV can rotate around all axis which can lead to couplings between the roll and yaw axis. In Equation 3.8 it was assumed that the aperiodic roll is not influenced by the yaw axis, therefore the results should be similar to the roll rig if the assumption is valid. The system was excited by the pilot by giving inputs while flying the aircraft in attitude mode with a PID controller. The inputs are therefore not perfect step inputs but represent a range of commands of varying amplitude and

frequency. To obtain a good frequency spectrum of the input a period of 150 seconds is used for the training data set and 40 seconds for the test set. The parameters for the model were found using a linear least squares fit in MatLAB.

Table 3.5: Linear fit parameters for the wind tunnel aperiodic roll model at 10m/s

Variable	Value	SE
F_p	-23.1	0.06
G_{δ_a}	270	0.4

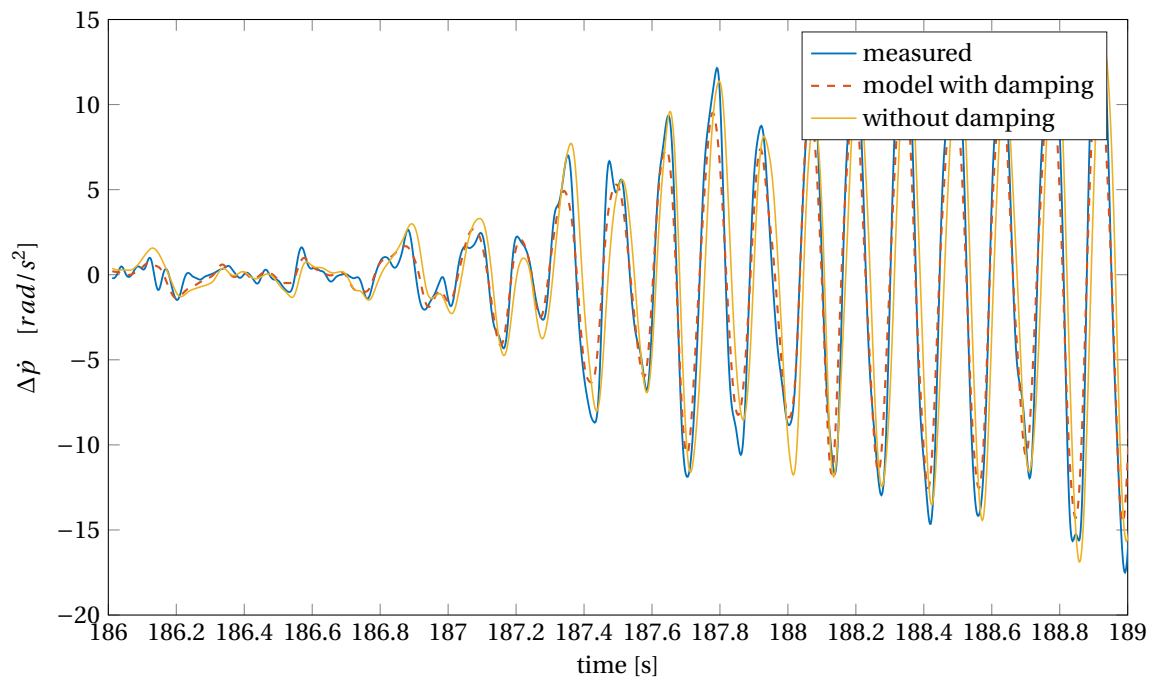


Figure 3.4: Measured and modeled angular acceleration around the roll axis at 10m/s during the free flight wind tunnel test

Table 3.6: *RMSE* of the model applied to the training set and test set during the free flight wind tunnel test at 10m/s

Variable	Training set	Test set
<i>RMSE</i>	1.09	1.06

Table 3.7: *RMSE* of the model with and without damping for the free flight wind tunnel test at 10m/s

Variable	With damping	Without damping
<i>RMSE</i>	1.09	2.01

The control effectiveness given in Table 3.5 is only 6% higher compared to the roll rig results. The *RMSE* for the test set is comparable to the training set as shown in Table 3.6. The model without the damping terms has an *RMSE* of 2.01 as shown in Table 3.7. In Figure 3.4 the prediction with and without the damping terms is similar. The difference between the two predictions is interpreted by the INDI controller as external disturbances.

3.1.3. OUTDOOR FLIGHT

During the outdoor flights the 5-hole pressure probes were connected to the static and total pressure ports to measure the airspeed. An airspeed controller was used to maintain the cruise speed at 10m/s. The system

was excited by the pilot by giving aileron inputs. The model parameters given in Table 3.8 are calculated based on the training set.

Table 3.8: Linear fit parameters for the outdoor aperiodic roll model at 10m/s

Variable	Value	SE
F_p	-16	1
G_{δ_a}	212	6

The difference in root mean square error between the test set and training is 2% indicating the model is not over-fitted. The angular acceleration is modeled with and without the damping. The root mean square error of the model without damping is 0.4% higher compared to the model with damping. The angular acceleration prediction is shown in Figure 3.5.

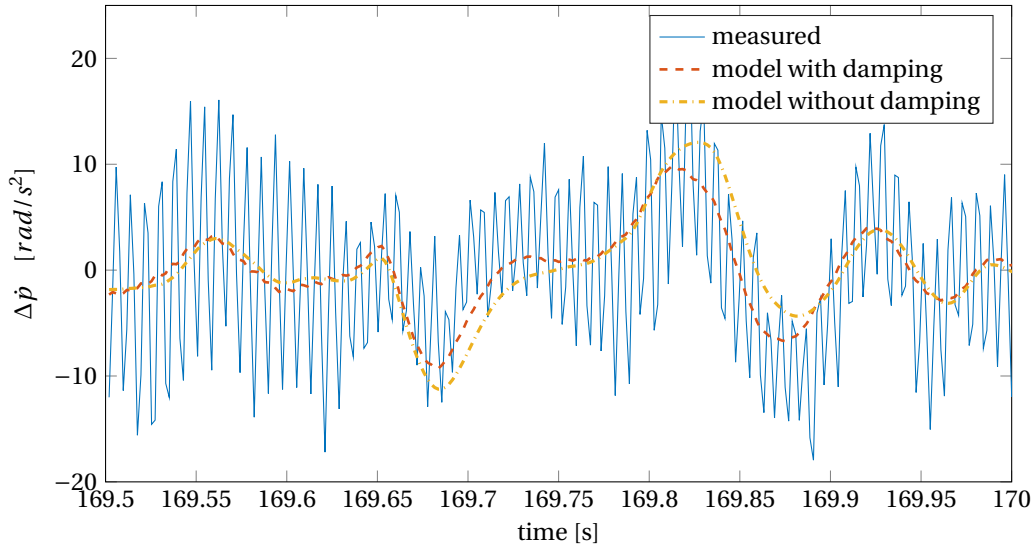


Figure 3.5: Measured and modeled angular acceleration around the roll axis at 10m/s during the outdoor flight

3.1.4. CONCLUSION AND RECOMMENDATIONS

The objective of this section was to model the angular acceleration around the roll axis and to determine the control effectiveness of the ailerons. To find the correct model three different tests were performed: roll rig measurements, free wind tunnel flights and outdoor flights.

When the MAV is placed in the roll rig it cannot get damaged making it an ideal test platform for new control techniques and to find model parameters. A few elements have to be considered however, which can influence the results during the roll rig set-up. The axis of rotation is subject to friction, which was minimized during the design but which can still lead to differences in the results. The rig construction forms an obstacle to the incoming flow leading to vortices which disturb the air around the MAV. The construction can be improved by making the wooden rods of cylindrical shape instead of rectangular shape. The MAV did not show any high frequency oscillations during the test and could remain fixed in one place when no controller was active indicating the turbulence generated by the rig had little effect on the behavior of the MAV. Any forces which occur in the lateral plane of the MAV will be compensated by the rig as the MAV has only 1 degree of freedom. The center of gravity of the MAV was assumed to lie in the thrust line of the propeller. During testing the center of gravity was found to lie more to the top of the fuselage due to the electronic components. This center of gravity offset causes errors in the roll rate and acceleration leading to errors in the estimation of the control effectiveness. During the roll rig tests doublet commands were given in an open loop manner therefore the response of the MAV was purely influenced by its own dynamics.

All the influences mentioned above lead to differences between the results calculated in the rig and those found during free flight. The largest source of error being the center of gravity shift as this was directly visible in the data. The *RMSE* calculated in free flight is much lower compared to the results obtained in the rig. This indicates the pilot inputs given in free flight excite all the relevant dynamics of the system making the

data better suited for the calculation of the parameters. The test procedure in the roll rig can therefore be improved to reduce the $RMSE$ value of the training and test set.

The difference between the results can be considered negligible for the purpose of this work making the roll rig set-up a good platform to calculate the effectiveness of a fixed-wing MAVs for various flight speeds. The calculation of the effectiveness was performed in an open loop configuration during the rig and with a PID attitude controller during free flight. The use of an attitude controller had no effect on the calculation of the control effectiveness as the results between the free flight and roll rig are very similar. This implies that test flights or rig experiments can be performed with active attitude controllers making the MAV easier to fly without influencing the results. The free flight tests shows that the influence of the yaw and pitch axis is negligible on the calculation of the aperiodic roll motion as the results are comparable to the roll rig where all other motions are constrained. Disturbances like wind gusts can influence the results during outdoor flights and may change the accuracy of the parameters.

A summary of the results is given in Table 3.9.

Table 3.9: Results for the damping and control effectiveness around the roll axis

Variable	Rig 10m/s	Free 10m/s	Rig 7m/s	Outdoor
l_p	-26.2	-23.1	-26.1	-16
G_{δ_a}	254	270	143	212

3.2. PITCH AXIS

The aircraft responses around the symmetrical axis are characterized by the short period mode and the phugoid. The phugoid is a slightly damped and slow motion which can be easily compensated by the controller by giving small elevator inputs. The short period mode is interesting for the INDI controller as this mode is fast and highly damped. During the short period the airspeed can be assumed to remain constant thereby the terms that depend on the speed u can be neglected. During this motion the thrust level is assumed constant $\Delta\delta_t = 0$. The asymmetric motions are considered negligible leading to $\Delta v = 0$ $\Delta p = 0$ $\Delta r = 0$ $\Delta\delta_a = 0$ $\Delta\delta_r = 0$. The second order derivative is neglected $\Delta\dot{w} = 0$. With these assumptions Equation 3.5 is simplified to Equation 3.10.

$$\dot{q} = \dot{q}_0 + \left. \frac{\partial c_7 M_{y_a}}{\partial w} \right|_{w=w_0} (w - w_0) + \left. \frac{\partial c_7 M_{y_a}}{\partial q} \right|_{q=q_0} (q - q_0) + \left. \frac{\partial c_7 M_{y_c}}{\partial \delta_e} \right|_{\delta_e=\delta_{e0}} (\delta_e - \delta_{e0}) \quad (3.10)$$

The damping terms are denoted by F_w and F_q and the control effectiveness is defined as G_{δ_e} leading to Equation 3.11.

$$\Delta\dot{q} = F_w V \Delta\alpha + F_q \Delta q + G_{\delta_e} \Delta\delta_e \quad \alpha = w/V \quad (3.11)$$

If the principle of time scale separation is applied, the angular acceleration is modeled by Equation 3.12.

$$\Delta\dot{q} = G_{\delta_e} \Delta\delta_e \quad (3.12)$$

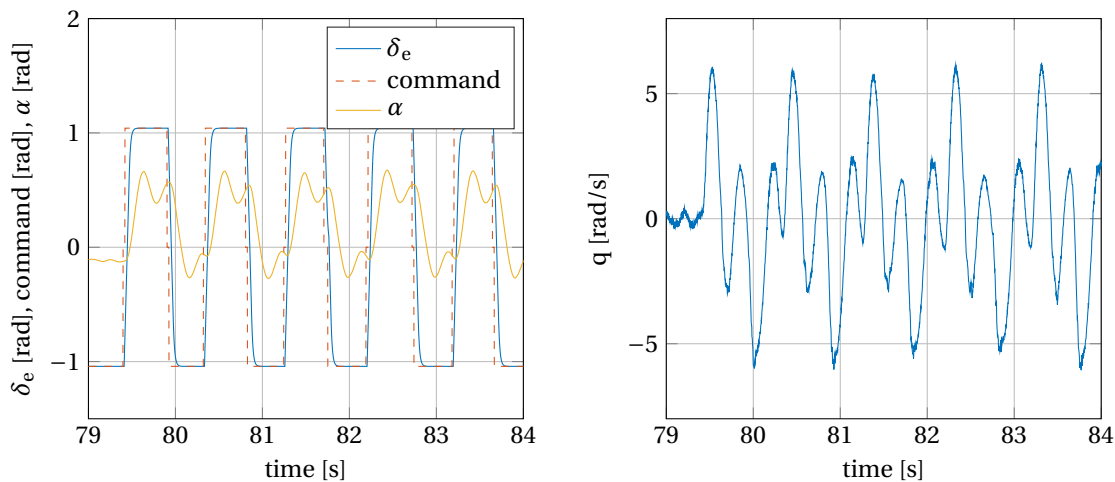
To find the values of F_w , F_q and G_{δ_e} three different tests were performed: pitch rig experiments in OJF, a free flight experiment outdoors and a free flight experiment in OJF. In the following subsections the experiments will be explained and the results analyzed and compared.

3.2.1. PITCH RIG

The pitch rig allows the MAV to rotate only around the pitch axis. This constrained motion leads to differences with respect to the free flight condition. During the free flight of an MAV, the pitch inputs result in a constant pitch rate while the forward speed of the MAV remains constant and the vertical speed increases in upwards or downwards direction. In the rig the upwards/downwards motion is constrained, therefore the angle of attack at which an equilibrium is reached will not be identical to the angle of attack in free stream flight. This should not affect the elevator effectiveness which is the main point of interest for the design of the INDI controller. The control effectiveness mainly depends on the shape and size of the elevator and the forward flight speed of the MAV. To verify this assumption the results will be compared with the free stream flight condition.

As the aircraft motion is constrained in vertical direction the pitch angle and the angle of attack are identical, and the pitch angle measured by the autopilot system will be used as angle of attack to create a fit according to Equation 3.12. In Figure 3.6b shows that the pitch rate initially increases but it quickly damps

out with an oscillation. This test was performed open loop, therefore the dynamics determine the motion of the MAV leading to long period oscillations. In Figure 3.6a shows that the elevator inputs cause the MAV to reach an equilibrium at a new angle of attack, although the oscillations around the equilibrium point have not damped out yet when the new input is given.



(a) Command and corresponding elevator deflection and angle of attack at 10m/s

(b) Pitch rate due to elevator deflections at 10m/s

Figure 3.6: Short period parameters

In Figure 3.7 the measured changes in angular acceleration around the pitch axis are compared to the models defined by Equation 3.11 and Equation 3.12. The angular acceleration can be very well predicted with the short period motion assumptions. The model with the aerodynamic damping terms as given by Equation 3.11 follows the measured angular acceleration with good accuracy. If the dynamics terms are left out and only the input is considered, the initial acceleration can be predicted, but the oscillations are clearly not modeled.

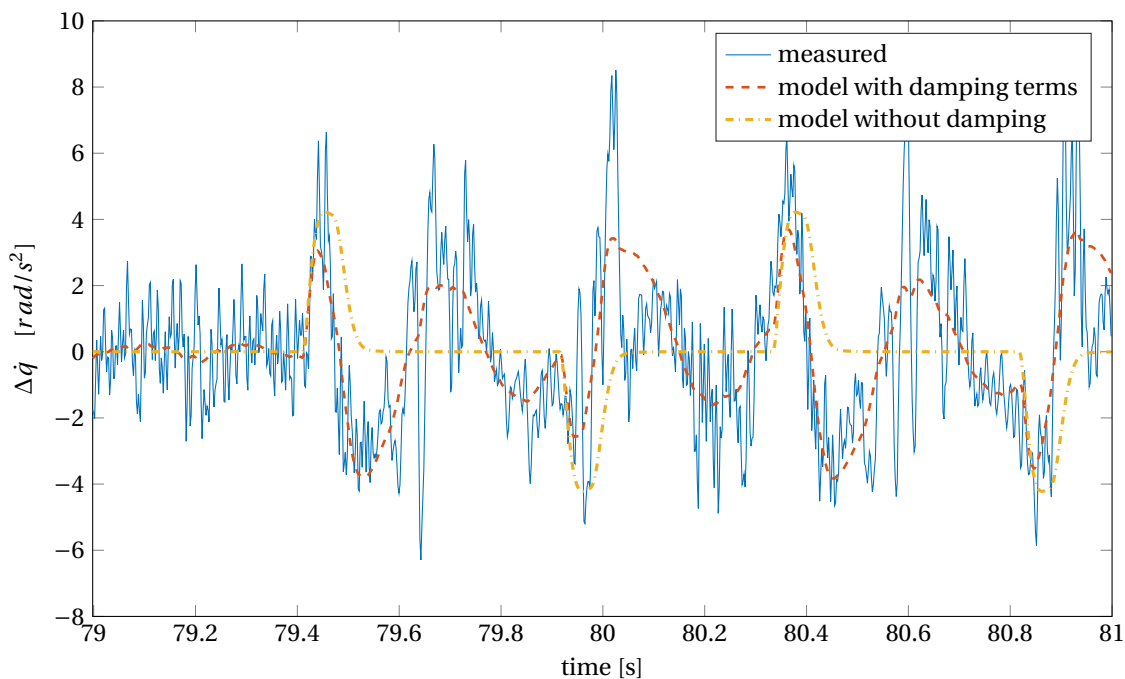


Figure 3.7: Measured and modeled angular acceleration in the pitch rig set-up at 10m/s

The data obtained at 10m/s was divided into a test set and a training set to evaluate the model. In total 45 seconds of data was considered, the training set consisted of 80% of the data and the remaining 20% was used for the test set. The training set was used to find the parameters given in Table 3.10. To verify the accuracy of the model and to ensure that over-fitting has not taken place the *RMSE* of the test set and training set are compared in Table 3.16. The difference between the values is 0.8%. Neglecting the damping terms leads to an increase in *RMSE* of 22% as shown in Table 3.17.

Table 3.10: Linear fit parameters for the short period motion in the pitch rig set-up at 10m/s

Variable	Value	SE
F_q	-8.3	0.2
F_w	-31.7	0.3
G_{δ_e}	73	1

Table 3.11: *RMSE* of the test set and training set for the pitch rig set-up at 10m/s

Variable	Training set	Test set
<i>RMSE</i>	1.25	1.24

Table 3.12: *RMSE* of the model with and without damping for the pitch rig set-up at 10m/s

Variable	With damping	Without damping
<i>RMSE</i>	1.25	1.61

Two additional tests were performed at 7m/s and 8m/s. Both test sets consisted of 45 seconds of data with doublet inputs of various lengths. The control effectiveness is for 7m/s is given in Table 3.13. The control effectiveness is for 8m/s is given in Table 3.14. The effectiveness values are very close to each other, indicating the control effectiveness has a nonlinear dependency with airspeed.

Table 3.13: Linear fit parameters for the short period motion in the pitch rig set-up at 7m/s

Variable	Value	SE
F_q	-5.6	0.1
F_w	-14.4	0.1
G_{δ_e}	34.8	0.2

Table 3.14: Linear fit parameters for the short period motion in the pitch rig set-up at 8m/s

Variable	Value	SE
F_q	-5.9	0.8
F_w	-18.0	0.1
G_{δ_e}	36.8	0.2

3.2.2. WIND TUNNEL FLIGHT

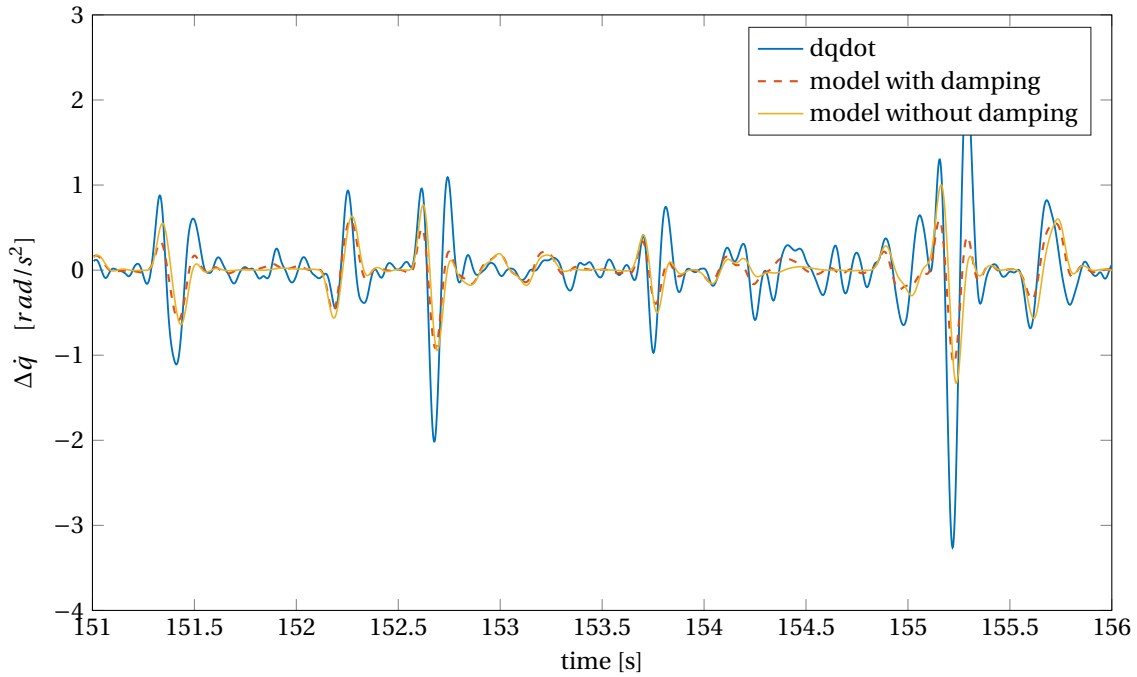


Figure 3.8: Measured and modeled angular acceleration around the pitch axis at 10m/s during the free flight in the wind tunnel

During the free flight in the wind tunnel the 5-hole pressure probes were not functioning properly as leaks were discovered after the test flight. The probe data can therefore not be used to model the angle of attack. The only angle which was measured during the pitch motion of the MAV is the pitch angle θ . Despite this assumption not being entirely correct, θ is used to obtain a model of the short period motion. All parameters in the model have a p-value below 5% indicating the parameters influence the response variable $\Delta\dot{q}$. The results for G_{δ_e} are 15% higher compared to the pitch rig results. The test was performed by manually flying in the wind tunnel with a PID attitude controller. The system was exited around the pitch axis by giving inputs to the elevator. The $RMSE$ of the test set is 6 times higher compared to training set as shown in Table 3.16. This error may be due to the use of the pitch angle to estimate the angle of attack value. Difference in $RMSE$ between the model with and without the damping is much smaller as shown in Table 3.17. Neglecting the damping term does not show visible differences in the prediction of the angular acceleration given in Figure 3.8.

Table 3.15: Linear fit parameters for the short period motion during free flight at 10m/s

Variable	Value	SE
F_q	-11.3	0.1
F_w	-11.7	0.1
G_{δ_e}	85.7	0.5

Table 3.16: Difference between test set and training $RMSE$ for the free wind tunnel flight around the pitch axis

Variable	Training set	Test set
$RMSE$	0.284	1.698

Table 3.17: Difference between the model with and without the damping in terms of $RMSE$ for the free wind tunnel flight around the pitch axis

Variable	With damping	Without damping
$RMSE$	0.284	0.329

3.2.3. OUTDOOR FLIGHT

The airspeed, measured by the probes, was kept constant at 10m/s by using an airspeed controller. The system was exited by the pilot by giving elevator inputs. The pitch angle is used to calculate the model instead of the angle of attack. The angle of attack measurement could not be retrieved from the data as the probe was not connected to all 5 holes during the test. The model parameters given in Table 3.18 are calculated based on the training set containing 100 seconds of data. The difference between the model including the damping terms and without the damping terms is shown in Figure 3.9. The model predicts much smaller changes in acceleration compared to the measured values. The model can be largely improved by using the angle of attack value instead of the pitch angle.

Table 3.18: Linear fit parameters for the outdoor aperiodic roll model at 10m/s

Variable	Value	SE
F_q	-14	1
F_w	-52	3
G_{δ_e}	59	3

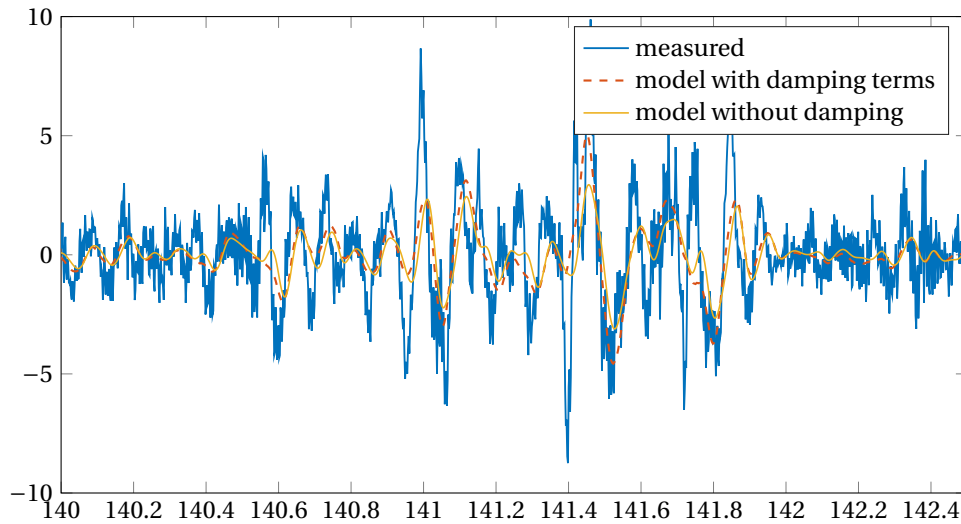


Figure 3.9: Measured and modeled angular acceleration around the pitch axis at 10m/s during the outdoor flight

3.2.4. CONCLUSION AND RECOMMENDATIONS

The most reliable model of the short period motion is the model calculated using the rig results. This model includes the angle of attack which is a key parameter in the short period response. The models calculated based on the wind tunnel flight and the outdoor flight include the pitch angle leading to errors in the results. The rig model will therefore be used for the final controller design. Errors can still be present in the rig parameters due to the rig friction and the turbulence generated by the grids. Furthermore the rig results were obtained without the pressure probes installed in the wing making the moment of inertia around the pitch axis smaller.

Three test cases were performed with the results given in Table 3.19.

Table 3.19: Results from wind tunnel and outdoor tests

Variable	WT Rig	WT free	Outdoor
F_q	-8.39	-11.3	-14
F_w	-31.1	-11.7	-52
G_{δ_e}	72.2	85.7	59

3.3. YAW AXIS COUPLING

Equation 3.3 shows that for fixed-wing aircraft the yaw axis and the roll axis are coupled. It is interesting to investigate the influence of the rudder inputs and yaw rate on the aperiodic roll maneuver. By including the yaw rate and rudder input the Taylor series expansion of Equation 3.4 leads to Equation 3.13.

$$\Delta \dot{p} = F_p \Delta p + G_{\delta_a} \Delta \delta_a + F_r \Delta r + G_{\delta_r} \Delta \delta_r \quad (3.13)$$

The aperiodic roll model is calculated based on the free wind tunnel flight analyzed in subsection 3.1.2. The same 150 seconds of data are used to calculate the complete model shown in Table 3.20. The rudder effectiveness has a large standard error indicating this value is not accurate. During the flight the rudder was not often used by the pilot. To improve the estimation of G_{δ_r} , another flight should be performed were the system is exited more around the yaw axis. The aileron effectiveness and the roll damping are very similar to the values calculated in Table 3.5. This shows that the aileron effectiveness can be calculated by using a simplified model which does not include the yaw rate and rudder inputs.

Table 3.20: Rudder and yaw rate influence on aperiodic roll during free flight wind tunnel at 10 m/s

Variable	Value	SE
F_p	-21.5	0.06
G_{δ_a}	269	0.4
F_r	28	0.4
G_{δ_r}	210	32

3.4. ACTUATORS

The actuator model is perhaps the most important model for the INDI control architecture. As shown in the literature section, the actuator model determines the gains of the linear controller and the performance of the overall system. Errors in the actuator model can therefore make the system unstable or degrade its performance. The Slick 360 Micro uses 4 micro servos to move the control surfaces. The fastest servos available on the market were selected, namely the HK5330. They weigh only 1,9 grams and can move from 0 to 60 deg in 0.04 seconds.

The servo model can be determined by looking at the input of the system which is the PWM command from the autopilot and the output which is the position of the servo arm. The arm position is measured by the potentiometer, an electrical component which is used by the internal control system of the servo. The potentiometer values together with the PWM commands were logged at 512Hz by the Paparazzi autopilot system. When subject to a step input the servo behaves as a first order system with a constant slope and an initial delay as shown in Figure 3.10.

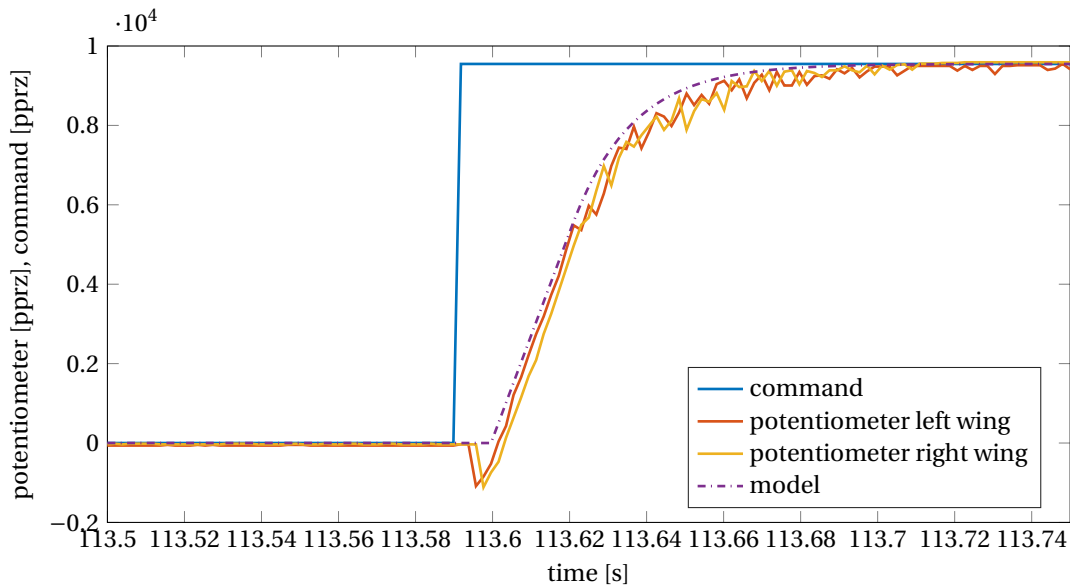


Figure 3.10: Potentiometer reading compared to servo model

In the Open-Source Paparazzi Autopilot system the PWM command is given in the range $[-9600;9600]$ called *pprz* units. The position of the servo arm δ_a is calculated by Equation 3.14 in *pprz* units. The initial delay of 10 milliseconds is mainly caused by the servo electronics. The servo has an internal controller which regulates the position based on the PWM command received by the autopilot system. If the internal servo frequency would be 512Hz, the delay would be approximately 2 milliseconds, this delay is however on average around 10 milliseconds indicating a lower internal control frequency. The slope of this servo is very steep and the fastest among its category with an increase of 500 *pprz* units each sampling time. The last part of the response resembles a first order system. The aileron deflection has to be measured in radians according to Equations 3.8 and 3.9. To convert the *pprz*-commands to radians Equation 3.14 can be used. The servo rotations range from $[-\pi/3;\pi/3]$.

$$\delta_a[rad] = \delta_{a_{min}} + \frac{(\delta_{a_{max}} - \delta_{a_{min}})}{19200} (\delta_a[pprz] + 9600) \quad (3.14)$$

The servo model in radians is given by Equation 3.15.

$$\begin{aligned} A(s) &= \frac{60}{s+60} \\ \left(\frac{\Delta\delta_a}{\Delta t} G_{\delta_a} \right)_{max} &= 11 \quad [rad/s] \\ \left(\frac{\Delta\delta_e}{\Delta t} G_{\delta_e} \right)_{max} &= 4 \quad [rad/s] \end{aligned} \quad (3.15)$$

To decrease the initial delay the Paparazzi Autopilot can be used as a servo controller. The autopilot can send pulses directly to the servo motors by using the PWM pins and it can read the potentiometer values through the ADC ports. The servo can be tuned to achieve the same slope as the original servo controller with a smaller initial delay. If the delay is reduced to 2 milliseconds the overall servo performance will drop to 0.032 seconds from 0 to 60 deg. The pitch probes used to improve the turbulence mitigation properties need a 15 milliseconds time advantage to move the ailerons to the desired position. If the servo is faster, it can reach larger deflections within these 15 milliseconds improving the turbulence rejection capabilities of the MAV. The INDI control loop structure also depends on the speed of the servos and will therefore improve in terms of reference tracking performance and disturbance rejection performance.

In Equation 3.14 it was assumed that the servo arm deflection is equal to the control surface deflection. From the drawing given in Figure 3.11 it can be seen that this assumption is correct if the servo arm length is equal to the radius which makes the control surface rotate. In this case $R1 \approx R2$ making the error negligible.

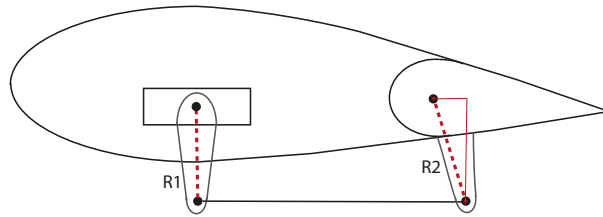


Figure 3.11: Servo mechanism drawing

3.5. PHASE-ADVANCED SENSORS

The phased-advanced sensors can be calibrated by using the formulas for a five hole spherical probe as explained in the literature section 2.3.1. The data were obtained for the range of flight speeds of interest (7m/s-12m/s) and for the range of angles of attack and side slip that can be typically experienced during the flight (+/-15 degrees).

Equation 2.14 used in the literature section will be used as a reference to calculate the angle of attack, side slip angle and dynamic pressure. The reference differential pressure was measured between the top and

central hole, therefore the equations used for the calibration change to the Equations given by 3.16.

$$\begin{aligned}
 \Delta P_1 &= P_1 - P_\infty = q \left(1 - \frac{(f-1)(\tan^2 \alpha + \tan^2 \beta)}{1 + \tan^2 \alpha + \tan^2 \beta} \right) \\
 \Delta P_\alpha &= P_2 - P_3 = 2f q \frac{\tan \alpha}{1 + \tan^2 \alpha + \tan^2 \beta} \\
 \Delta P_\beta &= P_4 - P_5 = 2f q \frac{\tan \beta}{1 + \tan^2 \alpha + \tan^2 \beta} \\
 \Delta P_R &= P_1 - P_2 = f q \frac{(1 - 2 \tan \alpha - \tan^2 \alpha)}{2(1 + \tan^2 \alpha + \tan^2 \beta)}
 \end{aligned}
 \tag{3.16}$$

The four differential pressures were measured on board of the autopilot system by using the analog ports and logged at a frequency of 512Hz. The real angle of attack was measured based on the pitch angle of the autopilot placed in line with the pressure probe. Some runs were executed with the autopilot measuring the angle of attack and other runs were executed while measuring the side slip angle. The angles could not both be logged at the same time as the yaw angle measurements are not reliable indoors. The probe was therefore rotated 90deg when the side slip angle had to be measured. The real dynamic pressure was measured by the Memcor Model 2101 digital pressure gauge at 10Hz. This instrument has a range from -1200 to 15000 Pascal. The method used to calibrate the sensor in the wind tunnel is explained in the following steps. The first and most straightforward test is to find the scaling and offset for ΔP_1 given the real value of q . When α and β are equal to zero first line of 3.16 reduces to Equation 3.17. To ensure the values of α and β are equal to zero the values of ΔP_α and ΔP_β should remain zero when the ΔP_1 changes.

$$\begin{aligned}
 \alpha &= \beta = 0 \\
 \Delta P_1 a_{p_1} + b_{p_1} &= q
 \end{aligned}
 \tag{3.17}$$

A least squares linear fitting method was used to determine the parameter coefficients. A summary of the coefficient values is given in Table 3.21. Runs 1 and 2 are performed on the same day and runs 3 and 4 on the following day. In Figure 3.12 the calibrated value of the ΔP_1 is compared to the real value of q .

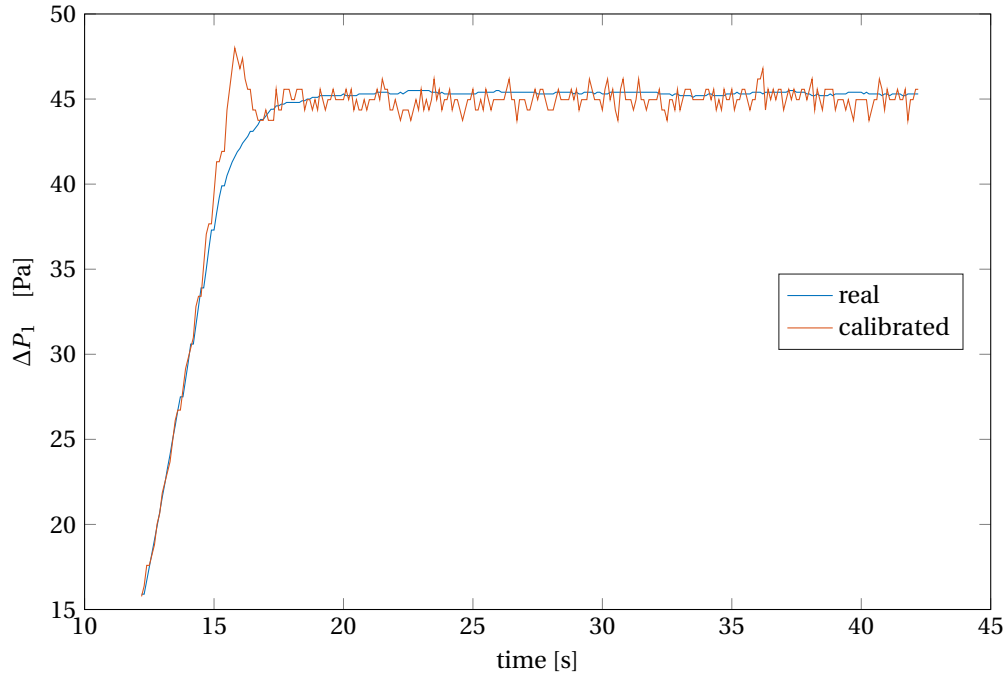


Figure 3.12: Calibration of ΔP_1 with α and β equal to zero

Table 3.21: Calibration parameters for ΔP_1

run	a_{P_1}	SE_a	b_{P_1}	SE_b	R^2
run 1	0.996	0.003	-0.018	0.142	0.995
run 2	1.122	0.002	1.093	0.125	0.998
run 3	1.176	0.002	-0.248	0.147	0.998
run 4	1.148	0.004	-0.435	0.219	0.996

If α is changed over the course of the test the equation for ΔP_1 becomes dependent of the sensitivity factor f . Given the values for α and q , the sensitivity factor can be determined:

$$\beta = 0 \tag{3.18}$$

$$\Delta P_1 a_{P_1} + b_{P_1} = q \left(1 - \frac{(f-1) \tan^2 \alpha}{1 + \tan^2 \alpha} \right)$$

A summary of the f values is given in Table 3.22.

Table 3.22: Sensitivity factor f

run	f	SE_f	R^2
run 1	0.608	0.014	0.607
run 2	0.434	0.019	0.273
run 3	0.808	0.022	0.489
run 4	0.957	0.025	0.539

Find the scaling and offset for ΔP_R given the real value of q and the sensitivity factor f :

$$\alpha = \beta = 0 \tag{3.19}$$

$$\Delta P_R a_{P_R} + b_{P_R} = \frac{fq}{2}$$

In Figure 3.13 the calibrated value of the ΔP_R is compared to the real value calculated using Equation 3.19 with the real values of q and α .

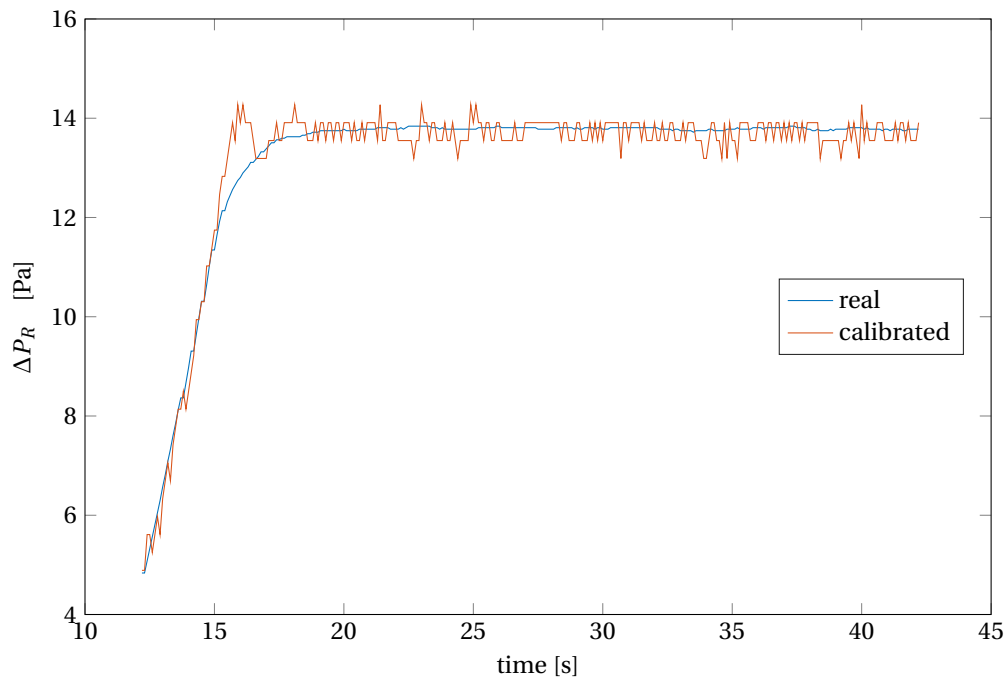
Figure 3.13: Calibration of ΔP_R with α and β equal to zero

Table 3.23: Calibration parameters for ΔP_R

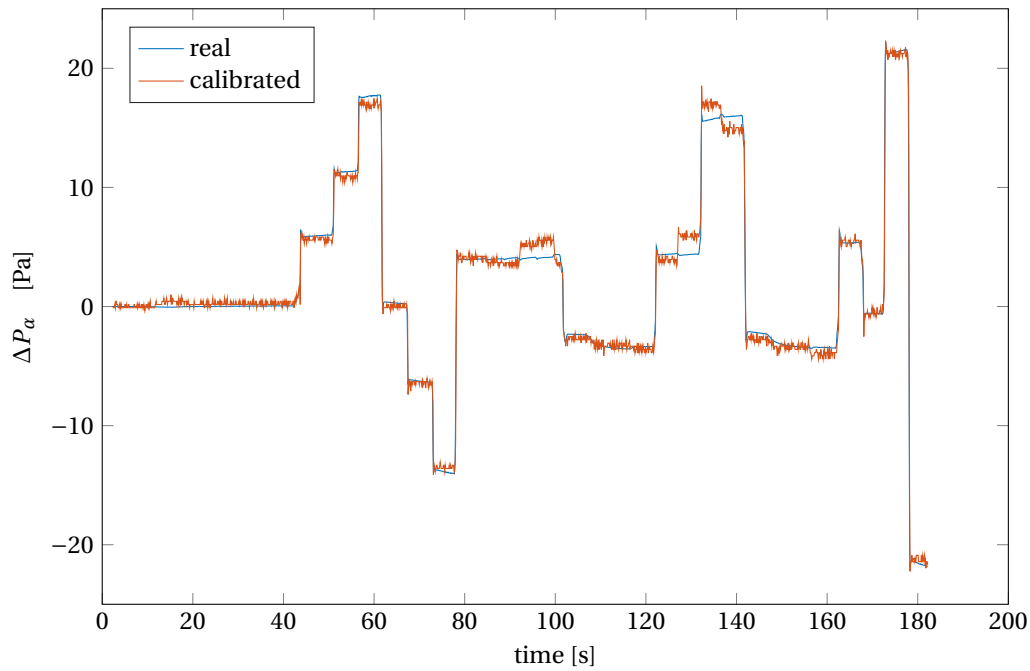
run	a_{P_R}	SE_a	b_{P_R}	SE_b	R^2
run 1	0.591	0.002	0.184	0.046	0.995
run 2	0.406	0.001	0.293	0.035	0.998
run 3	0.974	0.003	2.704	0.076	0.996
run 4	1.136	0.004	2.189	0.104	0.996

Find the scaling and offset for ΔP_α given the real value of q and the sensitivity factor f :

$$\beta = 0 \quad (3.20)$$

$$\Delta P_\alpha a_{P_\alpha} + b_{P_\alpha} = 2f q \frac{\tan \alpha}{1 + \tan^2 \alpha}$$

In Figure 3.14 the calibrated value of the ΔP_α is compared to the real value calculated using Equation 3.20 with the real values of q and α .

Figure 3.14: Calibration of ΔP_α assuming β equal to zero

Find the scaling and offset for ΔP_β given the real value of q and the sensitivity factor f :

$$\beta = 0 \quad (3.21)$$

$$\Delta P_\beta a_{P_\beta} + b_{P_\beta} = 2f q \frac{\tan \beta}{1 + \tan^2 \beta}$$

In Figure 3.15 the calibrated value of the ΔP_β is compared to the real value calculated using Equation 3.21 with the real values of q and β .

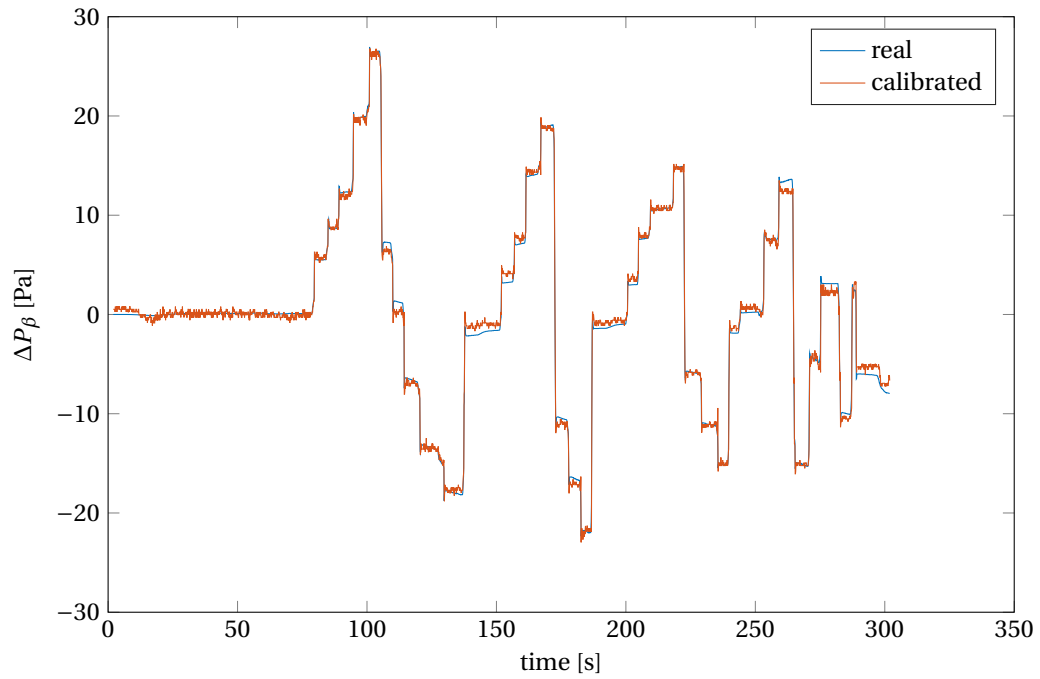


Figure 3.15: Calibration of ΔP_β assuming α equal to zero

An additional fit needs to be found for ΔP_R as the equation does not fit the measured curve. The error can be considered related to the shape of the probe head, which is not spherical but chamfered at 45 deg. The parameters multiplying $\tan \alpha$ need to be recalculated for this specific scenario:

$$\beta = 0$$

$$\Delta P_R a_{P_R} + b_{P_R} = f q \frac{(1-f_1 \tan \alpha - f_2 \tan^2 \alpha)}{2(1+\tan^2 \alpha)} \quad (3.22)$$

In Figure 3.16 the calibrated value of the ΔP_R for varying α is compared to the model given by Equation 3.22.

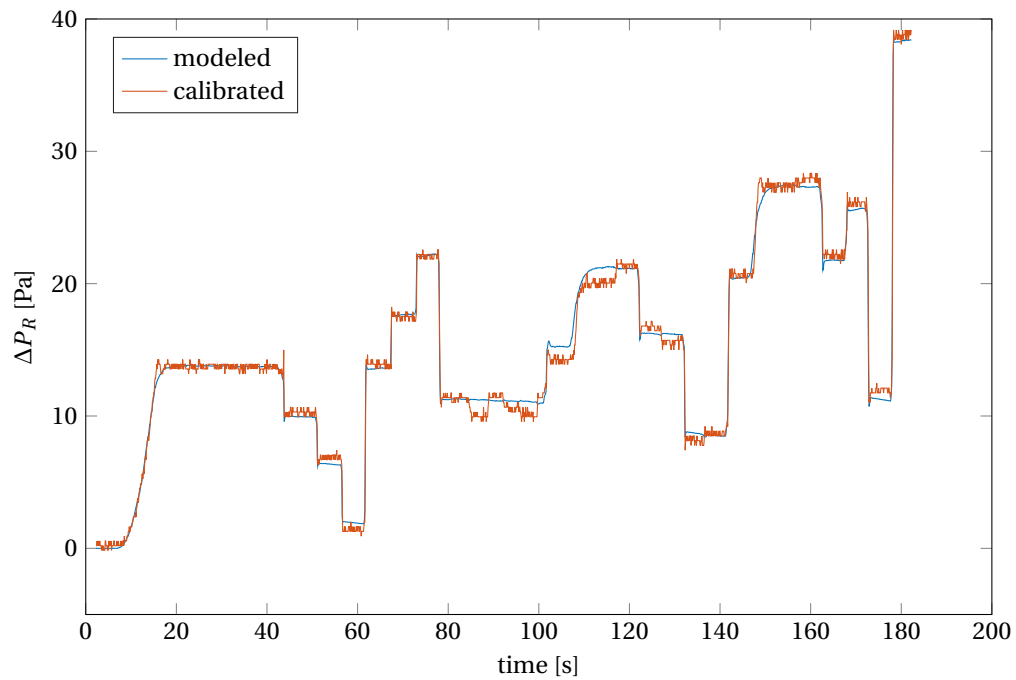


Figure 3.16: Calibration of ΔP_R assuming β equal to zero

A least squares linear fitting method was used to determine the parameter coefficients. A summary of the coefficient values performed for 4 different runs on 2 different days based on α in given in Table 3.24. The calibration of the side slip was also done for 2 runs on 2 different days given in Table 3.25.

Table 3.24: Calibration parameters for ΔP_α

run	f_{1_α}	SE_{f_1}	f_{2_α}	SE_{f_2}	R^2	a_{P_α}	SE_a	b_{P_α}	SE_b	R^2
run 1	2.528	0.010	-0.566	0.044	0.982	0.443	0.001	-0.165	0.022	0.992
run 2	2.375	0.006	-0.248	0.043	0.993	0.344	0.001	-0.167	0.014	0.996
run 3	3.136	0.006	-0.162	0.033	0.996	0.602	0.000	0.370	0.023	0.997
run 4	3.159	0.006	0.212	0.031	0.996	0.691	0.001	-1.136	0.031	0.997

Table 3.25: Results from wind tunnel testing

run	a_{P_1}	SE_a	b_{P_1}	SE_b	R^2	a_{P_β}	SE_a	b_{P_β}	SE_b	R^2	f	SE_f	R^2
run 1	1.130	0.002	0.013	0.151	0.998	0.329	0.001	0.0999	0.013	0.997	0.453	0.037	0.104
run 2	1.202	0.003	-1.050	0.210	0.996	0.453	0.001	0.462	0.016	0.997	0.620	0.027	0.286

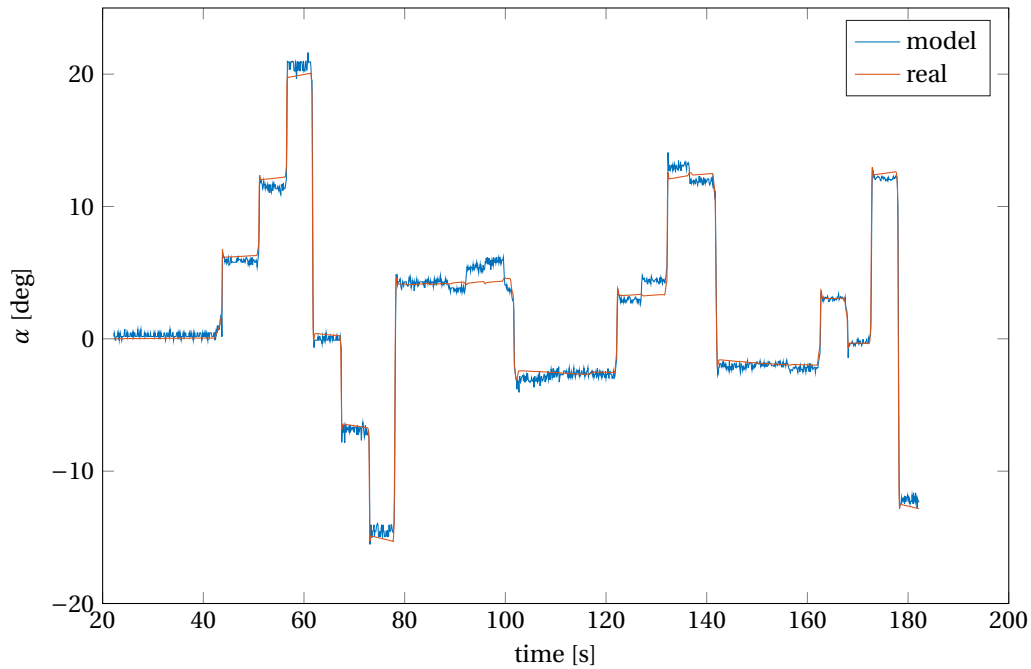
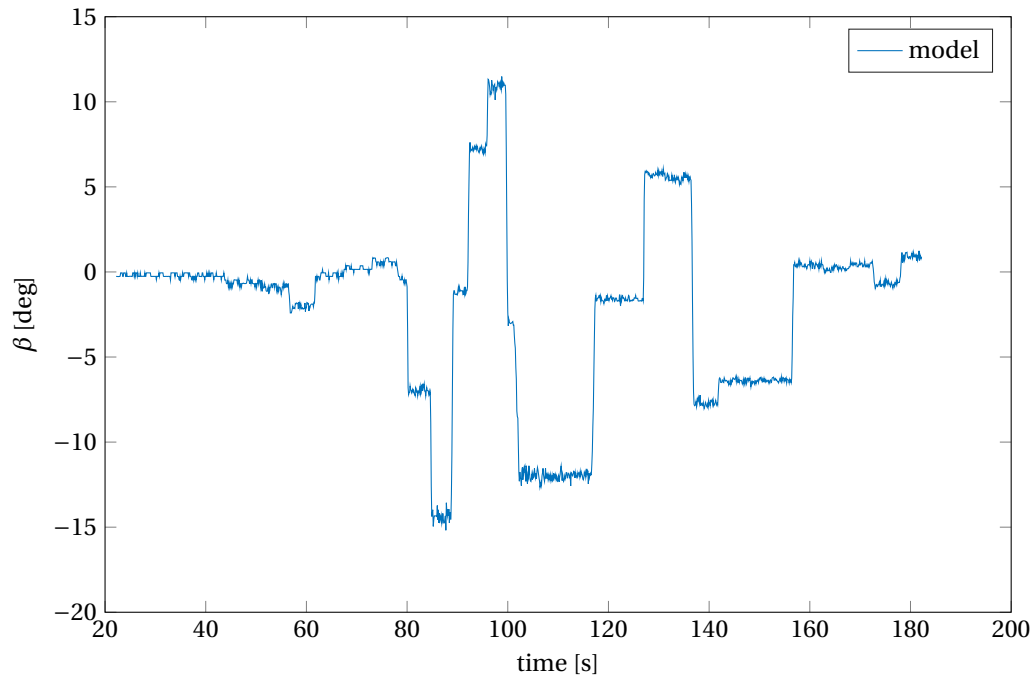
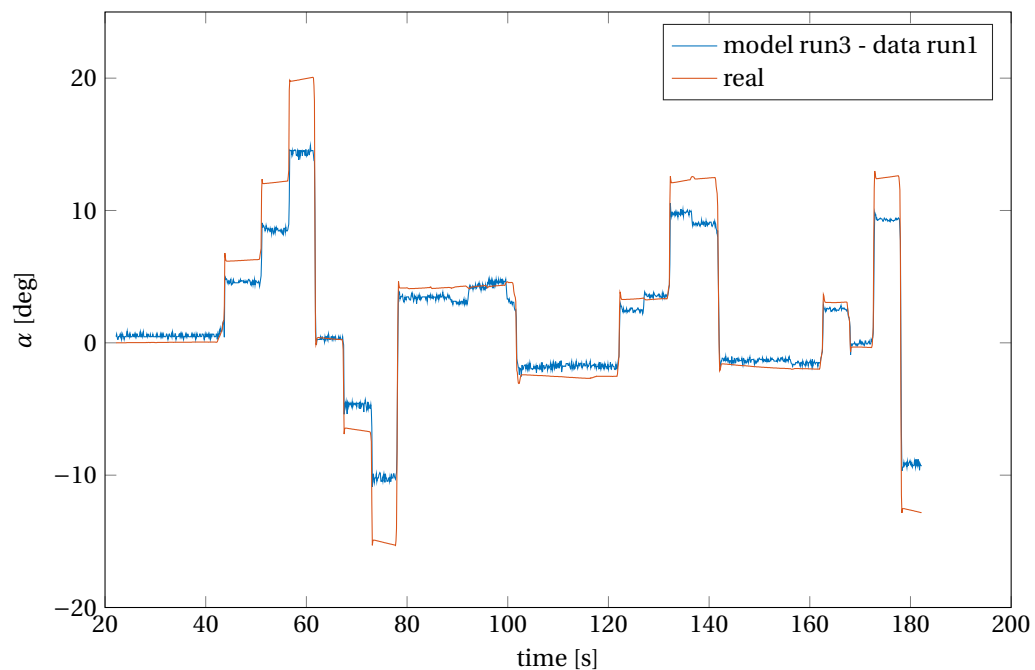


Figure 3.17: Calculation of α based on pressures

Figure 3.18: Calculation of β based on pressures

The values of α and β can be calculated analytically by combining the equations for ΔP_R , ΔP_α and ΔP_β . The equation for ΔP_R was adjusted with the parameters $f_{1\alpha}$ and $f_{2\alpha}$. The solution is therefore different depending on the values of these parameters. For example for run 1, the solution is given by Equation 3.23. The calculated values of α and β are obtained by using Equation 3.23. The value of α is displayed in Figure 3.17, the value of β is given in Figure 3.18.

$$\begin{aligned} \tan \alpha &= (400\Delta P_R\Delta P_\beta - 57\Delta P_\beta(49.25\Delta P_R^2 + 62.30\Delta P_R\Delta P_\alpha + 12.68\Delta P_\alpha^2)^{1/2} + 253\Delta P_\alpha\Delta P_\beta) / (114\Delta P_\alpha\Delta P_\beta) \\ \tan \beta &= \tan \alpha \Delta P_\beta / \Delta P_\alpha \end{aligned} \quad (3.23)$$

Figure 3.19: Calculation of α based on pressures measured during run 1 with the model calculated with the data of run 3

The value of α displayed in Figure 3.17 is calculated using the data from run 1. This model gives a good prediction with an *RMSE* of 0.639 and a maximum error in the prediction of α of 4.4 degrees. If the calibration parameters from run 3 are used to predict the value of α during run 1, the *RMSE* becomes 1.984. The maximum error in the prediction of α is in this case 8.39 degrees. This model is given in Figure 3.19. This shows that the variation of the estimated parameters has a large effect on the calculation of the true angle of attack and side slip angle.

The variation of the calibration parameters is partially caused by the accuracy of the sensor device itself. The differential pressure sensor has an error band of 1% over a range of 10 millibar. Implying that pressure variations of 10 Pascal cannot be eliminated from the results. The issue with this calibration method is that errors propagate through the formula's leading to large offsets in the final calculations of α and β . An additional source of error is given by the pressure reading of the Mensor Model 2101 digital pressure gauge which is sampled at 10Hz. This signal appears to be filtered as it does not capture fast changes in the tunnel speed. This influences the model fit and therefore also the calibration parameters.

4

CONTROLLER DESIGN

The first part of this chapter describes the control techniques used for attitude control. These controllers are used to obtain the desired roll and pitch angles. The controllers are all designed for the desired cruise speed condition of 10m/s. The phase-advanced sensors can be added as a feed-forward component to the ailerons, this is an independent element of the controller which can be switched on or off during testing. The second part of the chapter describes the outer loop control techniques used for autonomous flight in the wind tunnel using the OptiTrack system. The hovering condition is rarely experienced by MAV's outdoors, therefore different control techniques were used to adjust to this scenario.

4.1. INNER LOOP CONTROL

Two different control techniques are described in this section: INDI and PID controllers for roll and pitch with and without phase-advanced sensors. The controllers are designed based on the assumptions made in Chapter 3 and the state of the art knowledge described in Chapter 2.

4.1.1. INDI

The control laws for the INDI controller were derived in Chapter 3 by applying a Taylor series expansion at the cruise condition and by neglecting the higher order terms. The resulting equations were further simplified by applying the principle of time scale separation. The influence of the aerodynamic terms was neglected as it was smaller than the influence of the control surfaces. As explained in Chapter 2, the performance of the INDI controller is determined by the actuator dynamics, the second order filter and the sampling time. The actuator dynamics pose the limits to the performance in reference tracking. For disturbance rejection however, the performance is determined by the actuator dynamics, the second order filter and the sampling time. The design of the second order filter is explained in detail in this chapter. The INDI controller can only be started if the MAV is flying, during initialization on the ground the control surfaces have no influence on the attitude making the controller unstable. The INDI controller was therefore started when throttle values are above 25% of the maximum throttle. This ensured a stable take-off after MAV initialization.

ROLL

The control loop structure shown in Figure 4.1 is based on Equation 3.9. The dynamic damping term F_p is not included in this control structure but is incorporated in the disturbances term d which is an input of the block MAV. The INDI controller is given by the inner loop with virtual control input v and output the angular acceleration \dot{p} . The linear controller is used to determine the virtual control input v . The reference roll angle ϕ_{ref} is compared to the actual roll angle ϕ , the error is multiplied by a proportional gain P giving a reference roll rate. The reference roll rate is then compared to the actual roll rate p multiplied by a derivative gain D . For small pitch angles the roll rate can be used to approximate the derivative of the roll angle as stated by the kinematic relations given by Equation 3.2. The rate error is equal to the reference angular acceleration, called virtual control input v . The actual angular acceleration is calculated by differentiating the roll rate p through a second order low pass filter H . Filtering introduces a delay in the signal, therefore all signal shifted in time are denoted by the subscript f . In Chapter 3 aileron deflections were used to determine the angular acceleration, now the problem is reversed, the changes in angular acceleration are used to determine the

gain I . The integral resets when the throttle value is 25% of the maximum throttle or lower. This reset function was introduced for the wind tunnel tests. In the wind tunnel the MAV is initially laying on the platform to initialize the sensors and afterwards it is hanging on a string before take-off. During these phases the roll angle error should not and cannot be compensated for, therefore the integral term has to remain zero. During flight the proportional term and integral term are summed and used as the reference roll rate. The difference with the actual roll rate multiplied by derivative gain D is then used as input for the aileron deflection. The roll rate p is in this case used to approximate the derivative of the error which is used in traditional PID control structures. This approximation is only valid for small pitch angles as shown in the kinematic relations given by Equation 3.2. For the cruise condition analyzed in this master thesis project the pitch angle can be considered small enough to be neglected. Many traditional PID controllers require a reference model to smooth the reference signal allowing for higher gains and therefore a better performance. The advantage of using the roll rate p is that a reference model is not needed. In the control loop structure presented in this thesis fast changes in the reference signal will lead to fast changes in the roll angle which in turn cause high roll rates which have a damping effect on the controller output. The roll rate is in general a smoother signal compared to the derivative of the error leading to less noise in the output signal.

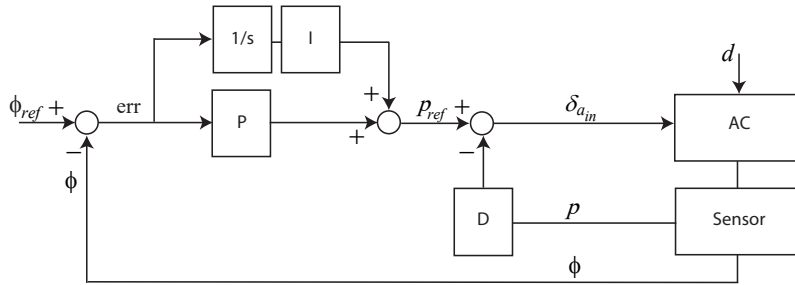


Figure 4.4: PID control block structure roll

The behaviour of the MAV in roll is defined by the aperiodic roll motion modeled by Equation 3.8. Two parameters are needed to determine the system response: the aileron deflection which depends on the output of the controller and the change in roll rate which can be predicted by using the full aerodynamic model of the Slick 360 Micro. The stability derivatives of the Slick 360 Micro are not known and will not be determined during this master thesis work. The PID gains can therefore not be calculated beforehand, but have to be determined experimentally during test flights. The gains were chosen to obtain the fastest possible reference tracking performance based on a step input of 0.4 radians. This was obtained with $P = 15000$, $D = 700$ and $I = 30$.

PITCH

The PID control loop structure for the pitch angle is given in Figure 4.5. The control loops are based on the traditional PID loop structure, the reference pitch angle is compared to actual pitch angle leading to an error signal. The error is multiplied by a proportional gain P and integrated to be multiplied by integral gain I . The derivative term is first multiplied by the proportional gain leading to a derivative gain D which depends on the proportional gain. If the proportional gain is increased, the derivative gain will also increase with the ratio determined by the factor D . This structure is used to make the tuning of the controller easier during test flights. The derivative of the error was in this case used instead of the pitch rate as this is the standard implementation for the Paparazzi Open-source autopilot system for fixed-wing aircraft.

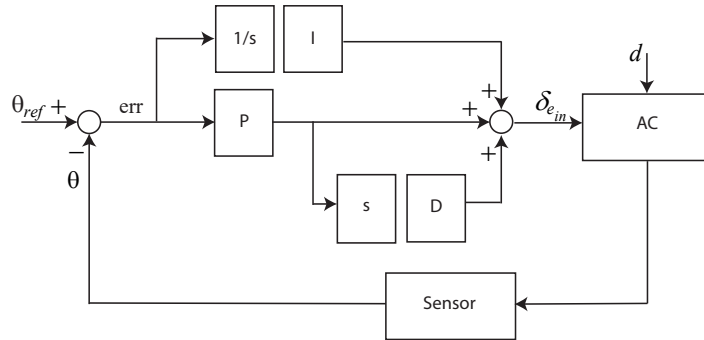


Figure 4.5: PID control block structure pitch

The theoretical calculation of the PID gains around the pitch axis is not possible for the Slick 360 Micro as the stability derivatives which predict the angle of attack and the pitch rate are not available. The gains will therefore be determined experimentally during test flights. The pitch axis is critical as it influences the flight speed of the MAV and the climb and descent performance. The gains used to maintain a stable flight can therefore be very different from the gains leading to the fastest performance. The definition of optimal gains depends in this case on the weight and weather conditions in which the test flight is executed. The pitch probes and GPS increase the weight of the MAV decreasing the flight envelope, a stall is reached at higher airspeeds compared to the clean configuration. It is therefore preferable to use lower PID gains to prevent abrupt changes in pitch angle. In the wind tunnel very small changes in pitch angle are allowed due to the limited space in which the MAV can be flown. In this scenario higher gains can be used due to the small changes in reference angle and due to the fast reaction time needed to stay within the boundaries of the wind tunnel. To be able to compare the PID controller to the INDI controller the fastest reference tracking performance is chosen as the main design focus. The fastest reference tracking is obtained with $P = 16000$, $D = 1.5$ and $I = 30$. Aggressive gains can however only be used if an airspeed controller is implemented to prevent stalls. Without the use of an airspeed controller it is recommended to lower the P gain to 4500.

4.1.3. PHASE-ADVANCED SENSORS

In the literature section it was shown that pitch probes sensors can be used as feed-forward components to the ailerons to counteract disturbances around the roll axis and to generate direct lift. The feed-forward implementation is shown in Figure 4.6.

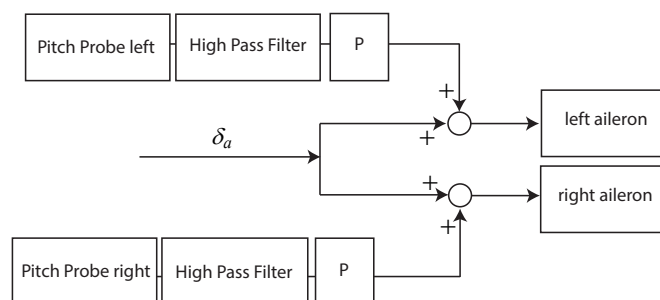


Figure 4.6: Feed-forward control probes

It is important to understand that the pitch probes sense all the changes in angle of attack of the incoming flow. These changes can however also be caused by the pilot or the controller. In that case the command should not be counteracted. Without an aerodynamic model of the MAV and without the knowledge of the stability derivatives the angle of attack induced by the input cannot be predicted. A different approach was chosen to distinguish between disturbances and variations induced by the controller. The power spectral

density of the input signals has more power at the low frequencies compared to the power spectral density of turbulence. Especially pilot commands have high power for very low frequencies as humans cannot react very fast leading to slow changes in pitch and roll angle. A controller on the other hand can give very fast inputs, therefore analysis of the power spectrum of the controlled signal is required to determine which frequencies are of interest.

Initially a simple second-order high pass filter was designed given by Equation 4.2. The cut-off frequency ω was set to 0.5 rad/s and the damping ζ to 1. These values were found experimentally and were determined for manual flight control.

$$H(s) = \frac{s^2}{s^2 + 2\zeta\omega s + \omega^2} \quad (4.2)$$

This filter was tested during the internship at RMIT by performing roll rig experiments with turbulence. Turbulence was generated by static grids placed at the inlet of the test section of the RMIT industrial wind tunnel described by Ravi [25] and used by Mohamed et al [4] for testing. The filter eliminates all biases and offsets present in the probe measurements as these are low frequency signals ensuring the pitch probes improve the signal and center the roll angle around zero as shown in Figure 4.7. Without the use of a high pass filter the probes cause offsets in the results as shown in Figure 4.8. During the RMIT wind tunnel testing the feed-forward gain of the probe was determined experimentally to give the best results for $P = 14000$.

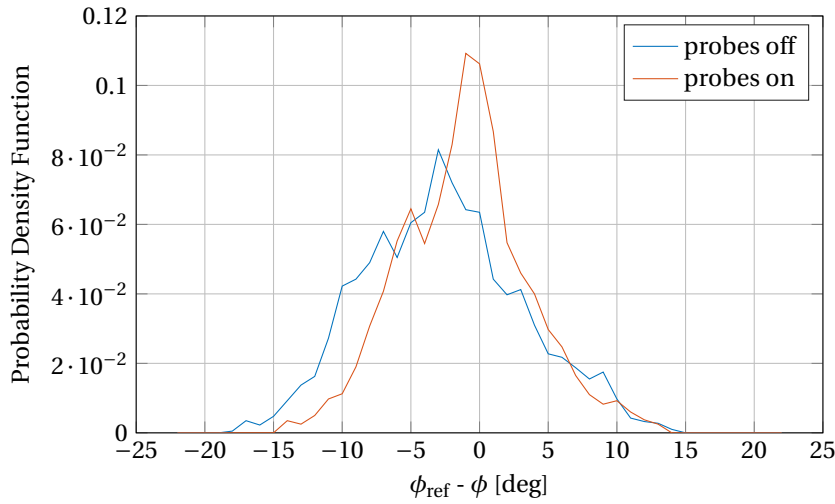


Figure 4.7: Probability density function for roll rig experiments at 10m/s with filter

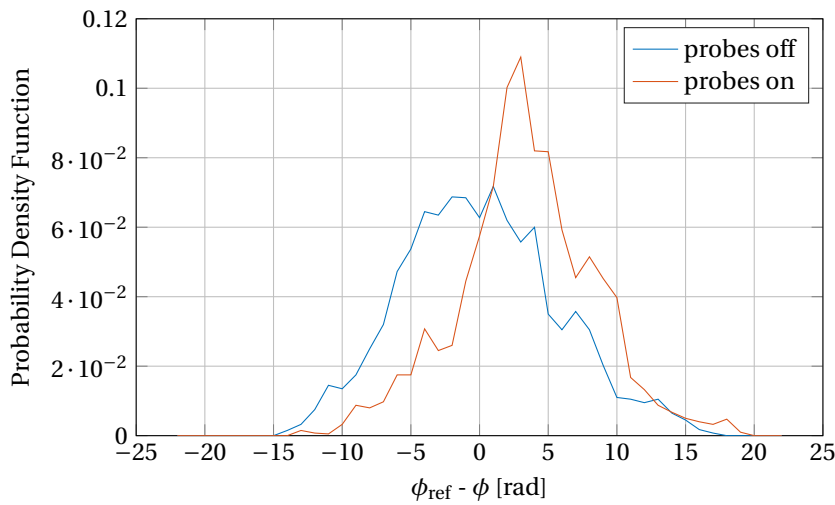


Figure 4.8: Probability density function for roll rig experiments at 10m/s without filter

During the OJF wind tunnel test the controllers are used to provide very fast steering movements. To improve the performance of the system a fourth order Butterworth filter was designed. The fourth order filter was determined based on the power spectral density function of the pitch probe signal for a time span in which inputs are given by the controller. The controller frequencies should not be counteracted as they are required by the controller to follow the reference signal. The high pass filter was designed in MatLAB by varying the cut-off frequency until a satisfactory pitch probe signal was created which would not interfere with the controller. The cut-off frequency was set to 4Hz (25 rad/s) with a sampling time of the sensor module of 128Hz. The transfer function of a fourth order high pass Butterworth filter is given by Equation 4.3.

$$H(z) = \frac{b(1) + b(2)z^{-1} + b(3)z^{-2} + b(4)z^{-3} + b(5)z^{-4}}{a(1) + a(2)z^{-1} + a(3)z^{-2} + a(4)z^{-3} + a(5)z^{-4}} \quad (4.3)$$

$$b = [0.773347 \quad -3.093387 \quad 4.640080 \quad -3.193387 \quad 0.773347]$$

$$a = [1 \quad -3.487308 \quad 4.589291 \quad -2.698884 \quad 0.598065]$$

4.2. OUTER LOOP CONTROL

In this section the outer loop control is described for both the wind tunnel flights and the outdoor flights. During the wind tunnel flight the position is controlled by using the GPS location and aircraft heading. During the outdoor tests an airspeed controller is used to maintain a constant airspeed.

4.2.1. THROTTLE CONTROL

The throttle is used in fixed-wing MAVs to control the climb and descent phases of the flight. The throttle is therefore always accompanied by a corresponding pitch angle calculated based on the reference climb rate. During the wind tunnel tests the throttle was also used to control the horizontal displacements in the wind tunnel direction (forwards/backwards). The vertical and horizontal loops are therefore coupled. The correction for forwards and backwards displacements has an influence on the climb loop. The gains could therefore not be tuned too fast, as the corrections made by one loop lead to errors in the other loop. The vertical controller used for testing the Slick 360 Micro is called Auto Throttle control. This control technique calculates the climb rate based on altitude and climb rate errors without the need to carry an additional airspeed sensor.

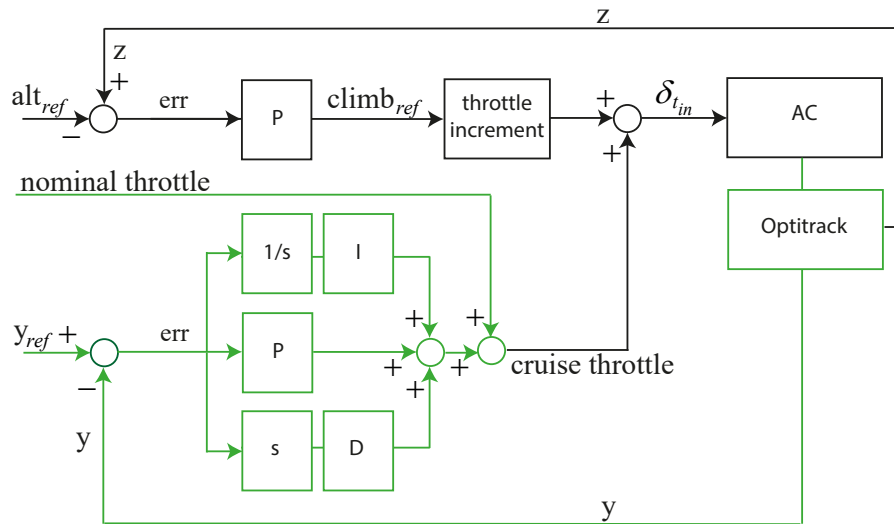


Figure 4.9: Vertical and horizontal throttle control block structure

The control loop structure for the throttle controller is shown in Figure 4.9. The altitude measured by OptiTrack system is compared to the reference altitude obtained from the flight plan. The reference altitude is in this case equal to the altitude of the waypoint towards which the MAV is flying. The altitude error is

multiplied by a proportional gain, giving the reference climb rate. In the wind tunnel the proportional altitude gain was set to 0.2 indicating that an altitude error of 10 meters corresponds to a climb rate of 2 m/s. The errors in the wind tunnel are in the order of 1 meter, therefore the climb setpoint is in the order of ± 0.2 m/s. The reference climb rate is used to calculate the required pitch angle in combination with the required throttle setting. The reference climb rate is then multiplied by the throttle increment which is summed to the cruise throttle value. The throttle increment is in this case 0.04. During outdoor flights the cruise throttle is a fixed quantity, during the wind tunnel tests the cruise throttle was varied to control the horizontal position. The horizontal position error is determined by the reference Y-position and the actual Y-position in the tunnel, this error was used as input for the PID controller. The nominal throttle value is the value at which the plane flies steady in one spot when no disturbances are present. This value was determined during manual test flight in smooth flow at 10m/s. The additions made to the Auto Throttle loop for indoor flight are shown in green in Figure 4.9.

4.2.2. VERTICAL PITCH CONTROL

The pitch controller is used for the descent and climb phases of the flight. The controller is based on the altitude error. An integral term was added to counteract small offsets which lead to displacements outside the tunnel cross section. The reference climb rate is directly used to calculate the pitch setpoint by using a feed-forward gain. The climb rate is however limited to ensure the aircraft can achieve the desired pitch setpoint without stalling. The derivative gain is calculated based on the difference between the climb reference and the climb speed. The changes designed for the wind tunnel set-up are highlighted in green in Figure 4.10.

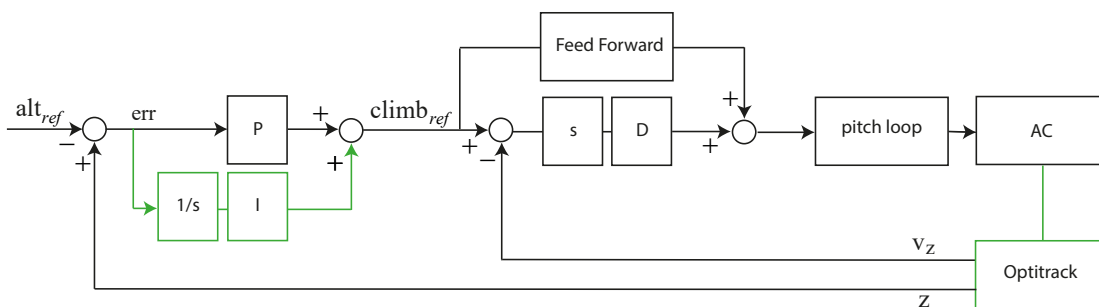


Figure 4.10: Vertical pitch control block structure

4.2.3. LATERAL CONTROL

In the wind tunnel the MAV can be considered fixed in one spot, a situation which is normally very unusual for fixed-wing aircraft and which can be encountered only during very strong wind. Normally, fixed-wing aircraft use the course angle to determine how to fly from one point to the other. The reference course angle χ_{ref} is calculated as the arctangent of the X and Y position errors. The current course angle is defined as the arctangent of the x and y ground speed velocity components. In this case however, the position displacements are close to zero varying constantly by very small amounts. In this scenario, lateral movements of the MAV lead to a course angle varying from $+90$ to -90 deg. If the course error indicates that the MAV has to move to the right, small movements result in a course approaching $+90$ deg to the right leading to a compensating command to the left and so forth. The MAV would therefore constantly jump from one extreme to the other without being able to move the aircraft to the desired position. The scenario in which the course angle is larger than 90 deg results in a 360 deg turn in the wrong direction, which clearly shows that this angle cannot

be used for lateral control in the wind tunnel. The heading angle ψ is normally not reliable indoor as it is calculated by the magnetometer, in this case however the OptiTrack system is used to determine the heading providing a very accurate measurement.

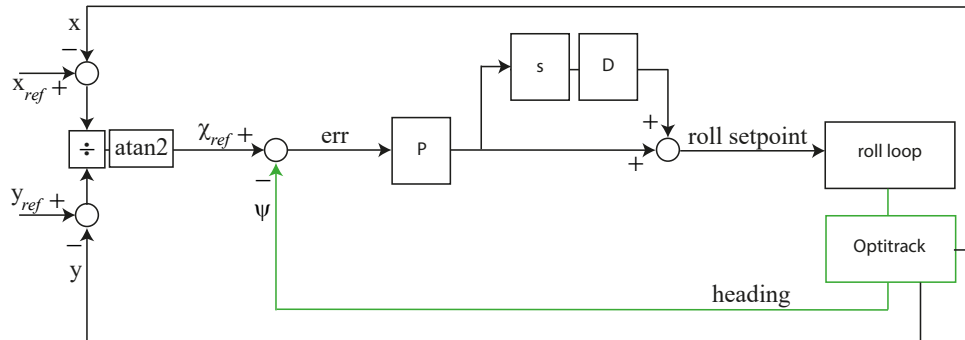


Figure 4.11: Lateral control block structure

Figure 4.11 shows how the heading is used for control. The P and D gain are tuned to achieve a fast response time. During the flight the waypoint can be moved closer or further away as a gain. The closer the waypoint is to the MAV the larger the course error will become for any lateral movement. During outdoor flights the Paparazzi control systems uses the *Carrot*, an intermediary reference value which looks a few seconds ahead in time based on the nominal flight speed of the MAV. The *Carrot* calculates the reference course angle based on the distance the MAV will fly in the next seconds. This however is not a useful feature in the wind tunnel. This will cause the system to believe the MAV will reach the waypoint within a few seconds and will stop giving commands and move to the next block in the flight plan. This feature was therefore turned off during the wind tunnel tests.

4.2.4. OUTDOOR AIRSPEED CONTROL

During the outdoor flight the airspeed is controlled by adjusting the throttle level. An overview of the airspeed controller is given in Figure 4.12.

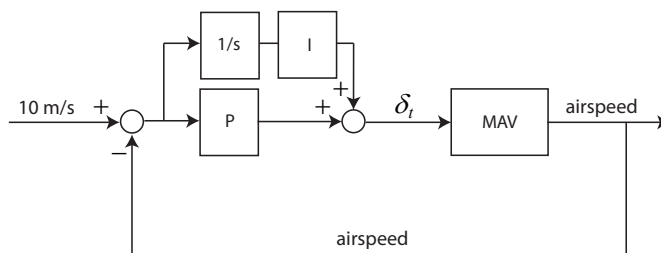


Figure 4.12: Lateral control block structure

The throttle level δ_t is determined based on the airspeed error multiplied by a proportional gain P and incremented by the integral gain I.

5

EXPERIMENTAL SET-UP

The indoor tests were all performed in the Open Jet Facility (OJF) at Delft University of Technology. The platform used during the experiments is the Slick 360 Micro with the Open Source Paparazzi Autopilot system

5.1. SLICK 360 MICRO

The Slick 360 Micro is an aerobatic model made out of foam with standard control surfaces (ailerons, elevator and rudder). The model is sold by HobbyKing all over the world but is not produced any longer. The most important parameters are given in Table 5.1. The overview of the Slick 360 is given by Figure 5.1.

Table 5.1: Slick 360 Micro characteristics

Wing Span [cm]	49
Chord [cm]	8.85
Weight basic setup [gr]	115
Weight with probes [gr]	130
Weight with probes and GPS [gr]	160



Figure 5.1: Slick 360 Micro model with autopilot and sensors

The Paparazzi Open-Source Autopilot system was used both for the hardware components and for the software. The Lisa M autopilot was installed with an Aspirin IMU system equipped with gyroscopes, accelerometers and magnetometers. An RC receiver with Spektrum protocol was used to control the MAV during test flights. For the indoor flights in the wind tunnel a wireless ESP chip was used to connect to the MAV from the ground station computer. To make the system autonomous the ESP chip was used to send the position data from the OptiTrack to the MAV. For the outdoor test flights an XBee chip was used as datalink connection to provide a longer range. During the autonomous outdoor flights a GPS receiver was also added to the system to obtain position data. Pressure probe sensors produced by Honeywell of the

type HSCDRRN010MDAA3 were used to measure the pressure differences. These sensors are very sensitive to small changes in pressure with a range of ± 10 mbar. The sensors operate at 3.3V which can be supplied directly by the Lisa M autopilot. A schematic of how the components were connected during the wind tunnel tests is given in Figure 5.2.

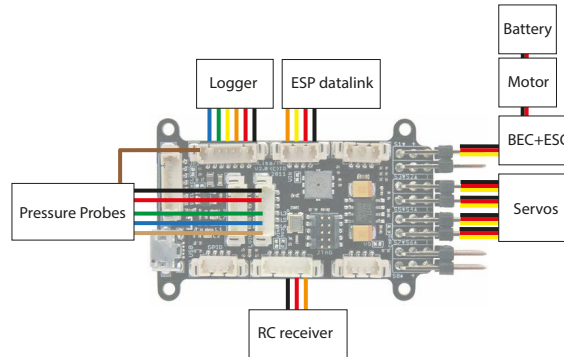


Figure 5.2: Lisa M autopilot component wiring diagram

5.2. OJF

A schematic of the OJF wind tunnel is given in Figure 5.3. The OJF tunnel cross section is 285×285 cm. The space used to fly the MAV can be defined as a box of $5 \times 5 \times 5$ meters, parallel to the wind tunnel cross-section and flow direction. The Y axis is defined opposite to the flow direction, the X axis is defined to the right and the Z axis to the top. The origin of the reference system is in the middle of the wind tunnel cross section, just underneath the start of the inlet. The Y-axis is also defined as being in the North direction, therefore a heading angle of 0 deg will be measured when the MAV is flying opposite to the flow direction. The OptiTrack positioning system sends the position coordinates to the MAV in this reference system.

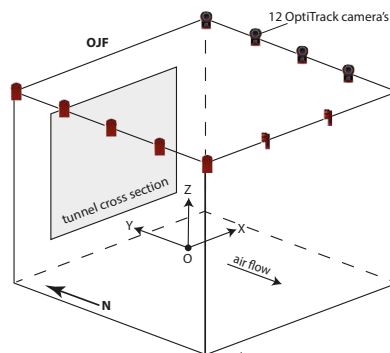


Figure 5.3: OJF wind tunnel coordinate system definition

5.2.1. OPTITRACK SYSTEM

The OptiTrack system is a platform which consists of infrared camera's and motion capturing software. In the OJF 12 camera's were placed on the ceiling covering the wind tunnel test section with the dimensions of approximately $5 \times 5 \times 5$ meters. The MAV was equipped with 4 infrared markers placed in a unique pattern to reflect the light of the infrared camera's. The system measures the position and velocity of the body at 120 frames per second with millimeter accuracy. The position, heading and velocity information is sent to the

MAV at 20Hz through the datalink connection. The speed at which the data can be sent to the MAV depends on the datalink connection, with the ESP chip a data rate of 20Hz was achieved.

5.2.2. PITCH AND ROLL RIG SET-UP

In order to model the aircraft dynamics around the roll and pitch axis, a rig was constructed. This rig allows to model the roll and pitch axis independently and to assess the controller behavior before performing an actual test flight. At RMIT the experiments on the pressure probe functionality were performed in a roll rig set-up. Building on this idea a rig was constructed at TU Delft for both the roll and pitch axis, see Figures 5.4 and 5.5. The rig consists of a fixed part, which can easily be attached to the OJF tunnel floor and a movable

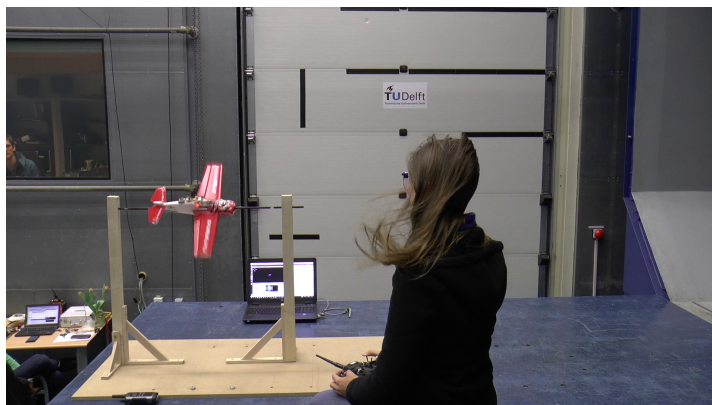


Figure 5.4: Roll rig set-up

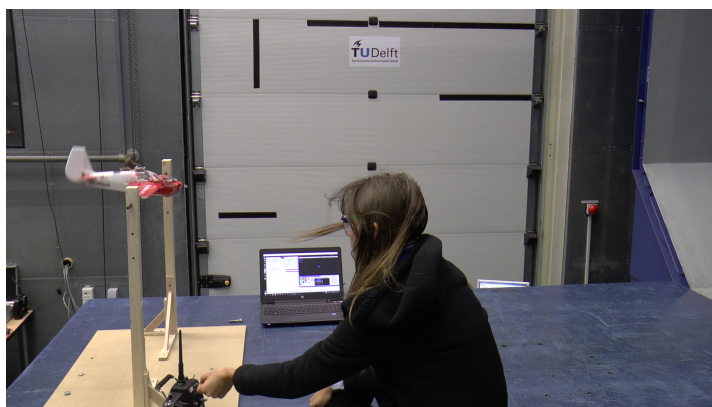


Figure 5.5: Pitch rig set-up

rod which can be configured for both roll and pitch. During the design of the rig special attention was given to the bearings of the rod. The bearings were taken from a small model helicopter such that the friction is reduced to the minimum. It has to be taken into account however that the rod will experience some friction when rotating in the rig structure, this friction can therefore influence the model results. The rig construction was created in a relatively short time and had therefore not been optimized for turbulence reduction. The construction rods were made out of rectangular pieces of wood which create turbulent flow over the center of the MAV during the roll rig set-up. The turbulence induced by the rig can influence the model of the MAV around the roll axis leading to differences with the free stream condition. For the roll rig set-up, the rig rotational axis passes through the aircraft body from the thrust line to the tail. Attention was paid to align this axis with the center of gravity of the vehicle. There can however be differences in the vertical location of the center of gravity with respect to the rotational axis, leading to errors in the model identification. For the pitch rig set up the rotational axis passed through the quarter chord line which corresponds to the center of gravity location. Errors in the center of gravity location can in this case also lead to errors in the model identification. All the uncertainties mentioned above have to be taken in account when identifying the model parameters compared to the results in free flight.

5.2.3. FREE FLIGHT SET-UP

The free flight set-up was used to test the performance of the INDI and PID controller after a stable response was observed in the roll and pitch rig. The wind tunnel cross section is very small and recovery after the MAV exits the tunnel is impossible as the airflow suddenly disappears making the plane uncontrollable. A string was therefore attached from the MAV center of gravity to the wind tunnel ceiling. The string was made out of 0.8mm fishing wire to be as light as possible. While the MAV is suspended on the string the forces and moments cannot be represented by the equations of motion shown in Chapter 3. The INDI controller can therefore not be used during the take-off phase of the flight as the incremental control law quickly increases to the maximum input. The PID controller is an error based controller, with an incremental term which resets for throttle values below 25%. For throttle values below 25% the PD controller is used to maintain a stable attitude, as soon as the control surfaces start to become effective the INDI control can be turned on or the incremental term of the PID controller becomes active. The throttle threshold value is much lower than the values experienced during the cruise phases of the flight (40%-60%), meaning the control loops are not affected during the cruise phase which is used to analyze the controller performance.



Figure 5.6: Free flight in OJF

5.2.4. TURBULENCE GRIDS SET-UP

At RMIT meshed grids are used to create well mixed turbulence. In the OJF no previous set-up of this kind was used. During this master thesis project a limited amount of time was available to construct the grids. The grids were therefore made out of existing components available from the Control and Simulation Department. The grids are made out of metal rods, evenly spaced in the vertical direction. Two of these sets of grids were placed next to each other to cover the entire test section leaving a small gap at the top. The grids used in this set-up do not resemble the perfect meshed grids required for well mixed turbulence. The vertical bars in the middle connecting the two sections form a wake which has different turbulence characteristics with respect to the rest of the test section. The turbulence in the vertical and horizontal direction is also different as the metal bars are only present along the vertical direction. The turbulence intensity and its variations could not be determined during the test week. A hot-wire set-up was investigated but only 1-axis hot wires were present and unfortunately not working at the time of the test. Cobra Probes were the first choice for determining the turbulence profile. These could however not be bought for this Master thesis work due to the limited budget. The 5-hole pressure probes were therefore used to measure the 4 differential pressure components. After the 5-hole pressure probes were calibrated, damaged tubes were discovered which make these measurements unreliable and therefore not suited for analysis of the turbulence intensity profile. Creating a turbulence intensity profile for this set-up would require measuring the turbulence at different locations in 3D space for the entire flight area of the MAV, defined as the $5 \times 5 \times 5$ m box shown in Figure 5.3. The flight area is very close to the actual grids meaning a large variation of turbulence intensity can be expected along the Y-axis.



Figure 5.7: Turbulence grids set-up

5.3. SENSOR CALIBRATION

To calibrate the sensors a special set up was designed as given in Figure 5.8. The autopilot was mounted on a stand which could be rotated to change the angle of attack and the side slip angle experienced by the sensor. The sensor was placed 380mm in front of the point of rotation and 360mm in front of the autopilot mounting board.

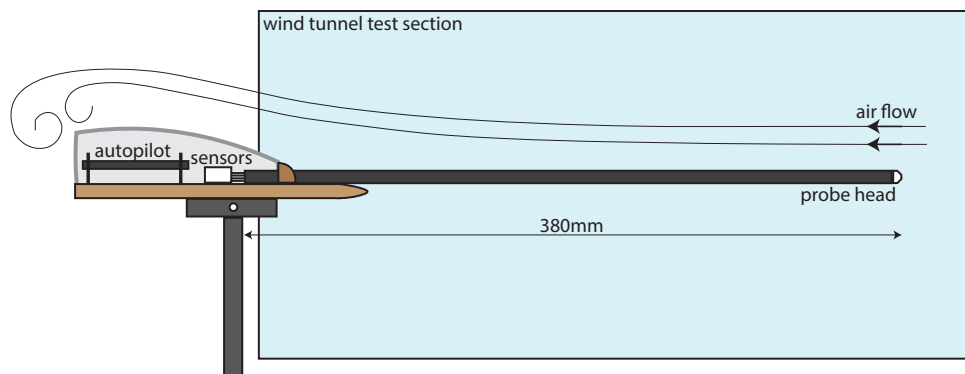


Figure 5.8: 5-hole probe calibration set-up

6

RESULTS

The results section is divided into three part: preliminary outdoor flights, autonomous wind tunnel flights and airspeed controlled outdoor flights. The preliminary outdoor flights were performed to check the basic functionality of the controllers and to obtain data on the reference tracking performance of the system. The wind tunnel flights show an innovative approach to autonomously control the position of the MAV within the tunnel cross section. The wind tunnel flights provided a series of insights which led to improvements in the INDI and PID controller parameters. Specific tests were also developed to ensure the pressure probe system did not contain any leaks. With improved parameters final outdoor tests flights were executed. The final outdoor tests show the disturbance rejection performance of both controllers and include the pressure probes as feed-forward component to enhance the system performance.

6.1. PRELIMINARY OUTDOOR FLIGHTS

This section presents the reference tracking responses of the PID and INDI controller obtained during outdoor tests. The reference tracking section is important as it determines whether a fair comparison can be made between PID and INDI in turbulence. The comparison of INDI and PID will be made for both the roll and pitch axis for doublet inputs. The reference tracking tests were all performed during outdoor test flights on a day with no wind and therefore very low turbulence intensities. The preliminary controller parameters for INDI are given in Table 6.1 and for PID in Table 6.2.

Table 6.1: Preliminary parameters of the INDI controllers

	Roll	Pitch
P	400	400
D	22	22
G	0.019	0.014
ω_n	3.2	1.6

Table 6.2: Preliminary parameters of the PID controllers

	Roll	Pitch
P	12500	4500
I	1	1
D	700	1.5

6.1.1. ROLL AXIS

The reference tracking tests were done during outdoor test flights. To ensure the results of the doublet inputs are valid in general, three difference moments during the test flight are considered. The results for the PID controller are given in Figure 6.1. The three curves are very similar with no overshoot and a comparable rise time. The rise time was calculated at the first step input from 0 to approximately 0.5 seconds. The values of the rise time for this time period are given in Table 6.3.

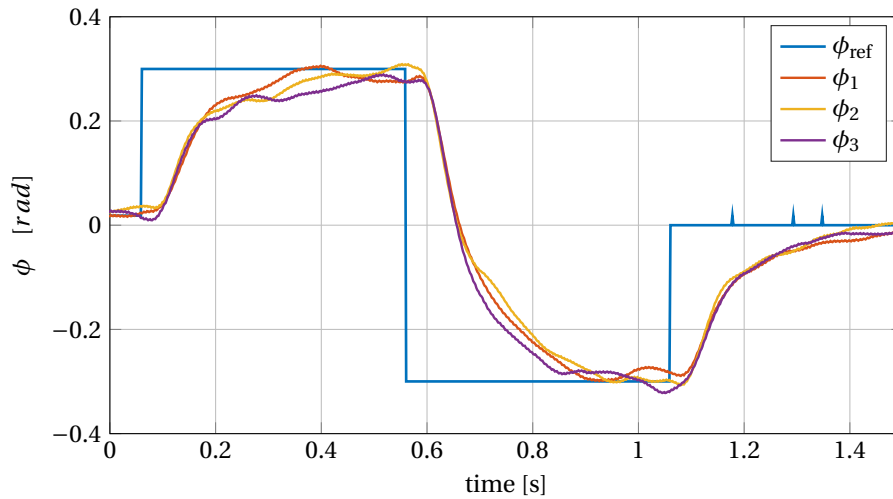


Figure 6.1: Roll angle during the doublet for the PID controller

Table 6.3: Rise time of the first step input for PID roll angle controller

Variable	ϕ_1	ϕ_2	ϕ_3
Rise time	0.246	0.297	0.398

The INDI controller response to doublet inputs is given in Figure 6.2. The response is similar for the three tests with a fast rise time followed by some overshoot. The values for the rise time and overshoot calculated for the first step input between 0 and 0.5 seconds are given in Table 6.4.

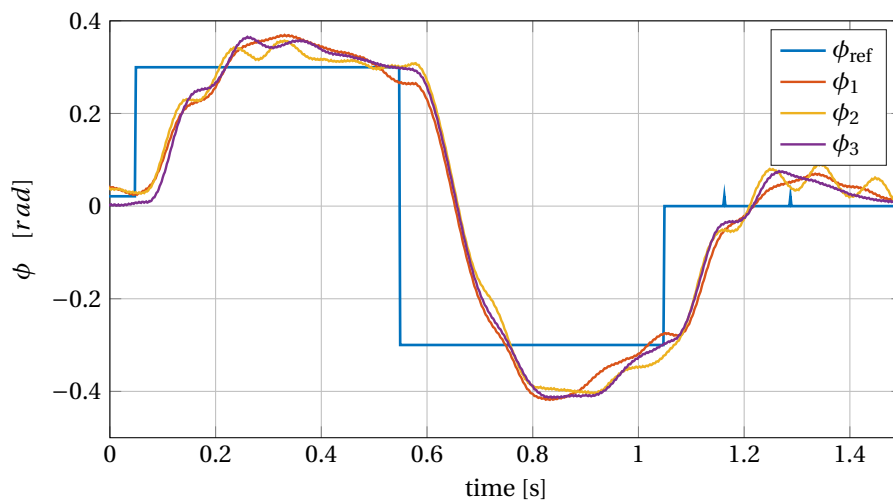


Figure 6.2: Roll angle during the doublet for the INDI controller

Table 6.4: Rise time and overshoot of INDI controller

Variable	ϕ_1	ϕ_2	ϕ_3
Rise time	0.160	0.150	0.160
Overshoot	0.070	0.057	0.066

The performance of the PID and INDI is comparable around the roll axis. The INDI controller has a faster rise time but more overshoot whereas the PID controller has a slower rise time with no overshoot. The similarity of the responses can be improved by increasing the PID gains or decreasing the INDI gains.

It is a matter of preference whether a faster rise with overshoot is preferred over a slower rise time with no overshoot.

6.1.2. PITCH AXIS

In Figure 6.3 three different moments are displayed during the test flight with the PID controller for the same doublet input. The transient response to the first step input has not died out before the next input is given. The rise time of the the first step input is variable as the starting angle is different for the three test cases as shown in Table 6.5. This clearly shows that a steady-state error is present indicating the integral gain should be increased.

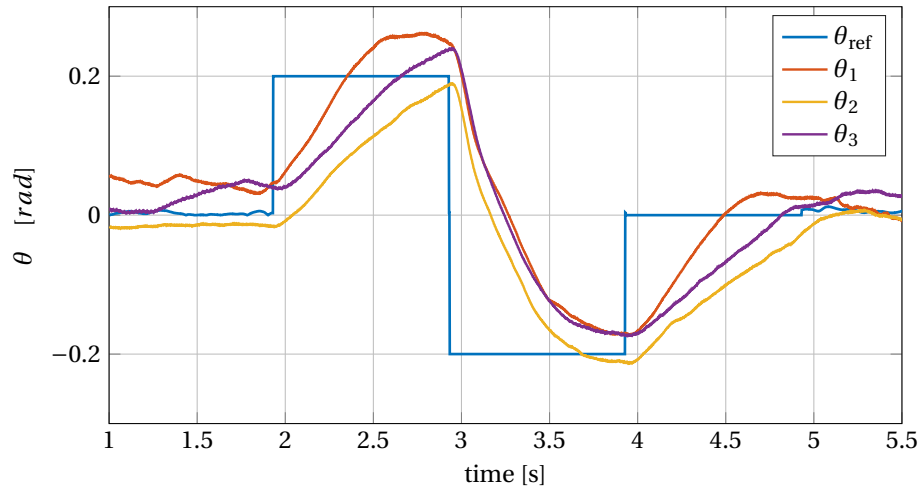


Figure 6.3: Pitch angle during the doublet for the PID controller

Table 6.5: Rise time of the first step input for PID pitch angle controller

Variable	θ_1	θ_2	θ_3
Rise time	0.038	0.095	0.064

The INDI controller has a much faster response around the pitch axis as shown in Figure 6.4. The three test cases are nearly identical with a short rise time and some overshoot. The overshoot is on average 0.046 radians and the rise time 0.015 seconds, the values are given in Table 6.6.

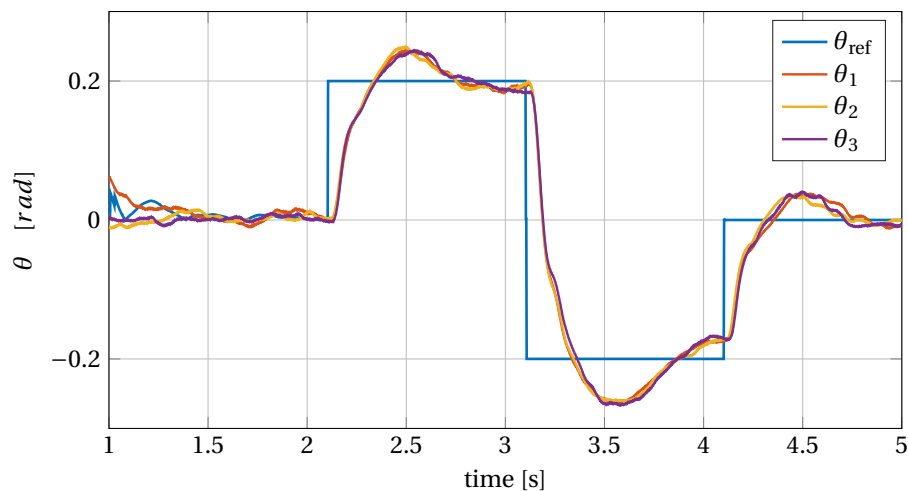


Figure 6.4: Pitch angle during the doublet for the INDI controller

Table 6.6: Rise time of the first step input for INDI pitch angle controller

Variable	θ_1	θ_2	θ_3
Rise time	0.015	0.015	0.016
Overshoot	0.044	0.049	0.044

To ensure the MAV was experiencing exactly the same conditions during the flight, the reference tracking response of the INDI controller was immediately followed by the response of the PID controller as shown in Figure 6.5. The difference between the two controllers is clearly visible and shows that the reference tracking performances are not comparable. This major difference is mainly due to small flight envelope of the Slick 360 Micro which led to prefer a slow pitch response to prevent stalling the aircraft in mid air. These gains were in hindsight not suitable for the purpose of comparing the disturbance rejection performance of the PID and INDI controller in the wind tunnel. Low gains are optimal for outdoor flights where small variations in height are acceptable and where large margins need to be taken as the MAV airspeed is not controlled. During autonomous outdoor test flights, the INDI controller caused several stalls due to aggressive pitch maneuvers.

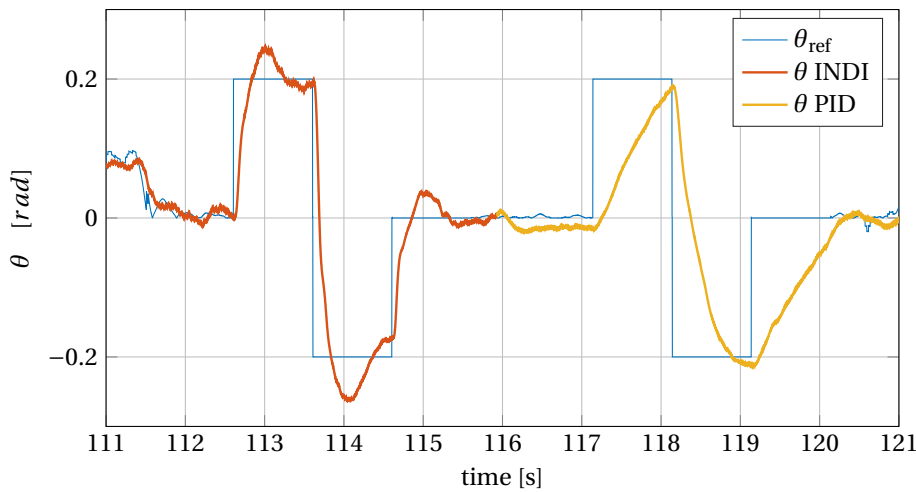


Figure 6.5: Comparison of reference tracking pitch angle during the doublet for the PID and INDI controller

6.2. AUTONOMOUS WIND TUNNEL FLIGHTS

The results of the disturbance rejection tests were all obtained in the OJF with the turbulence generating grids at a speed of 10m/s in fully autonomous flight. The data was obtained for the INDI attitude controller with and without pressure probes and for the PID attitude controller. The PID attitude controller was not able to fly in the tunnel for more than a couple of seconds making it very difficult to obtain data for the analysis of the performance. The INDI controller was much more precise and could therefore be flown within the tight wind tunnel test section even with turbulence generating grids. The differences between the INDI controller with and without probes are analyzed in this section. The tubes connecting the probe head to the sensor were later discovered to have small cuts which influence the pressure reading. The results can therefore not be used to make final conclusions on the effect of the probes on the disturbance rejection performance.

INDI WITH AND WITHOUT PROBES

The effect of the pressure probes was investigated in two test flights. In the first test flight only very little data on the probes is available as the MAV flew outside of the tunnel when the PID attitude controller was activated. In total 9 seconds of data are available in which the INDI controller with pressure probes was active. This data is compared to the 9 seconds of data immediately before the probes were activated. The time frame in which the data was collected is too short to make final conclusions on the effect of the pressure probes. Many sources of error can influence the results in such a short time span. The position of the MAV determines the turbulence intensity as the MAV was flying in a range between 0 and 5 meters from the turbulence generating grids. The turbulence itself can also be varying in intensity over short time periods and therefore not be equal during the two time frames. The results of this test are shown in Figure 6.6. In Figure 6.6a the results for the roll axis are given. The probes improve the performance around the roll axis as the peak of the

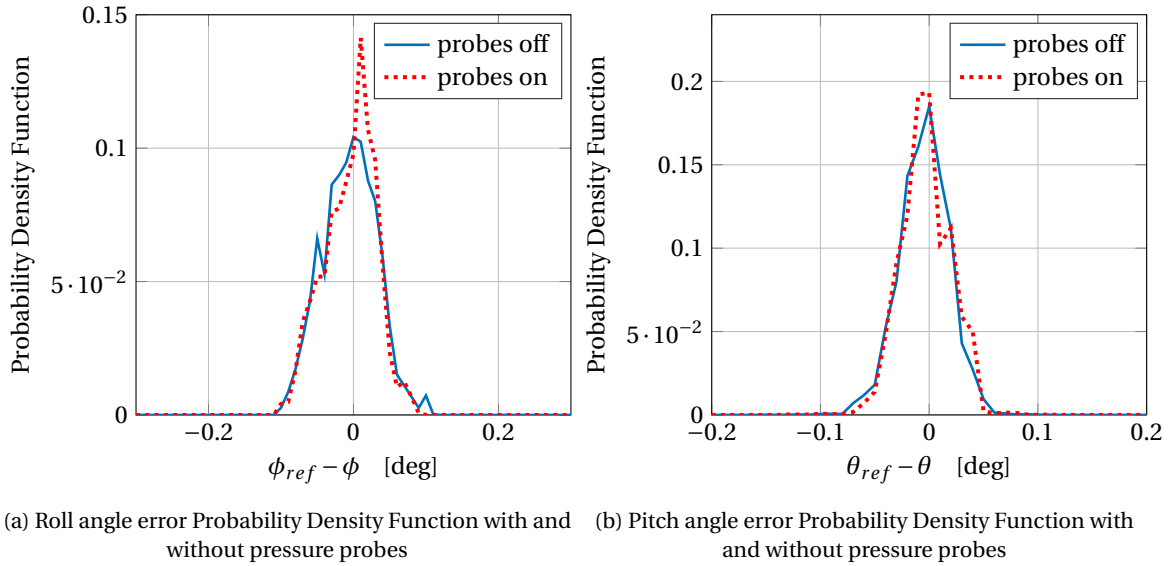


Figure 6.6: Comparison with and without pressure probes for the first flight

probability density function is higher and therefore more centered around small errors in the roll angle. In Figure 6.6b the probes seem to improve the performance slightly around the pitch axis.

The second test flight was aimed at analyzing the effect of the pressure probes in combination with the INDI controller and more data was obtained. In total 3 segments of 14 seconds for the INDI controller with and without probes were collected. The three segments are compared to understand if the time span used to analyze the performance is sufficient to make general consideration about the effect of the probes.

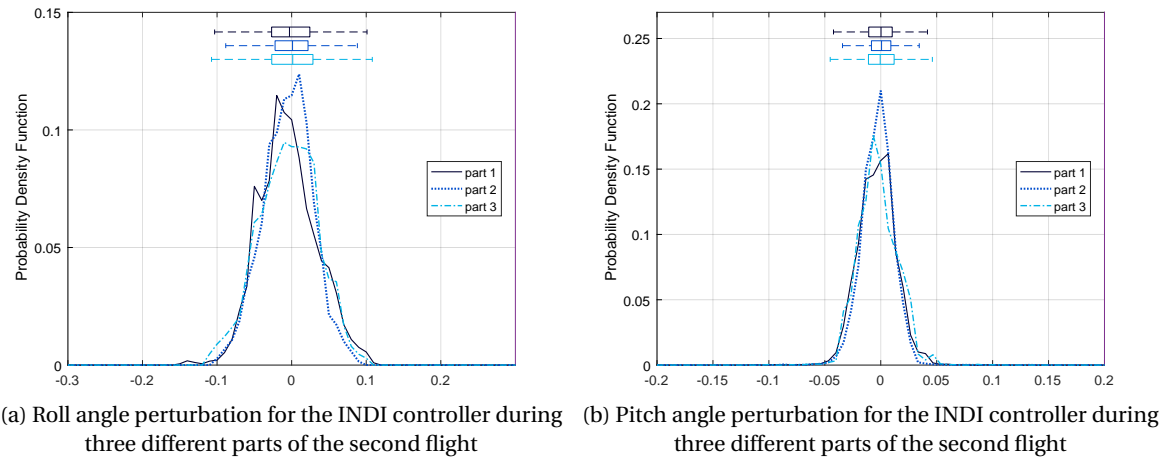


Figure 6.7: Performance of the INDI controller during three different parts of the second flight

The INDI controller performance without probes is displayed in Figure 6.7. The probability density function for the roll axis is given in Figure 6.7a. The difference between the box plot ranges and the peak values is not negligible. The largest difference occurs between run 2 and 3, the box plot range increases by 18% for run 3 with respect to run 2. For the pitch axis the results are given in Figure 6.7b. The probability density functions show different peaks and box plot ranges, with the largest differences experienced between run 1 and 2. The box plot range of run 1 is 19% more compared to run 2.

To variation in box plot ranges is related to two major factors. The first is the variable position of the MAV in the wind tunnel close to the turbulence generating grids. The closer the MAV flies to the grids the larger the turbulence intensity it will experience. Secondly the turbulence intensity may not be constant for a specific location in the wind tunnel for such a short period of time. A larger time period should therefore be considered to obtain the same average turbulence intensity.

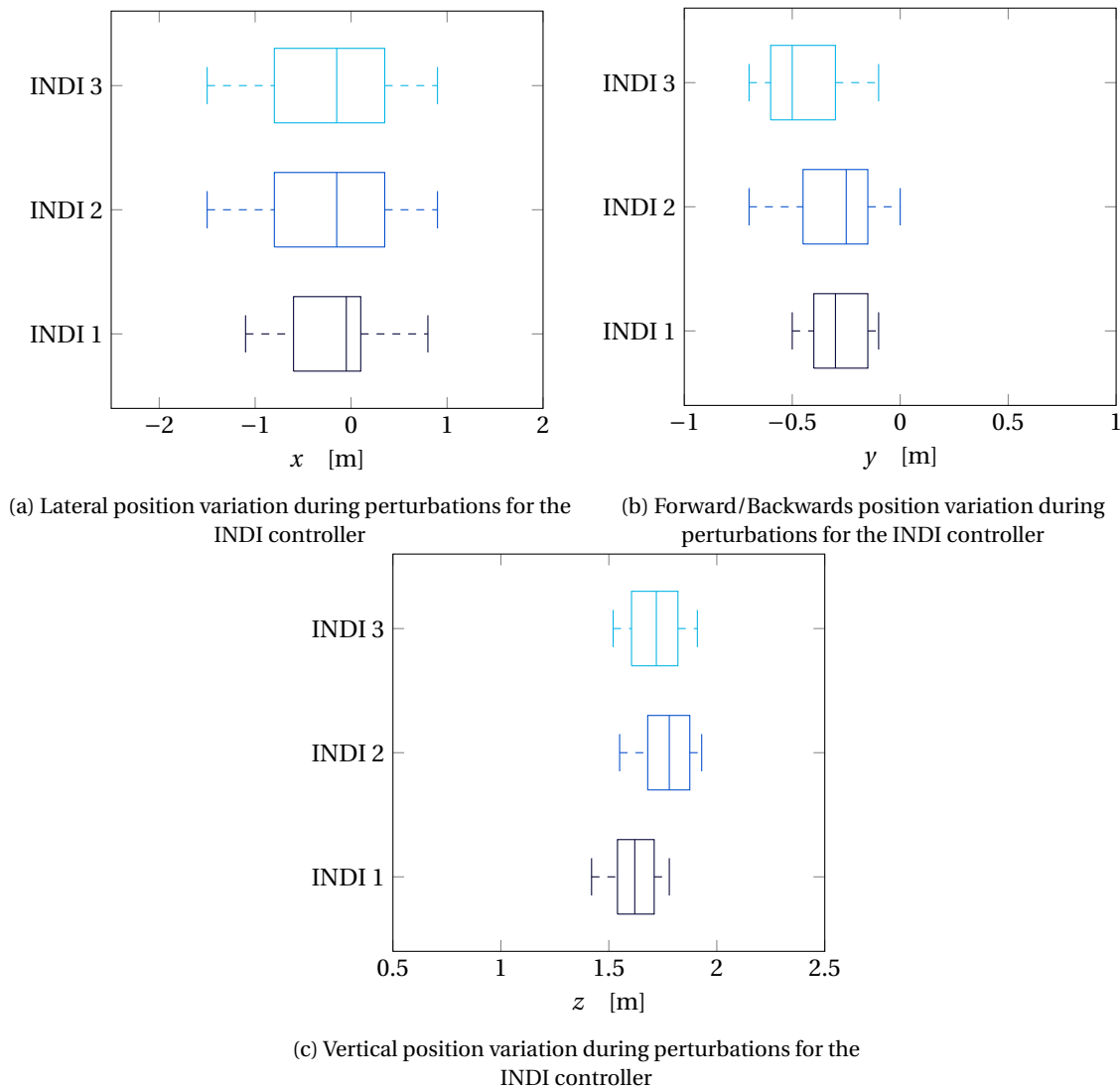
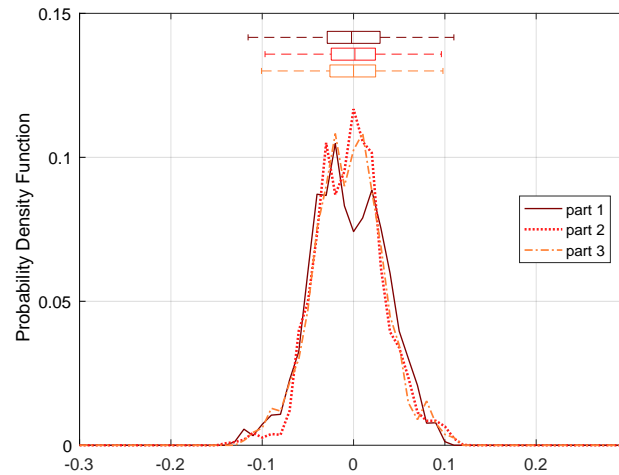


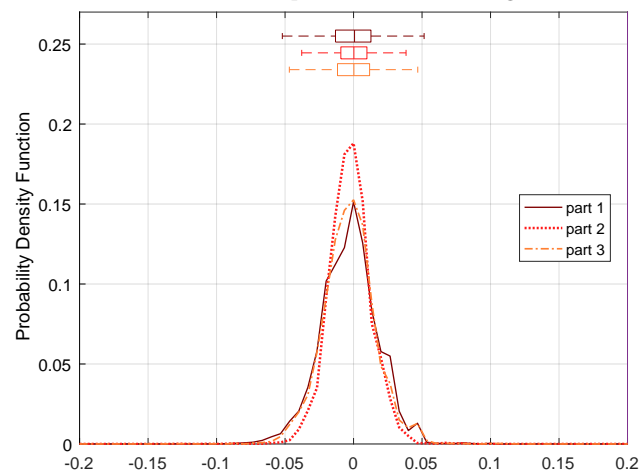
Figure 6.8: Position perturbation comparison for the INDI controller without probes

The position of the MAV in the wind tunnel was logged by using the OptiTrack system. The variation in lateral, longitudinal and vertical position is given in Figure 6.8. In Figure 6.8a it can be seen that the lateral position is very similar for all three runs and can therefore not lead to any difference in the results. In Figure 6.8b the backwards/forwards position is given. This position has the most influence on the turbulence intensity and should therefore be as similar as possible for the three runs. Runs 1 and 2 are closer on average to the grids and will therefore experience a higher turbulence intensity. Counter intuitively this leads to a better performance around the roll axis indicating more factors may influence the results. In Figure 6.8c the height at which the MAV was flying in the wind tunnel is compared. The first run has the lowest average height but in general the height is similar for the three runs. No major difference can be observed when looking at the position of the MAV during the three test runs indicating a longer time span should be chosen to compare the results.

The INDI controller performance with the probes is given in Figure 6.9. The performance around the roll axis for three different sets of data is given in Figure 6.9a. The main difference is present between runs 1 and 2, as the peak for run 1 is not placed around the zero value but shifted toward to the left. The range of the boxplot for run 1 is 14% more compared to run 2. For the pitch axis the results are given in Figure 6.9b. Runs 1 and 3 are very similar but run 2 shows large improvements around the pitch axis as the box plot range of run 2 is 27% less compared to run 1.



(a) Roll angle perturbation for the INDI controller with probes during three different parts of the second flight



(b) Pitch angle perturbation for the INDI controller with probes during three different parts of the second flight

Figure 6.9: Performance of the INDI controller with probes during three different parts of the second flight

To analyze whether the variation in performance between the runs is due to the position of the MAV in the tunnel an overview of the lateral, longitudinal and vertical position is given in Figure 6.10. The position does not vary much between the runs as the average values lay close together. It is interesting to note that the lateral position shown in Figure 6.10a and the longitudinal position given in Figure 6.10b are not significantly different. The height increases slightly with the runs as shown in Figure 6.10c. The position is not a determining factor for the performance of the MAV in turbulence and therefore longer runs should be considered to compare the performance with and without the pressure probes.

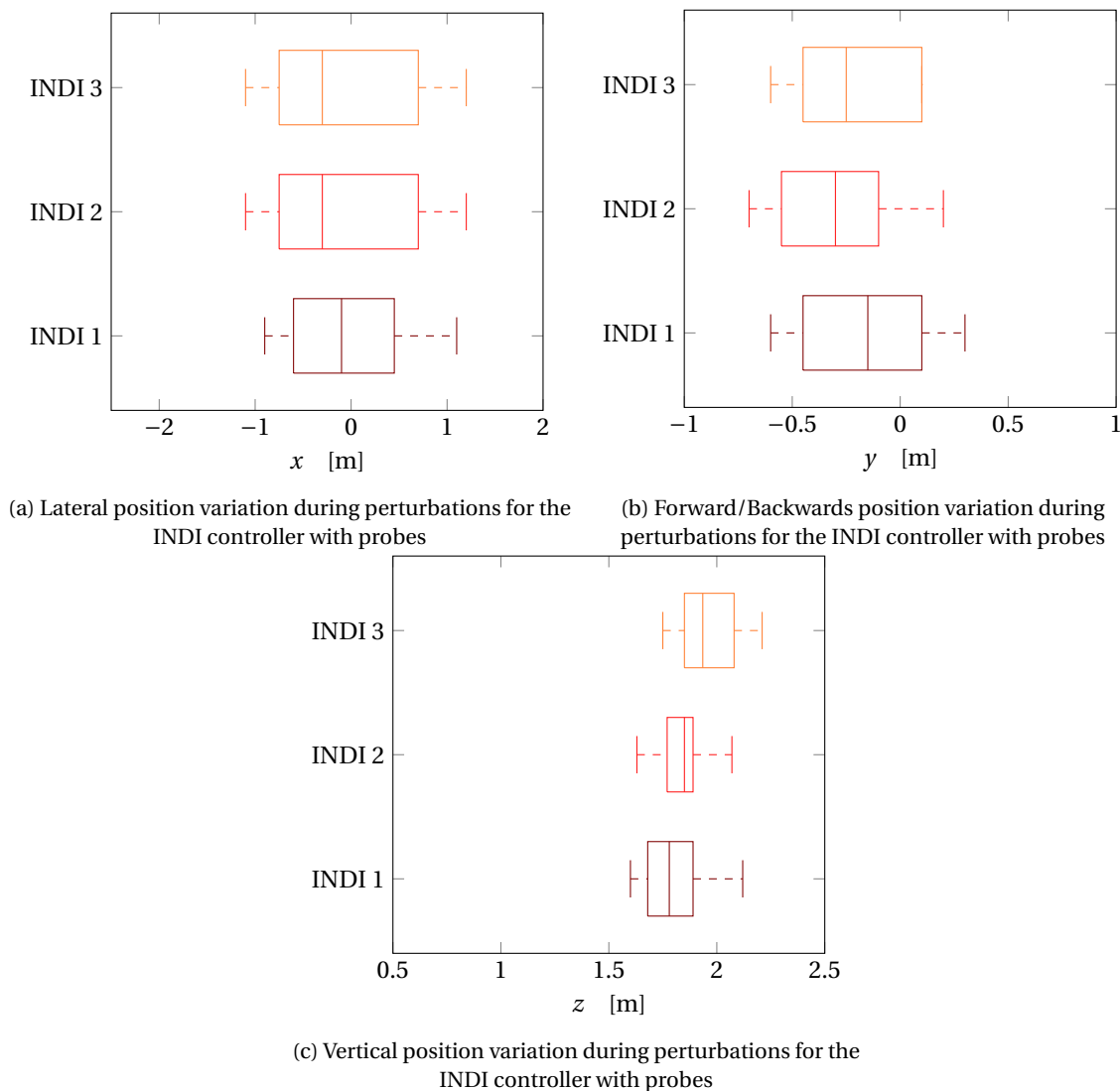
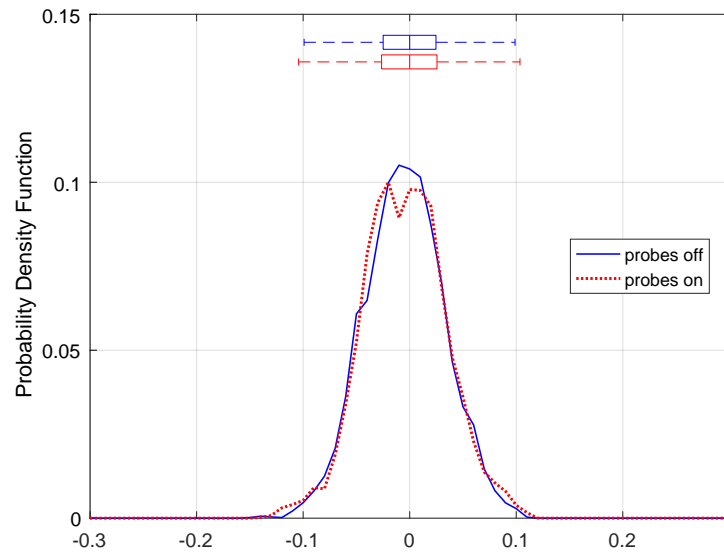
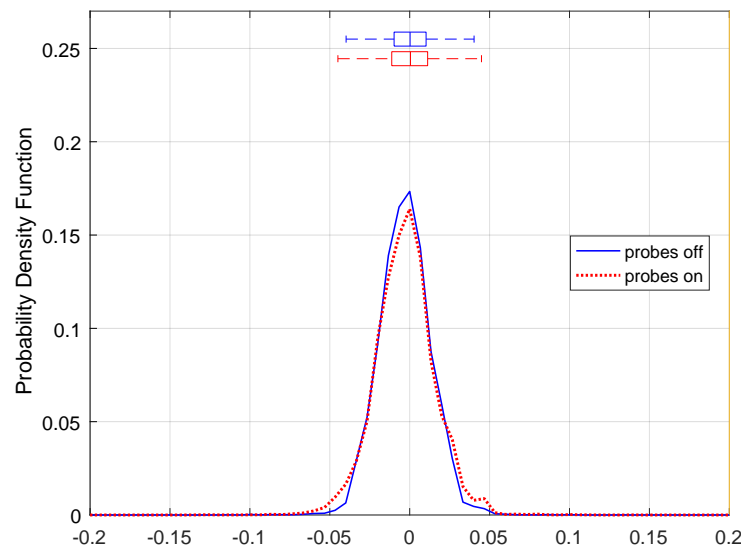


Figure 6.10: Position perturbation comparison for the INDI controller with probes

To increase the time span containing data with and without the probes, the three test cases are combined to look at the differences for the complete test set. On average it can be seen that the probes decrease the performance of the system for both the roll axis shown in Figure 6.11a and the pitch axis given in Figure 6.11b. By analyzing the work performed by Mohamed et al. [4], it is unlikely that the probes decrease the performance of the INDI controller. Mohamed et al. [4] showed that large improvements in the disturbance rejection performance are obtained when the system is combined with a PID controller. The most likely explanation for this unexpected result is that the probes were not working properly during the test. During the pressure probe calibration small cracks were discovered in the probe tubes. These leaks influence the pressure difference measured by the sensors and therefore influence the feed-forward command sent to the ailerons. Due to the leaks, the results presented cannot be used to draw conclusions on the effect of adding the probes to the INDI controller.



(a) Comparison of the roll angle perturbation for the INDI controller with and without probes during the second flight



(b) Comparison for the pitch angle perturbation for the INDI controller with and without probes during the second flight

Figure 6.11: Comparison of the angle perturbations for the INDI controller with and without probes during the second flight

INDI vs PID

It is interesting to compare the INDI controller with the PID controller in terms of disturbance rejection. The reference tracking performance of the system around the roll axis is comparable for the PID and INDI controller, making it possible to perform a fair comparison in terms of disturbance rejection. The reference tracking performance around the pitch axis is much slower for the PID controller, this should be taken into account when looking at the disturbance rejection performance.

For this test it was very difficult to obtain data on the PID controller performance. The PID controller was not precise enough to be flown autonomously in the wind tunnel for a long period of time. The longest time frame in which the MAV flew in the tunnel with the PID controller is 18 seconds. This data will be used to give some preliminary results on the controller performance. The results for the PID controller can be compared to the results for the INDI controller for the same time span of 18 seconds. To make the comparison as fair as possible with the given time frame, the data obtained with the INDI controller will be split into multiple sections of 18 seconds after which the most representative run will be selected for the comparison. In total three runs of 18 seconds could be identified for the INDI controller. The most suitable run will be selected based on the position of the MAV in wind tunnel as this determines the turbulence intensity experienced by

the MAV.

The performance of the INDI controller for the three sections of 18 seconds is given in Figure 6.12. The probability density functions and corresponding box plots for the roll axis are given in Figure 6.12a. The performance of section 2 is clearly worse than the performance of sections 1 and 3. When looking at the position data for section 2, it becomes clear that the MAV was flying at the edge of the wind tunnel at the bottom of the test section as shown in Figure 6.13c. The air speed and turbulence intensity experienced in this region are completely different from the rest of the tunnel as the MAV is flying in the boundary layer of the tunnel floor. The wind tunnel floor corresponds to a height of approximately 0.5 meters as the MAV was initialized on a platform below the inlet. This section of the data will therefore not be chosen as comparison material for the PID controller. For the pitch axis, sections 2 and 3 have a better performance compared to section 1, displayed in Figure 6.12b. The longitudinal and lateral position for these two sections is very similar, as shown in Figure 6.13a and Figure 6.13b. The results for section 1 are obtained for a different position in the wind tunnel giving a different performance.

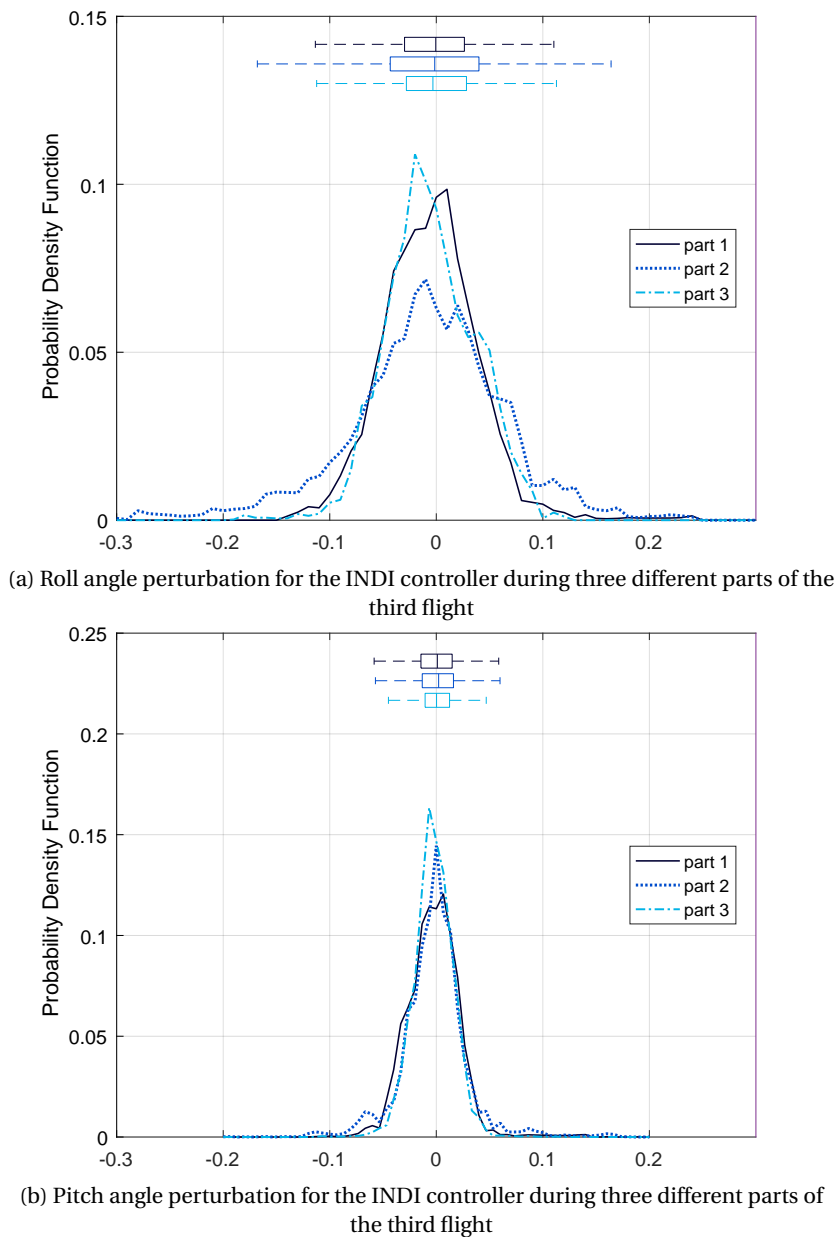


Figure 6.12: Disturbance rejection performance of the roll and pitch angles of the INDI controller for three runs of 18 seconds each

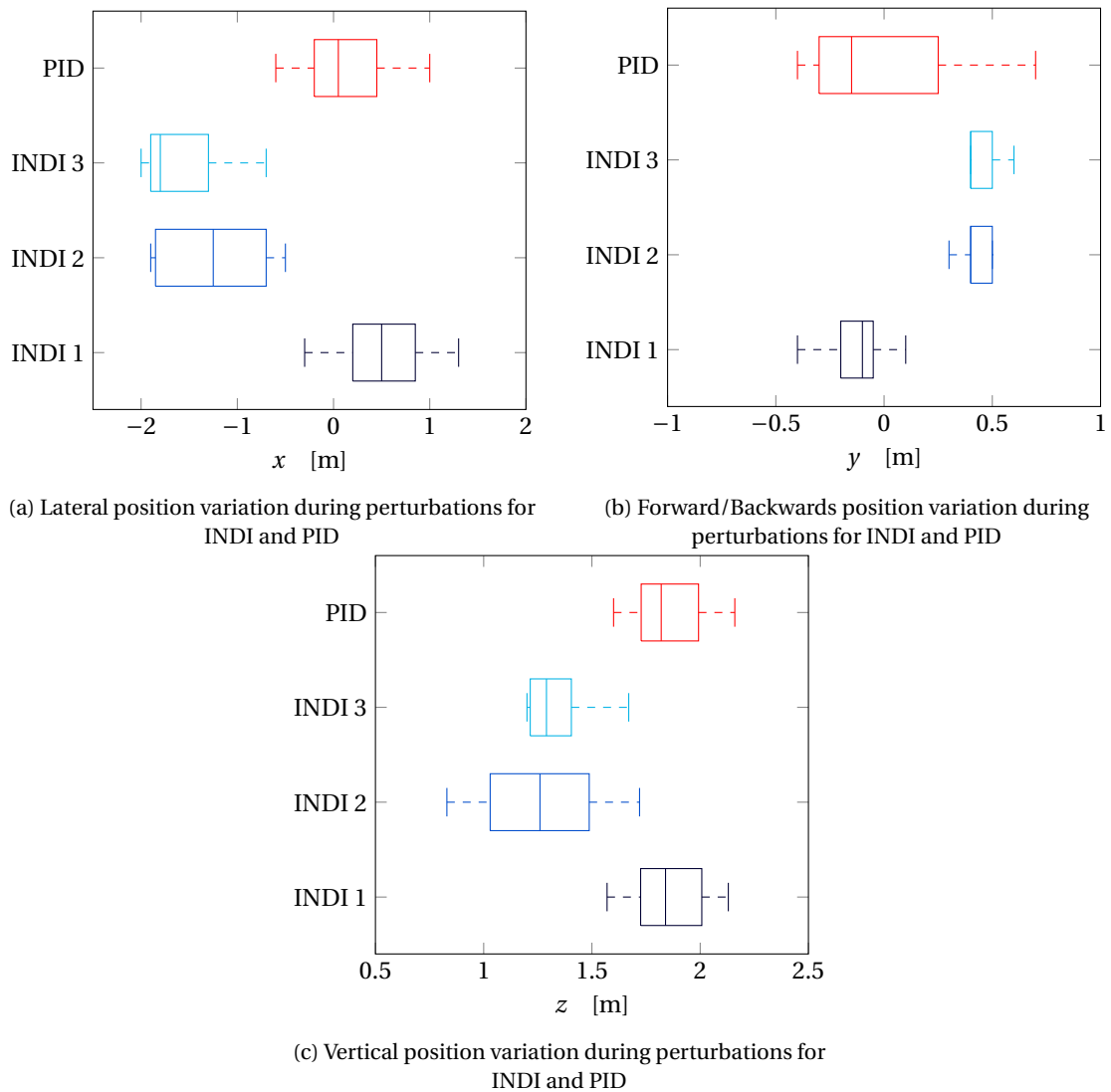


Figure 6.13: Position perturbation comparison between INDI and PID

The INDI controller data which was collected at locations comparable to those experienced by the PID controller is given by the time frame of section 1. This is not surprising as this data was collected immediately before the PID controller data. When comparing section 1 of the INDI controller with the PID controller the probability density plots and box plots given in Figure 6.14 and Figure 6.15 are created. The INDI controller performance is clearly better than the PID controller. The box plot for the roll angle is 40% less for the INDI controller compared to the PID controller. The mean value for the PID controller is not centered around the zero point indicating the integral gain should be increased to obtain a better performance. Despite the performance of the INDI and PID controllers are similar for reference tracking, the disturbance rejection performance is clearly worse. For the pitch angle a similar situation is observed, the probability density function for the PID controller is not symmetrical around the zero value and the peak is much lower compared to INDI. From box plots it can be concluded that the range for the INDI controller is 43% less than the PID controller.

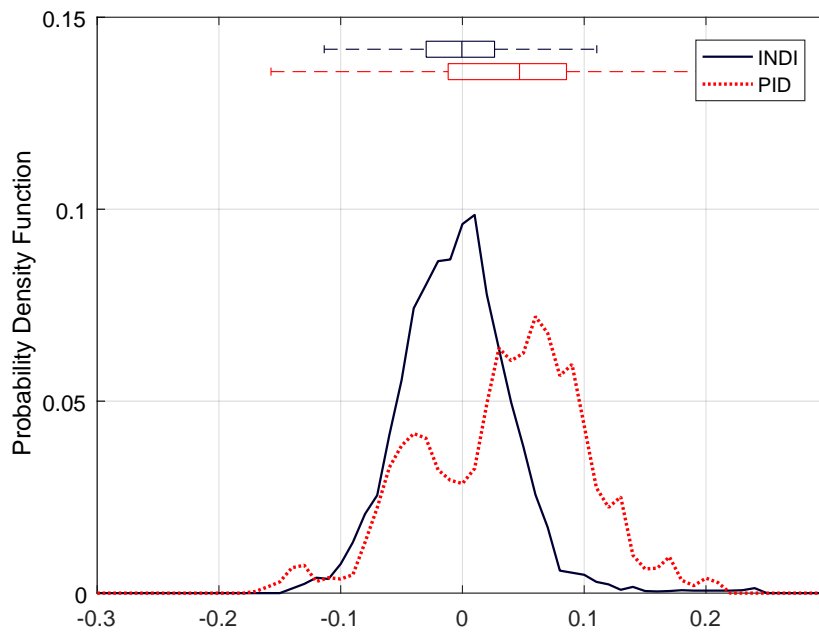


Figure 6.14: Comparison of roll angle perturbation for the PID and INDI controller

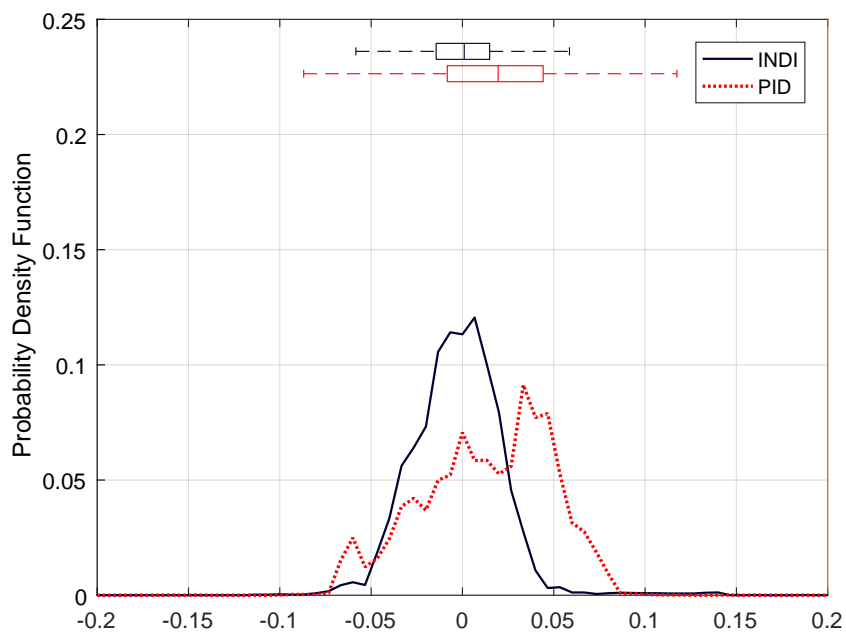


Figure 6.15: Comparison of pitch angle perturbation for the PID and INDI controller

TURBULENCE INTENSITY AND LENGTH SCALE

During the wind tunnel flights only the pitch differential pressure sensors were connected. Additional static tests were performed where the probe was connected to the 4 differential pressures given by Equation 3.16. The aim of this test was to characterize the turbulence intensity and length scale in all three directions. Three measurements were taken at three different positions in the tunnel to characterize the flow for a period of 180 seconds each. The results unfortunately showed that the total-static pressure port was not plugged in the autopilot correctly for logging. No signal is available for this direction. The other pressure differentials were measured but cannot be used for the analysis due to the discovery of small cracks in the probe tubes.

6.3. OUTDOOR TEST FLIGHTS

The final outdoor tests were performed with the modeled values of the control effectiveness and with improved linear gains. Based on the closed-loop reference tracking analysis the INDI gains are lowered and the filter cut-off frequency increased. The PID gains are increased to make the rise time faster especially around the pitch axis. The incremental gains of the PID controller are drastically increased to remove the steady-state errors. An overview of the final controller parameters is given in Table 6.7 for INDI and in Table 6.8 for PID.

Table 6.7: Final parameters of the INDI controllers

	Roll	Pitch
P	185	185
D	22	22
G	0.022	0.008
ω_n	15.9	15.9

Table 6.8: Final parameters of the PID controllers

	Roll	Pitch
P	15000	16000
I	30	30
D	700	1.5

The reference tracking performance of the INDI controller around the roll axis with the final parameters is given in Figure 6.16a. The response is analyzed for a step input of 0.4 radians. The average rise time of the three curves is 0.15 seconds with an overshoot of 10%. This response is faster than the response calculated in section 4.1.1 of Chapter 4. This indicates that the control effectiveness parameters or the actuator model may be subject to errors. Additional flight tests should be performed with different values of the control effectiveness to assess the influence of this parameter on the step response. The reference tracking performance of the PID controller around the roll axis is shown in Figure 6.16b. The rise time of the three curves is on average 0.19 seconds with an overshoot of 5%. The high levels of turbulence experienced during the flight made it

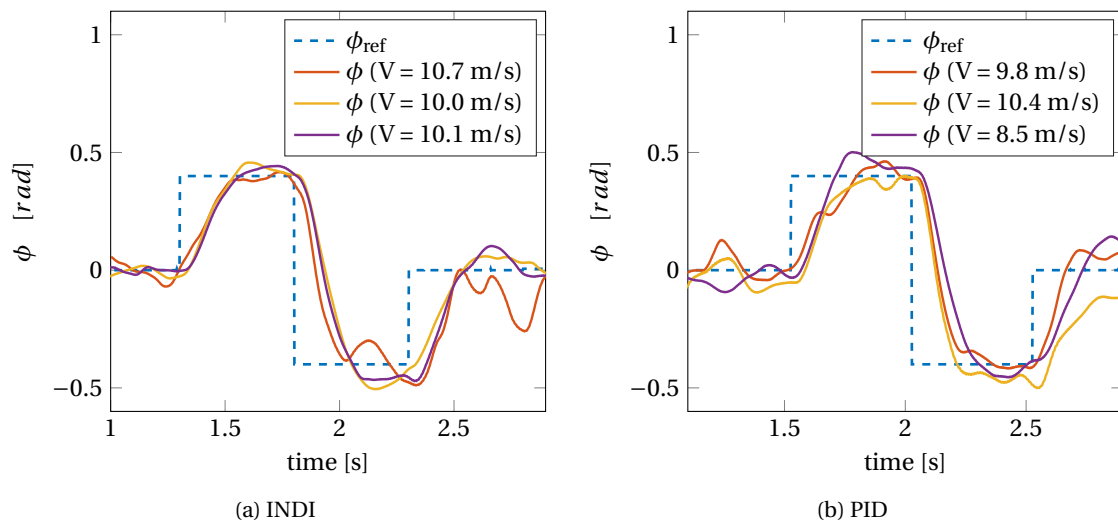


Figure 6.16: Reference tracking performance around the roll axis using final control parameters

difficult to distinguish pilot commands from turbulence effects while watching the MAV in mid air. This is also visible in the data of the pitch response plots. The reference tracking performance of the INDI controller around the pitch axis is given in Figure 6.17a. The variation between the three curves is related to the high levels of turbulence and the difference in flight speeds at which the step responses were executed. The rise time of the test performed at 10.6 m/s is 0.37 sec with an overshoot 13%. Due to a limited amount of batteries, the PID controller step response could only be executed twice during this test day. The effect of high energy

turbulence makes it difficult to assess the performance of the system as shown in Figure 6.17b. The results from a different test day are therefore included. These results were obtained on a calm day with no wind. The performance is clearly visible in Figure 6.18. The response is extremely fast with a rise time of 0.08 seconds. The response is much faster compared to the INDI controller. It should however be noted that the conditions in which this test was executed are different from the conditions experienced by the INDI controller. The incremental gain of the PID controller was increased by a factor 30 compared to the preliminary tests. By analyzing Figure 6.18 it can be seen that a steady-state error is still present in the response. Further flight tests should be performed to assess how much the incremental gain should be increased to fully eliminate the steady-state error. The I gain also influences the overall response therefore attention should be paid to maintain the desired rise time and overshoot.

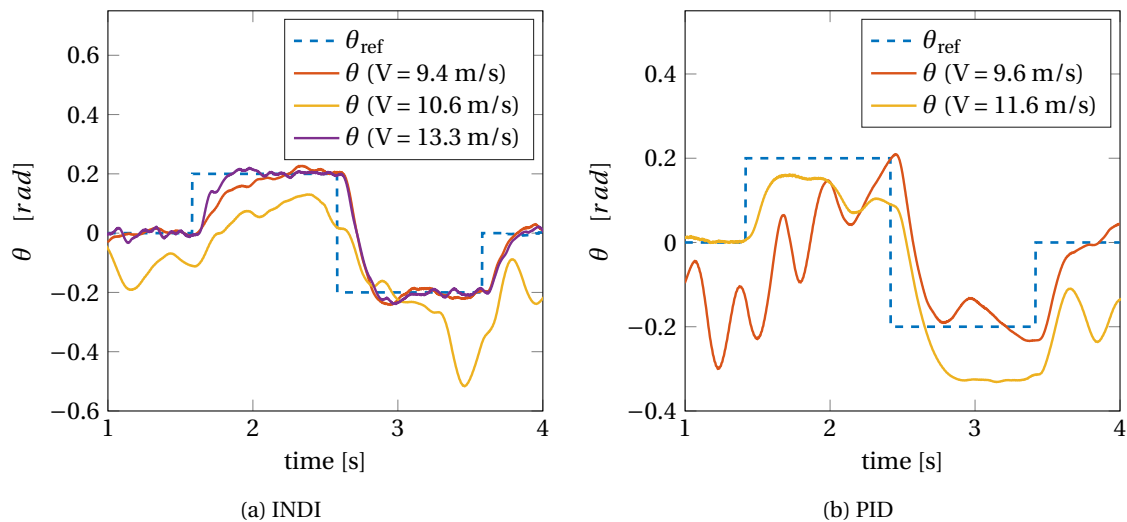


Figure 6.17: Reference tracking performance around the pitch axis using final control parameters

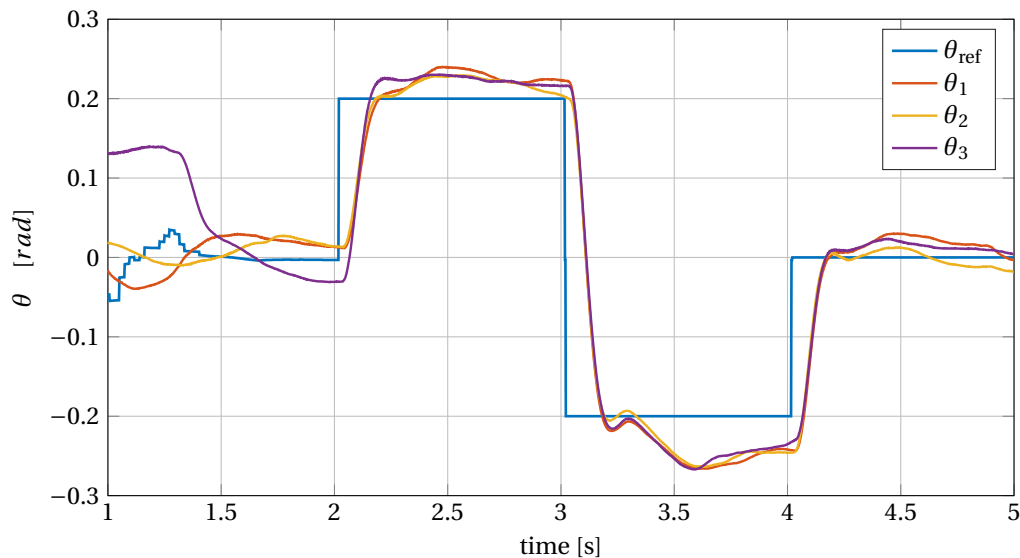


Figure 6.18: Pitch angle during the doublet for the PID controller in calm air at 10m/s

The disturbance rejection tests were performed by flying circuit patterns in the wake of trees. The MAV position was controlled by the pilot therefore the height and pattern of the test flights was not constant. All available data is therefore used for the analysis of the results to provide the best possible comparison between the different controllers. During the data analysis it was discovered that the right probe got obstructed during the second landing. This had an effect on both the airspeed measurement and the pitch probe measurement.

The data of all subsequent flights could therefore not be used to analyze the effect of the probes on the disturbance rejection performance. Subsequent flights included tests with the INDI controller in combination with the pitch probe sensors. No data on this innovative control solution is therefore available for analysis. The data of the first and second flight are combined together with the data from the last test flight in which the pitch probes were not used to control the attitude and the airspeed measurement was based on the left wing probe which was working properly. In total this provides 40 seconds of data for each control approach: INDI, PID and PID with probes. In total the flight data considered is 120 seconds. The von Karman fit is applied to the total data set to determine the longitudinal turbulence length scale. The power spectral density of the longitudinal turbulence spectrum is given in Figure 6.19. The measured turbulence shows attenuation at the high frequency components. According to Mohamed et al. [4] the probes vibrates with the air reducing the power measured at higher frequencies. According to the model presented in Figure 6.19 the longitudinal length scale is 2.5 meters. This is relatively short for outdoor measurements. The data used for the fit is taken for 2 minutes which is a short time span and shows high attenuation of the high frequencies which may lead to errors in the model estimates.

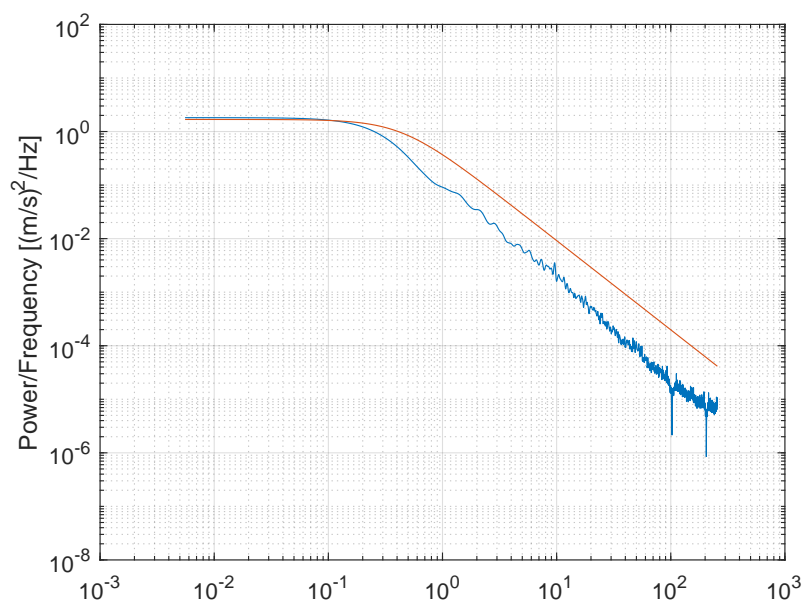


Figure 6.19: Von Karman fit and measured longitudinal turbulence spectrum

During the outdoor flights an airspeed controller was used to maintain the airspeed around the cruise condition of 10m/s. The average speed of the data set is 9.7m/s with a turbulence intensity level T_i of 12.9%. The disturbance rejection performance of the three controllers is presented in terms of the probability density function of the attitude error. Around the roll axis the performance is shown in Figure 6.20. The INDI controller decreases the boxplot range by 21% thereby increasing the peak of the probability density function around the zero point. The enhanced PID controller with the pitch probes does not show an improvement compared to the baseline PID controller. From the flight tests performed by Mohamed et al. a higher probability density function is expected [4]. By analyzing the flight test data an offset in the filtered probe signal was identified. This offset should have been eliminated by the high pass filter. The high pass filter showed the same behavior during subsequent tests when a constant offset was programmed into the probe value. By increasing the accuracy of the high pass filter parameters to a precision of 10^{-6} instead of 10^{-4} the offset was removed. The high pass filter error influences the control signal to the ailerons decreasing the performance of the pitch probe system. Another cause of concern is the overheating of the servos. The same servos were used for all outdoor test flights leading to wear of the gears. To eliminate this source of error, the servos must be replaced after each test flight.

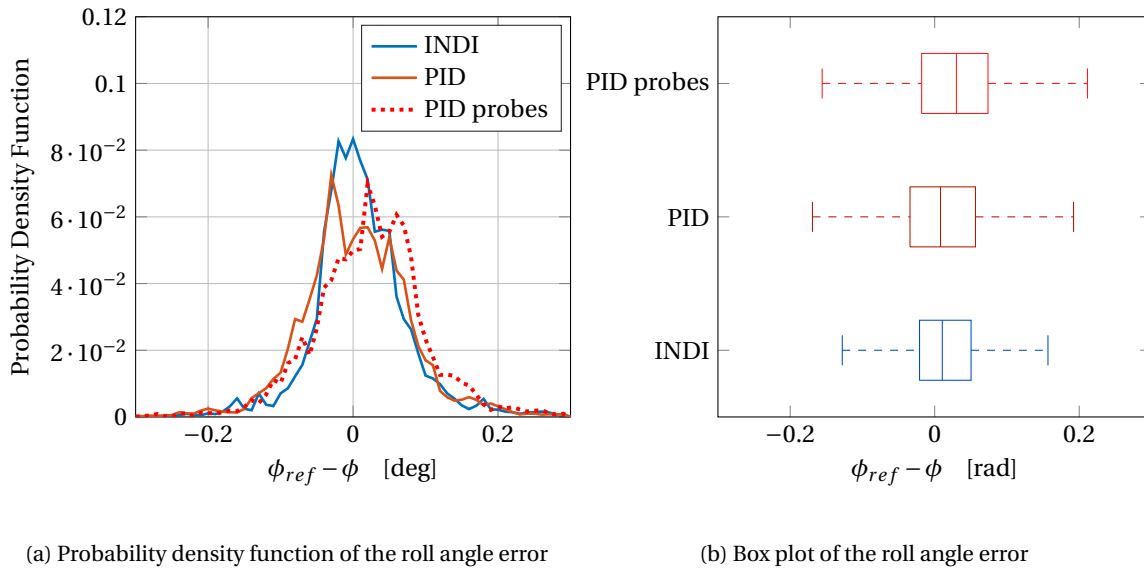


Figure 6.20: Disturbance rejection performance around the roll axis

Around the pitch axis the INDI controller shows a clear improvement in the probability density function shown in Figure 6.21. The box plot range is decreased by 24% compared to the baseline PID controller. The enhanced PID controller does not show the expected improvement in performance. To assess the performance of the enhanced PID controller additional flight tests should be performed with an improved high pass filter and new servos.

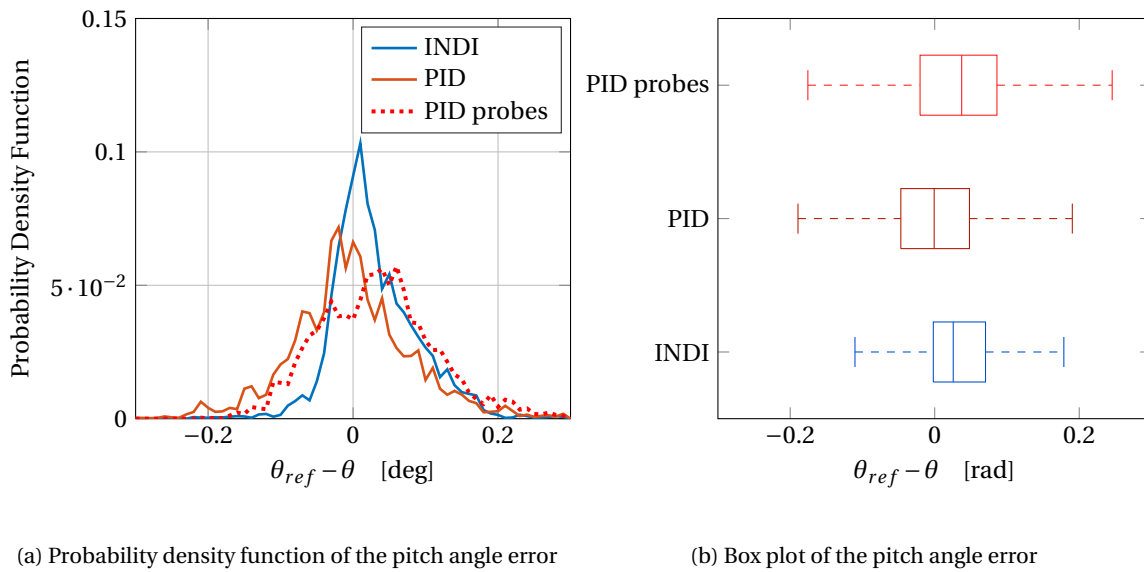


Figure 6.21: Disturbance rejection performance around the pitch axis

7

CONCLUSION

This Master Thesis project investigated the disturbance rejection performance of the INDI controller with and without phase-advanced sensors and compared its performance to a traditional PID controller with and without phase-advanced sensors. A number of preliminary and intermediary steps are required to address the research question.

The first challenge is to develop a model of the MAV and to investigate the calibration of the phase-advanced sensors. The MAV model is used by the INDI controller to predict the response of the system to roll and pitch inputs. The calibration of the pressure probes is used to measure the incoming flow angle and velocity. This part of the project has led to a number of findings:

- The control effectiveness is a nonlinear function of airspeed. Three different approaches can be used to calculate the effectiveness: roll and pitch rig tests, wind tunnel flights and airspeed controlled outdoor flights. Both open loop and closed loop tests can be used to generate data for the model. For the pitch axis the angle of attack could not be measured during free flight, making the pitch rig results the most reliable data to model the control effectiveness.
- The yaw coupling during the aperiodic roll maneuver can be neglected. The yaw components do not influence the value of the control effectiveness of the ailerons G_{δ_a} .
- Around the roll axis the damping term F_p is one order of magnitude smaller compared to the aileron effectiveness G_{δ_a} indicating that the principle of time scale separation can be applied. Around the pitch axis the damping term related to the angle of attack and the elevator effectiveness have the same order of magnitude. Incorporating the damping term in the INDI control structure is complex. For the purpose of this research the damping term was neglected taking into account that errors in the angular acceleration prediction can occur.
- The servo is a rate limited first order system with an initial delay of 10 milliseconds.
- The 5-hole pressure probe can be calibrated by using 4 differential pressure measurements. The calibration formulas used for spherical probes were modified to improve the model fit. The calibration parameters show large variations between each run. Variations have been identified as sensor fluctuations which are within the specifications of the manufacturer. The model fit can be improved by using a more accurate reference signal which captures fast variations in the wind tunnel speed.

The second challenge is to create an experimental set-up suitable for testing the system in high turbulence intensities. The most challenging and also innovative part of this set-up is the autonomous wind tunnel flight. The position control loops are designed such that the MAV can hover in a 2x2x2 meter box instead of moving with a constant speed along a trajectory. To achieve a fully autonomous wind tunnel flight in turbulence the following aspects have to be considered:

- Position data have to be sent to the MAV in the wind tunnel. A datalink connection is established by connecting the MAV to the Optitrack system by using a wireless WiFi module with a maximum datalink frequency of 20Hz.

- The course angle cannot be used for the lateral control due to the low ground speed. The heading angle is therefore used to control the lateral displacements.
- The throttle is used to control the MAV longitudinal and vertical position leading to a coupling between the two control loops. A damping term is added to the throttle controller and an integral gain is added to the pitch setpoint controller. This ensures small changes and offsets are counteracted.

The third challenge is to design an INDI and PID attitude controller for the MAV to be able to fly in high turbulence intensities. The most important aspects that have to be taken into account when designing these controllers are the following:

- The INDI controller is robust to errors in the control effectiveness matrix. Initial outdoor flights and autonomous wind tunnel flights were performed with estimates of the control effectiveness. During these tests the controller was stable and able to counteract disturbances.
- To improve the disturbance rejection performance, the cut-off frequency of the second order low pass filter should be designed to give the minimum delay.
- The closed loop analysis of the INDI controller shows that the system is rate limited. The performance therefore depends on both the actuator dynamics and the control effectiveness. When the system is operated in the rate limited region, increasing the gains does not necessarily lead to an improved performance.
- During autonomous outdoor flights, energy control loops should be used in combination with INDI. The aggressive response of the INDI controller led to fast pitch angle changes at low speeds causing multiple stall cases.
- The PID and INDI controller can be compared in terms of disturbance rejection if the controllers have the same reference tracking performance.
- The PID controller can be tuned to achieve the same reference tracking performance as INDI. Each flight condition requires different linear gains as this is a linear control technique. Without a complete aerodynamic model of the MAV it is difficult to assess when the maximum performance is reached for each flight condition. Due to the rate limiter the PID and INDI gains cannot be directly compared. Additional tests flight should be performed to investigate the effect of the rate limiter on the PD gains and the effect of the damping terms on the ratio between the proportional and derivative gain.

During the wind tunnel tests technical difficulties with a broken datalink connection allowed for 3 days of testing instead of 5. The short time span in which all systems had to be tuned led to a very challenging situation. Autonomous flight with INDI in turbulence was given the highest priority. The results obtained during the wind tunnel set-up lead to the following conclusions:

- The most important design considerations when tuning a controller for autonomous wind tunnel flights are a fast rise time and the total elimination of all steady-state errors.
- The PID attitude controller cannot be used to fly in the wind tunnel with the gains selected during outdoor flights. The integral gain has to be increased as much as possible to ensure all steady-state errors are eliminated. The gains required to fly in a 2x2x2 meter box have to be extremely aggressive to counteract even the slightest disturbances.
- The INDI attitude controller is an excellent technique to perform autonomous wind tunnel flights. It is capable of maintaining the MAV within a 1x1x1 meter box with an estimated value of the control effectiveness and an accurate model of the actuator dynamics. The box plot range of the INDI controller in roll is 40% smaller and in pitch it is 43% smaller compared to the PID controller. The controllers are compared for the same time interval of 18 seconds with the same average position in the wind tunnel.
- The position of the MAV in the wind tunnel determines the disturbance rejection performance. This implies that the turbulence intensity varies depending on the location in the tunnel.
- No conclusions can be drawn on the performance of the pressure probes in combination with the INDI controller due to leaks in the tubes connecting the sensor to the probe head. These leaks were discovered after the autonomous wind tunnel flights during the sensor calibration.

Outdoor flight tests were performed with improved linear PD gains and modeled values of the control effectiveness. The tests were performed in a field surrounded by trees during a windy day in turbulence intensities of 12.9%. An airspeed controller was used to keep the cruise speed around 10m/s. From the test flights the following conclusions can be drawn:

- Given a comparable reference tracking performance around the roll axis, the INDI controller improves the disturbance rejection performance compared to PID. The range of the box plot for the roll angle error decreased by 21% when using INDI.
- Around the pitch axis, the step responses are influenced by high energy turbulence making it difficult to assess the rise time and overshoot properties. The PID controller was tuned to be very aggressive to match the INDI controller behavior. More test flights should be performed as steady-state errors were still visible in the PID response. The INDI controller improved the disturbance rejection performance by 24% compared to PID.
- The high pass filter used for the probes introduced offsets in the signal. The pressure probes did not improve the performance of the system indicating more precise filter parameters should be used.
- No reliable data could be obtained on the INDI controller with pressure probes. Only a limited amount of test flights could be executed and the flight data show that one of the probes got obstructed during the second landing making all subsequent results unreliable.

Recommendations for further testing and research:

- The turbulence intensity profile of the OJF with turbulence generating grids should be determined before the test flights.
- Ideally based on the turbulence intensity profile, the MAV needs to fly in a 1x1x1 meter box in which the turbulence intensity is fairly constant.
- Tests should be performed which use the same linear PD gains for the PID and INDI controller. This comparison provides additional information on the effects of the rate limiter and the damping terms.
- Additional flight tests should be performed with improved high pass filter parameters to assess the performance of the INDI controller in combination with the pitch probes. The servo degradation should be evaluated after each flight test.

BIBLIOGRAPHY

- [1] B. Adler, J. Xiao, and J. Zhang, *Autonomous exploration of urban environments using unmanned aerial vehicles*, *Journal of Field Robotics* **31**, 912 (2014).
- [2] M. A. Goodrich, B. S. Morse, D. Gerhardt, and J. L. Cooper, *Supporting wilderness search and rescue using a camera-equipped mini uav*, *Journal of Field Robotics* **25**, 89 (2008).
- [3] S. Watkins, J. Millbank, B. Loxton, and W. Melbourne, *Atmospheric winds and their implications for microair vehicles*, *AIAA* **44**, 2591 (2006).
- [4] A. Mohamed, M. Abdulrahim, S. Watkins, and C. R., *Development and flight testing of a turbulence mitigation system for micro air vehicles*, *Journal of Field Robotics* (2015), 10.1002/rob.21626.
- [5] E. J. J. Smeur, Q. Chu, and G. C. H. E. de Croon, *Adaptive incremental nonlinear dynamic inversion for attitude control of micro aerial vehicles*, *AIAA Journal of Guidance, Control, and Dynamics* **39**, 450 (2016).
- [6] E. J. J. Smeur, G. C. H. E. de Croon, and Q. Chu, *Gust disturbance alleviation with incremental nonlinear dynamic inversion*, Submitted to IROS Conference (2016).
- [7] J. J. E. Slotine and W. Li, *Applied Nonlinear Control* (1991) Chap. 6, pp. 207–276.
- [8] J. Han, *From pid to active disturbance rejection control*, *IEEE transactions on Industrial Electronics*, **56**, 900 (2009).
- [9] K. H. Ang, G. Chong, and Y. Li, *Pid control system analysis, design, and technology*, *IEEE Transactions on Control Systems Technology* **13**, 559 (2005).
- [10] A. Visioli, *Practical PID Control* (2006).
- [11] J. G. Ziegler and N. B. Nichols, *Optimum settings for automatic controllers*, *Transactions of ASME* **64**, 759 (1942).
- [12] Paparazzi-UAV, *Control loops*, Available at http://wiki.paparazziuav.org/wiki/Control_Loops (2016).
- [13] Pixhawk, *Fixedwing aircraft controller tuning guide*, Available at https://pixhawk.org/users/fixedwing_pid_tuning (2016).
- [14] T. Hägglund, *A unified discussion on signal filtering in pid control*, *Control Engineering Practice* **21**, 994 (2013).
- [15] MathWorks, *Tune pid controller to favor reference tracking or disturbance rejection*, Available at <http://nl.mathworks.com/help/slcontrol/ug/tune-pid-controller-to-balance-tracking-and-disturbance-rejection-performance.html> (2016).
- [16] Q. Chu, *Ae4311-1: Advanced flight control*, Available on Blackboard (2015).
- [17] H. P. Lee, S. E. Reiman, C. H. Dillon, and H. Youssef, *Robust nonlinear dynamic inversion control for a hypersonic cruise vehicle*, *AIAA Guidance, Navigation, and Control Conference and Exhibit AIAA Paper 2007-6685*, 3380 (20 - 23 August 2007).
- [18] J. S. Brinker and K. A. Wise, *Flight testing of reconfigurable control law on the x-36 tailless aircraft*, *AIAA Journal of Guidance, Control, and Dynamics* **24**, 903 (2001).
- [19] K. Bordignon and J. Bessolo, *Control allocation for the x-35b*, *2002 Biennial International Powered Lift Conference and Exhibit*, *AIAA Paper 2007-6020* (2002), 10.2514/6.2002-6020.

- [20] P. R. Smith, *A simplified approach to nonlinear dynamic inversion based flight control*, 23rd Atmospheric Flight Mechanics Conference, Boston, MA, U.S.A **AIAA Paper 1998-4461** (1998), 10.2514/6.1998-4461.
- [21] S. Sieberling, Q. Chu, and A. J. Mulder, *Robust flight control using incremental nonlinear dynamic inversion and angular acceleration prediction*, **AIAA 33**, 1732 (2010).
- [22] B. J. Bacon and A. J. Ostroff, *Reconfigurable flight control using nonlinear dynamic inversion with a special accelerometer implementation*, **AIAA Guidance, Navigation, and Control Conference and Exhibit**, Denver, CO, U.S.A. **AIAA Paper 2000-4565** (2000), 10.2514/6.2000-4565.
- [23] B. J. Bacon, A. J. Ostroff, and S. M. Joshi, *Reconfigurable ndi controller using inertial sensor failure detection & isolation*, **IEEE Transactions on Aerospace and Electronic Systems 37** (October 2001).
- [24] M. C. Vlaar, *Incremental Nonlinear Dynamic Inversion flight control implementation and flight test on a fixed wing UAV*, Master's thesis, Delft University of Technology (2014).
- [25] S. Ravi, *The influence of turbulence on a flat plate aerofoil at Reynolds numbers relevant to MAVs*, Ph.D. thesis, RMIT (2011).
- [26] T. F. Instrumentation, *Cobra probe references*, Available at <http://www.turbulentflow.com.au/Products/CobraProbe/CobraReferences.php> (2016).
- [27] A. R. Rodi and D. C. Leon, *Correction of static pressure on a research aircraft in accelerated flight using differential pressure measurements*, **Atmospheric Measurement Techniques 5**, 2569–2579 (2012).
- [28] A. Carruthers, A. Thomas, and G. Taylor, *Automatic aeroelastic devices in the wings of a steppe eagle aquila nipalensis*, **Journal of Experimental Biology 210**, 4136 (2007).
- [29] A. Mohamed, S. Watkins, R. Clothier, and M. Abdulrahim, *Influence of turbulence on mav roll perturbations*, **International Journal of Micro Air Vehicles 6**, 175 (2014).
- [30] A. Mohamed, K. Massey, S. Watkins, and R. Clothier, *The attitude control of fixed-wing mavs in turbulent environments*, **Progress in Aerospace Sciences 66**, 37 (2014).
- [31] J. A. Mulder, W. H. J. J. van Staveren, J. C. van der Vaart, E. de Weerd, C. C. de Visser, A. C. in 't Veld, and E. Mooij, *AE3202 Flight Dynamics* (2013).
- [32] L. Sonneveldt, *Adaptive Backstepping Flight Control for Modern Fighter Aircraft*, Ph.D. thesis, Delft University of Technology, Delft, The Netherlands (2010).